



**RAY NEXT-EVENT ESTIMATOR TRANSPORT OF PRIMARY AND  
SECONDARY GAMMA RAYS**

THESIS

Whitman T. Dailey, Captain, USAF  
AFIT/GNE/ENP/11-M04

**DEPARTMENT OF THE AIR FORCE**

**AIR UNIVERSITY**

***AIR FORCE INSTITUTE OF TECHNOLOGY***

**Wright-Patterson Air Force Base, Ohio**

APPROVED FOR PUBLIC RELEASE; DISTRIBUTION UNLIMITED

The views expressed in this thesis are those of the author and do not reflect the official policy or position of the United States Air Force, the Department of Defense, or the United States Government. This material is declared a work of the U.S. Government and is not subject to copyright protection in the United States.

AFIT/GNE/ENP/11-M04

RAY NEXT-EVENT ESTIMATOR TRANSPORT OF PRIMARY AND  
SECONDARY GAMMA RAYS

THESIS

Presented to the Faculty

Department of Engineering Physics

Graduate School of Engineering and Management

Air Force Institute of Technology

Air University

Air Education and Training Command

In Partial Fulfillment of the Requirements for the

Degree of Master of Science in Nuclear Engineering

Whitman T. Dailey, BS  
Captain, USAF

March 2011

APPROVED FOR PUBLIC RELEASE; DISTRIBUTION UNLIMITED

AFIT/GNE/ENP/11-M04

RAY NEXT-EVENT ESTIMATOR TRANSPORT OF PRIMARY AND  
SECONDARY GAMMA RAYS

Whitman T. Dailey, BS  
Captain, USAF

Approved:

---

Kirk A. Mathews, PhD (Chairman)

---

Date

---

Maj Benjamin P. Kowash (Member)

---

Date

---

David Gerts, PhD (Member)

---

Date

---

Lt Col Matthew S. Zickafoose (Member)

---

Date

**Abstract**

The purpose of this thesis was to investigate the application of the ray next-event estimation Monte Carlo method to the transport of primary and secondary gamma rays. The problem of interest was estimation of the free field flux at a distant point in a vacuum from a point source in the atmosphere. An existing Fortran code for neutron transport, Ray Next-Event Estimator v4.0, was adapted to perform photon transport computations including coherent scattering, incoherent scattering, photoelectric absorption, and pair production interactions. Production and transport of secondary gamma rays produced in bremsstrahlung, neutron inelastic scatter, and neutron absorption interactions was also implemented.

A new version of the code, Ray Next-Event Estimator v5.1, was produced with the added photon transport capability and other changes focused on future development of the estimator code for application to this class of problems. Code version 5.1 was exercised and compared to version 4.0 for neutron transport computations. Code version 5.1 was also demonstrated for application to gamma ray transport computations and coupled neutron-photon transport computations.

AFIT/GNE/ENP/11-M04

*For her.*

## **Acknowledgements**

I would like to thank my research advisor, Dr. Kirk Mathews, for his guidance, insight, and patience throughout the course of this research. Without his help, I would have been much more lost than usual, and certainly would not have made it to a successful conclusion. Thanks also go to Lt Col Matthew Zickafoose for his patience, assistance, and trust as he handed over his work just so that some cheeky graduate student could make a mess out of it. Thank you also to the members of my thesis committee and to the students and faculty of AFIT/ENP for the guidance, discussions, and classes that aided the successful completion of this research.

# Table of Contents

	Page
Abstract .....	iv
Acknowledgements .....	vi
List of Figures .....	ix
List of Tables .....	xiii
List of Symbols .....	xv
I. Introduction.....	1
The Air to Space Particle Transport Problem.....	1
The Ray Next-Event Estimator.....	4
Statement of the Research Problem .....	5
Assumptions and Limitations .....	6
Ray Next-Event Estimation.....	6
Neutron Transport Calculations .....	6
Atmospheric Representation .....	6
Geometric Representation.....	7
Photon Interactions .....	7
Secondary Gamma Ray Production Interactions .....	9
Motion of Nuclei and Charged Particles .....	10
Decay of Excited Nuclei by Gamma Emission .....	10
Approach.....	11
II. Theory .....	12
Coherent Scattering.....	13
Photoelectric Absorption .....	17
Incoherent Scattering.....	19
Pair Production .....	24
Bremsstrahlung Radiation .....	25
Decay of Excited Nuclei by Gamma Emission.....	27
III. Methodology .....	29



	Page
RNEE Transport of Speed-of-Light Neutral Particles .....	29
Implementation of Gamma Ray Interaction Physics .....	29
Scattering Angle Selection .....	30
Angular Density .....	44
Post-Scatter Energy .....	47
Secondary Particles .....	48
Bremsstrahlung Photons .....	48
Decay of Excited Nuclei by Gamma Emission .....	49
Gamma Ray Source Energy Selection.....	53
Summary of Major Changes to RNEE 4.0.....	57
Source Code Reorganization .....	57
Variable Dimensional Extension .....	58
Photon Interaction Physics Data .....	59
Particle Stacking in Linked Lists .....	61
Batch and Particle Sequencing .....	63
IV. Estimator Results and Demonstration.....	65
RNEE v5.1 Function Check .....	66
Run #1 - Neutron Transport, Monoenergetic Source .....	67
Run #2 - Neutron Transport, Fission Source .....	70
RNEE v5.1 Demonstration: Gamma Ray Transport .....	73
Run #3 - Gamma Ray Transport, Monoenergetic Source .....	73
Run #4 - Gamma Ray Transport, Fission Source .....	78
RNEE v5.1 Demonstration: Coupled Neutron-Photon Transport .....	81
Run #5 - Coupled Transport, Fission Neutron Source .....	81
Run #6 - Coupled Transport, Monoenergetic Neutron Source .....	83
V. Conclusions.....	88
Appendix A. RNEE 5.1 Release Notes.....	90
Appendix B. Sample Input Files .....	97
Bibliography.....	109

## List of Figures

Figure	Page
1. The Transport Problem.....	2
2. Photon Interaction Cross Sections for a N-O-Ar Mixture Like Air (NIST, 2010). ....	12
3. Coherent Scattering.....	13
4. Scaled Angular Distribution of Coherently Scattered Photons Incident from Left.....	15
5. Distribution of the Cosine of the Scattering Angle for Coherently Scattered Photons. ....	17
6. Photoelectric Absorption. ....	18
7. Incoherent Scattering.....	19
8. Scaled Angular Distribution of Incoherently Scattered Photons of Various Energies Incident from Left.....	21
9. Distribution of the Cosine of the Scattering Angle for Incoherently Scattered Photons of Various Energies. ....	23
10. Pair Production. ....	24
11. Level Scheme and Decay Gammas for $^{14}\text{N}$ , energy levels in keV. (NNDC, 2010).....	28
12. PDF and CDF for the Distribution of the Cosine of the Polar Scattering Angle for Coherently Scattered Photons.....	32
13. Distribution of 100,000 Angle Cosines Drawn by the Estimator Code Compared to the Angle Cosine CDF for Coherent Scattering. ....	33
14. Sampling by Rejection from the Klein-Nishina Distribution.....	36

Figure	Page
15. Sampling Efficiency for Basic Sampling by Rejection from the Klein-Nishina Distribution.....	37
16. Sampling by Rejection from Bounded Sample Space from the Klein-Nishina Distribution.....	39
17. Sampling Efficiency for Improved Sampling by Rejection from the Klein-Nishina Distribution.....	40
18. Distribution of 100,000 Angle Cosines Drawn by Estimator Code for Various Values of Alpha Compared to the Angle Cosine CDFs for Incoherent Scattering.....	42
19. Formatted List of Levels 1-6 for $^{15}\text{N}$ . ....	50
20. PDF and CDF for the Distribution of Gamma Ray Energies from Fission of $^{235}\text{U}$ . ....	55
21. Cumulative Distribution of 100,000 Gamma Ray Energies Drawn by the Estimator Code for Fission of $^{235}\text{U}$ Compared to the Gamma Energy CDF.....	57
22. Sample of Output from XCOM Photon Cross Sections Database.....	60
23. Ray-Estimated Neutron Flux Per Source Neutron at the Flux-Point from a Monoenergetic Point Source in Time and Energy Computed by RNEE v4.0.....	68
24. Ray-Estimated Neutron Flux Per Source Neutron at the Flux-Point from a Monoenergetic Point Source in Time and Energy Computed by RNEE v5.1.....	68
25. Ray- and Point- Estimated Time Integrated Flux Spectra for Neutron Transport from a Monoenergetic Point Source, 0 to 2 MeV.....	69
26. Watt Distribution of Neutron Energies from Fission of $^{235}\text{U}$ . ....	71

Figure	Page
27. Ray-Estimated Neutron Flux Per Source Neutron at the Flux-Point from a $^{235}\text{U}$ Watt Distributed Point Source in Time and Energy Computed by RNEE v4.0.....	72
28. Ray-Estimated Neutron Flux Per Source Neutron at the Flux-Point from a $^{235}\text{U}$ Watt Distributed Point Source in Time and Energy Computed by RNEE v5.1.....	72
29. Point-Estimated Gamma Ray Flux Per Source Gamma Ray at the Flux-Point from a Monoenergetic Point Source in Time and Energy. ....	75
30. Ray-Estimated Gamma Ray Flux Per Source Gamma Ray at the Flux-Point from a Monoenergetic Point Source in Time and Energy. ....	75
31. Inverse Relative Standard Deviation of Point- and Ray- Estimated Gamma Ray Flux at the Flux-Point from a Monoenergetic Point Source in Time and Energy.....	76
32. Ray- and Point- Estimated Time Integrated Flux Spectra for Gamma Ray Transport from a Monoenergetic Point Source. ....	77
33. Point-Estimated Gamma Ray Flux Per Source Gamma Ray at the Flux-Point from a $^{235}\text{U}$ Fission Point Source in Time and Energy. ....	79
34. Ray-Estimated Gamma Ray Flux Per Source Gamma Ray at the Flux-Point from a $^{235}\text{U}$ Fission Point Source in Time and Energy. ....	79
35. Inverse Relative Standard Deviation of Point- and Ray- Estimated Gamma Ray Flux at the Flux-Point from a $^{235}\text{U}$ Fission Point Source in Time and Energy. ....	80
36. Point-Estimated Secondary Gamma Ray Flux Per Source Neutron at the Flux-Point from a $^{235}\text{U}$ Fission Neutron Point Source in Time and Energy. ....	82

Figure	Page
37. Ray-Estimated Secondary Gamma Ray Flux Per Source Neutron at the Flux-Point from a $^{235}\text{U}$ Fission Neutron Point Source in Time and Energy. ....	82
38. Inverse Relative Standard Deviation of Point- and Ray- Estimated Secondary Gamma Ray Flux at the Flux-Point from a $^{235}\text{U}$ Fission Neutron Point Source in Time and Energy.....	83
39. Point-Estimated Secondary Gamma Ray Flux Per Source Neutron at the Flux-Point from a Monoenergetic Neutron Point Source in Time and Energy. ....	85
40. Ray-Estimated Secondary Gamma Ray Flux Per Source Neutron at the Flux-Point from a Monoenergetic Neutron Point Source in Time and Energy. ....	85
41. Inverse Relative Standard Deviation of Point- and Ray- Estimated Secondary Gamma Ray Flux at the Flux-Point from a Monoenergetic Neutron Point Source in Time and Energy.....	86

## List of Tables

Table	Page
1. Results of Chi-Squared Test for Fit of 100,000 Angle Cosines Drawn by the Code for Coherent Scattering.....	34
2. Comparison of Theoretical and Observed Rejection Sampling Efficiencies for 100,000 Angle Cosines Drawn by the Estimator Code for Various Values of Alpha for Incoherent Scattering. ....	41
3. Results of Chi-Squared Test for Fit of 100,000 Incoherent Scatter Angle Cosines Drawn by the Code for Various Values of Alpha. ....	43
4. Results of Chi-Squared Test for Fit of 100,000 Gamma Ray Energies Drawn by the Estimator Code for Fission of $^{235}\text{U}$ .....	57
5. List of Simulations Used to Exercise the Estimator Code.....	66
6. Properties of the Source and Flux-Point Time-Energy Grid for Monoenergetic Neutron Source Neutron Transport Demonstration. ....	67
7. Properties of the Source and Flux-Point Time-Energy Grid for Fission Neutron Source Neutron Transport Demonstration.....	70
8. Properties of the Source and Flux-Point Time-Energy Grid for Monoenergetic Gamma Ray Source Gamma Ray Transport Demonstration. ....	74
9. Properties of the Source and Flux-Point Time-Energy Grid for $^{235}\text{U}$ Fission Gamma Ray Source Gamma Ray Transport Demonstration. ....	78
10. Properties of the Source and Flux-Point Time-Energy Grid for Fission Neutron Source Coupled Neutron-Photon Transport Demonstration. ....	81

Table	Page
11. Properties of the Source and Flux-Point Time-Energy Grid for Monenergetic Neutron Source Coupled Neutron-Photon Transport Demonstration. ....	84

## List of Symbols

Symbol	Description
$\alpha$	Ratio of photon energy to electron rest mass energy, $h\nu / m_0c^2$
$\alpha_f$	Fine structure constant, 1/137.0360
$\beta$	Ratio of electron velocity to speed of light, $v / c$
$\gamma$	Gamma ray
$\theta$	Polar scattering angle
$\mu$	Cosine of polar scattering angle
$\xi$	A random number
$\sigma$	Interaction cross section
$v$	Electron velocity
$\chi$	Watt distribution
$\chi^2$	Chi-squared test statistic
$\omega$	Azimuthal scattering angle
$A$	Atomic mass number
$c$	Speed of light in a vacuum, 299792458 m/s
$C$	A constant
$E$	Energy
$f$	Scaled angular cross section function, $0 \leq f \leq 1$
$g$	Sample space boundary function
$h\nu$	Photon energy
$I$	Electron excitation and ionization potential
$I_\gamma$	Relative gamma emission intensity
$m_0c^2$	Rest mass energy of an electron, $\cong 511$ keV
$N$	Number density
$p$	Probability density function (PDF)
$p_\gamma$	Probability of gamma emission
$P$	Cumulative probability density function (CDF)
$T$	Kinetic energy
$Z$	Atomic number



# RAY NEXT-EVENT ESTIMATOR TRANSPORT OF PRIMARY AND SECONDARY GAMMA RAYS

## I. Introduction

Monte Carlo methods are a popular choice to simulate the transport of neutral particles in a scattering medium from a source to a point of interest. The stochastic nature of neutral particle transport lends itself well to this type of simulation (Zickafoose & Mathews, 2010-2011). Monte Carlo methods rely on sampling from the domain of theoretical behaviors to determine the radiation field at a specified location. To provide a solution of sufficiently low variance, large numbers of particle histories must be sampled, resulting in correspondingly large computation times. Variance reduction schemes can be applied to reduce the number of samples required to converge on an estimate for a particular problem.

### The Air to Space Particle Transport Problem

A particular class of problems, estimation of the free-field flux at a point in a vacuum, hereafter referred to as the flux-point, from a point source in a scattering medium is of interest. The general problem is illustrated in Figure 1.

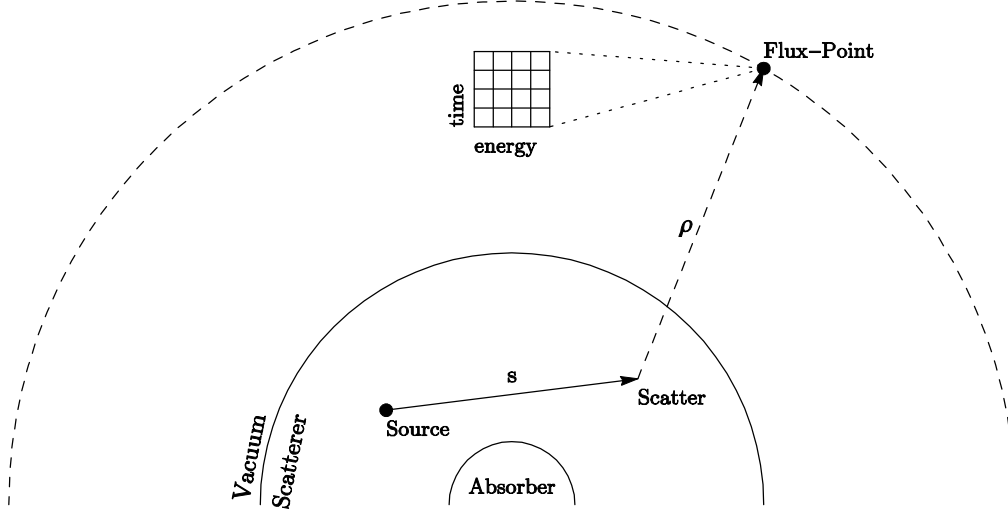


Figure 1. The Transport Problem.

Consider a neutral particle, a neutron or a photon, emitted from a point source in the atmosphere. That particle has energy and direction correlated with the properties of the source. The particle will travel along its path until it interacts with atmospheric nuclei or atomic electrons. Upon interaction, the particle has a probability to scatter to a flux-point in space with a discretized grid in time and energy. That probability is

$$P_{i,j} \left( A \middle| E', \Omega', s \right) = \frac{p \left( \theta(s) \right) e^{-\tau \left( E(E',s), \rho(s) \right)}}{2\pi \left( \rho(s) \right)^2} \text{box} \left( \frac{E(E',s) - E_i}{\Delta E}, \frac{T(E',s) - T_j}{\Delta T} \right) \quad (1)$$

where

$P_{i,j}$  = probability of arrival at the flux point in energy bin  $i$  and time bin  $j$   
 $E'$  = initial energy  
 $\Omega'$  = initial direction  
 $s$  = distance traveled along the path before collision  
 $\theta$  = polar angle between the particle path and a vector to the flux-point at the point of scatter  
 $p$  = the probability of scatter into the angle  $\theta$   
 $\tau$  = optical thickness from the point of scatter to the flux-point  
 $E$  = energy after scatter  
 $\rho$  = distance from the point of scatter to the flux-point  
 $box(\dots)$  = a 2-dimensional normalized boxcar function for a time-energy grid bin with center  $(E_i, T_j)$  and width  $(\Delta E, \Delta T)$ .

This is the next-event estimator (Lux & Koblinger, 1991, p. 380) and is herein referred to as the point next-event estimator. For a given scatter, there is a single probability and time-energy bin to which the particle may contribute. To converge on a solution, the estimator must be applied to a significant number of scattering points sufficiently dispersed throughout the sample domain in energy, position, and time. Sampling of these points is a source of variance in the estimate from the point next-event estimator.

Instead, consider that there is a continuous probability at each point along the ray, the trajectory of the particle, at which the particle might scatter to the flux-point. Depending on the scattering mechanics of the particle along the ray there may be a possibility of reaching multiple time-energy bins at the flux-point from a single ray (Zickafoose & Mathews, 2010-2011). Recognizing that there are continuous segments along each ray from which the particle could scatter to the

flux-point and by treating each ray continuously, instead of only as an endpoint as in the point next-event estimator, a new estimator could eliminate the source of variance from sampling the point of scatter.

## The Ray Next-Event Estimator

The ray next-event estimator is a Monte Carlo method developed by Lt Col Matthew Zickafoose (2010-2011) to improve the efficiency of existing tools and methods for neutron transport computations from a point source in the atmosphere to a flux-point in a vacuum. A purpose-built code accompanied the development of the method for demonstration and comparison to a conventional point next-event estimator. The estimator developed by Zickafoose is

$$P_{i,j} \left( A \middle| E', \Omega', s \right) = \frac{e^{-\tau(E', s_1)}}{4\pi} \int_{s_1}^{s_2} ds \frac{\Sigma_{scat}(s) e^{-[\tau(E', s-s_1) + \tau(E(E', s), \rho(s))]} }{\left( \rho(s) \right)^2} \quad (2)$$

where isotropic scattering is assumed and

$P_{i,j}$  = probability of arrival at the flux-point in energy bin  $i$  and time bin  $j$   
 $E'$  = initial energy  
 $\Omega'$  = initial direction  
 $s_1$  = beginning of a segment of the ray that contributes to energy bin  $i$  and time bin  $j$   
 $s_2$  = end of a segment of the ray that contributes to energy bin  $i$  and time bin  $j$   
 $\tau(E', s_1)$  = optical thickness along the ray to the beginning of the segment  
 $\Sigma_{scat}(s)$  = macroscopic scatter cross section at the point  $s$   
 $\tau(E', s - s_1)$  = optical thickness from  $s_1$  to a point  $s$  on the segment  
 $\tau(E(E', s), \rho(s))$  = optical thickness from the point  $s$  to the flux-point  
 $E$  = energy after scatter at point  $s$   
 $\rho$  = distance from the point  $s$  to the flux-point.

If isotropic scattering cannot be assumed, we recognize that the factor of  $1 / 4\pi$  from (2) becomes  $p(\theta(s)) / 2\pi$  as in the point next-event estimator from Lux (1991, p. 380). The ray next-event estimator is then

$$P_{i,j} \left( A | E', \Omega', s \right) = \frac{e^{-\tau(E', s_1)}}{2\pi} \int_{s_1}^{s_2} ds \frac{p(\theta(s)) \Sigma_{scat}(s) e^{-[\tau(E', s - s_1) + \tau(E(E', s), \rho(s))]} }{(\rho(s))^2} . \quad (3)$$

## Statement of the Research Problem

Incorporate the transport of primary and secondary gamma radiations in the Ray Next-Event Estimator (RNEE) v4.0 Fortran code.

## **Assumptions and Limitations**

The following assumptions and limitations were applied during the course of this research to allow focus to remain on the implementation of gamma ray interactions in the ray next-event estimator.

### **Ray Next-Event Estimation**

The efficacy of the ray next-event estimator was not the subject of this research. The method was demonstrated for neutron transport calculations (Zickafoose & Mathews, 2010-2011), but with appropriate application and inclusion of additional physics data can be generalized for neutral particle transport calculations including photon transport.

### **Neutron Transport Calculations**

Significant changes to the implementation of neutron transport calculations were avoided throughout the research. The implementation of neutron transport physics was assumed to be correct under the assumptions and limitations made by Zickafoose (2010-2011).

### **Atmospheric Representation**

The atmosphere is assumed as the U.S. Standard Atmosphere and is composed of only nitrogen and oxygen with relative concentrations of 74.8488%

and 21.1512% respectively. We assume a constant composition, variable density atmosphere up to an altitude of 86 km. Altitudes greater than 86 km are considered vacuum.

Additional atmospheric constituents can readily be included in the simulation with appropriately processed physics data, but a two element approximation was sufficient for this research. Including atmosphere at altitudes above 86 km would also be possible, with modification to the code, by adding additional atmospheric layers.

### **Geometric Representation**

The orientation of the source, flux-point, and earth are held constant for the duration of the simulation. This limits the application of the model to problems in which the flux-point is distant from the source, as in the case of a source in the atmosphere and a flux-point in geosynchronous orbit, so that their relative motion is small during the simulation. Should the code be applied to problems in which the flux-point is at lower altitudes than geosynchronous orbit, this assumption may not be valid.

### **Photon Interactions**

Photon interactions included in the simulation are coherent scattering, incoherent scattering, photoelectric absorption, and pair production. Other

photon interactions contribute less than 1% to the total interaction cross section for photons and are neglected (Lux & Koblinger, 1991, p. 47).

For coherent scattering, the angular distribution of scattered photons is approximated as the classical Thompson cross section. The actual angular distribution is the product of the Thompson cross section and the atomic form factor (Persliden, 1983, p. 122) which corrects the angular distribution for incident photon energy and the  $Z$  value of the scattering material. The atomic form factor becomes more important at higher energies (Persliden, 1983, p. 122). Because the coherent scatter cross section falls off rapidly with increasing energy and incoherent scatter and pair production interactions dominate at higher energies, the atomic form factor is assumed to have a negligible impact on these transport computations.

For incoherent scattering, the Klein-Nishina approximation for the distribution of scattered photons is assumed without the electron binding correction, also called the incoherent scattering function. The incoherent scattering function corrects the distribution of scattered photons for differences between elements and becomes important for high values of  $Z$  (Persliden, 1983, p. 121). Should the model be extended beyond the two element atmosphere approximation, the incoherent scattering function may need to be included. Discussion and references for the electron binding correction can be found in Lux (1991, p. 46).



For photoelectric absorption interactions, the emission of characteristic x-rays and auger electrons is ignored. Should the estimator be applied to low energy photon transport computations, characteristic x-rays may not be negligible. The photoelectron is considered in the computation if it is ejected with sufficient kinetic energy to emit bremsstrahlung radiation as it decelerates in the scattering medium.

The process of pair production is approximated as the immediate production of two new gamma rays at the site of the interaction. The path length and time of flight of the electron and positron are considered negligible. As in photoelectric absorption, the electron and positron are considered if they are produced if they are produced with sufficient energy to emit bremsstrahlung radiation as they decelerate in the scattering medium.

### **Secondary Gamma Ray Production Interactions**

The model assumed from bremsstrahlung radiation includes the continuous slowing down approximation, that all of the kinetic energy of the decelerating particle is dissipated, and that the radiated energy is emitted as a single coherent photon. These assumptions significantly simplify the model and limit its physical relevance, but implementation in the code provides the infrastructure for a more refined model to be implemented in the future.

The model assumed for neutron absorption assumes that the kinetic energy of the absorbed neutron is directly converted to energy to place the target nucleus in an excited state. Recoil energy of the nucleus is not considered. This limits the physical relevance of the model, but its implementation in the code provides the infrastructure for a more refined model to be implemented in the future.

### **Motion of Nuclei and Charged Particles**

The normal motion of atoms and the motion of recoiling nuclei are considered negligible compared to the space and time scales considered in the problem. The path length of charged particles, electrons and positrons, is also considered negligible when compared to that of neutral particles in the scattering medium.

### **Decay of Excited Nuclei by Gamma Emission**

Cascades of photons emitted in gamma decay processes by nuclei excited in neutron inelastic scatter and other interactions are assumed to be emitted instantaneously after the interaction that excited the nucleus. This assumes that the excited state half-lives and any metastable state half-lives are insignificant compared to the time scale of the simulation.

## **Approach**

The research approach is tailored to allow the focus of this research to remain on application of the ray next-event estimator to gamma ray transport.

1. Adapt the purpose built Ray Next-Event Estimator 4.0 code for gamma ray transport.
2. Apply the Ray Next-Event Estimator code to neutron and photon transport problems.
3. Extend neutron and photon interaction physical models to account for generation of secondary gamma radiation particles for transport computations.
4. Apply the Ray Next-Event Estimator code to coupled neutron-photon transport problems.

## II. Theory

Four types of interactions capture the vast majority of gamma ray interactions in a scattering medium like air. In air, coherent scattering and photoelectric absorption are the dominant processes for photons with energy less than 100 keV. Incoherent scattering dominates photon interactions for energies 100 keV to 10 MeV. Pair production, while not possible for photons with energy less than two electron rest masses or 1.022 MeV, quickly becomes important above 10 MeV. Cross sections for these interactions, as well as the total cross section, for a nitrogen-oxygen-argon mixture that approximates air are plotted in Figure 2.

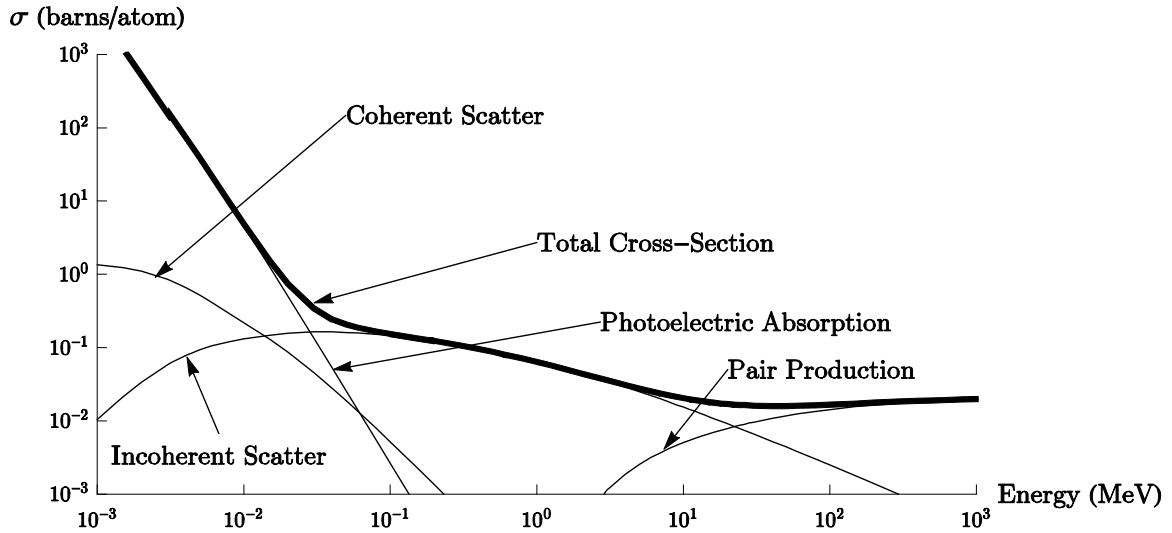
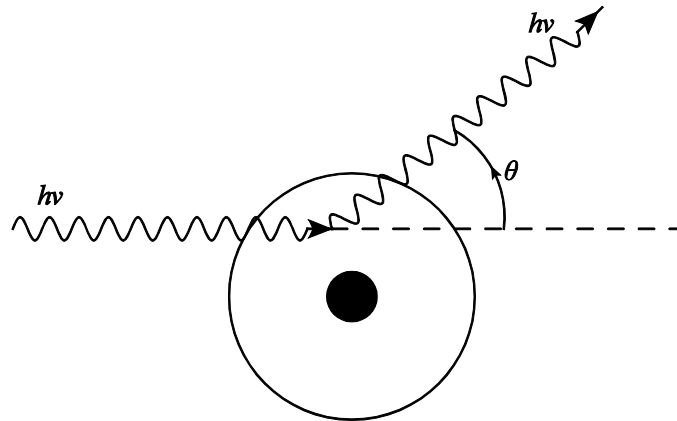


Figure 2. Photon Interaction Cross Sections for a N-O-Ar Mixture Like Air (NIST, 2010).

Other particle interactions can also produce gamma ray photons as a result of the interaction. High energy electrons and positrons produced in other gamma interactions can produce bremsstrahlung radiation photons as they decelerate in the scattering medium. Gamma rays can also be emitted by nuclei left in an excited state from neutron inelastic scatter and neutron absorption interactions.

### Coherent Scattering

Coherent scattering, also called Rayleigh scattering, occurs when a photon interacts coherently with the electrons of a target atom. The photon is absorbed and immediately reemitted from the atom in a different direction but with the same energy as the incident photon (Choppin, Liljenzin, & Rydberg, 2002, p. 143). Figure 3 shows a graphical depiction of a coherent scatter interaction.



**Figure 3. Coherent Scattering.**

The angular distribution is described as the product of the classical Thompson cross section and the atomic form factor,

$$\frac{d\sigma}{d\Omega} = \frac{r_e^2}{2} (1 + \cos^2 \theta) F(q, Z) , \quad (4)$$

where  $r_e$  is the classical electron radius, and  $F(q, Z)$  is the atomic form factor (Lux & Koblinger, 1991, p. 47).

The atomic form factor is dependent on the photon energy and the atomic number of the target atom. Including the atomic form factor in these computations would significantly complicate the model for coherent scattering. We assume the effect of the atomic form factor to be negligible ( $F(q, Z) = 1$ ) to allow the focus of the research to remain on implementation of gamma ray interactions in the code. The atomic form factor becomes more important for higher energy photons (Persliden, 1983, p. 122), but because the cross section for coherent scatter drops rapidly with increasing energy relative to other photon interactions the probability of a high energy coherent scatter interaction is low. References for formulations of the atomic form factor can be found in Lux (1991, p. 46).

The angular distribution of coherently scattered photons, scaled so that  $0 \leq \frac{d\sigma}{d\Omega} \leq 1$ , is plotted in Figure 4 for photons incident from the left.

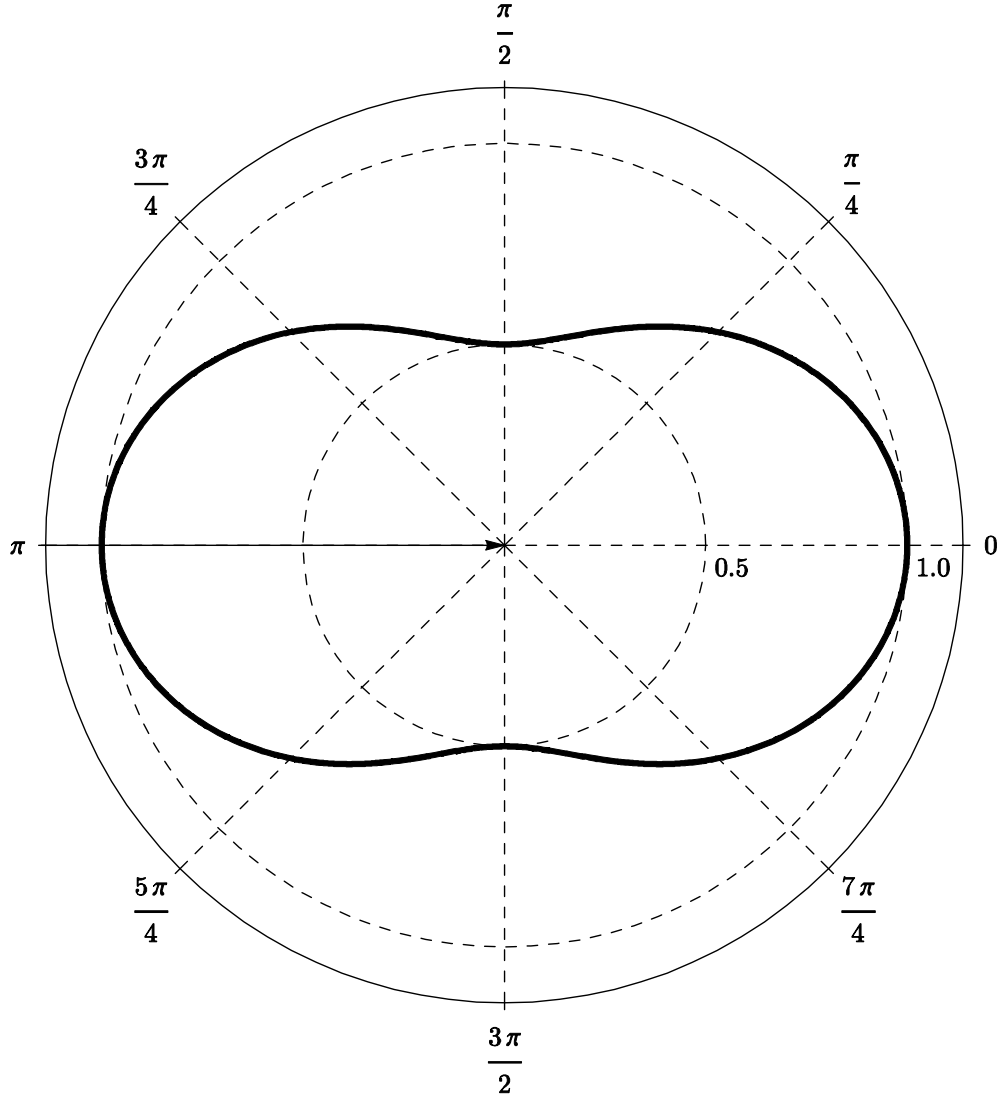


Figure 4. Scaled Angular Distribution of Coherently Scattered Photons Incident from Left.

Because  $\omega$  is assumed to be uniformly distributed from zero to  $2\pi$ , we recognize that  $d\Omega = 2\pi \sin \theta d\theta$  (Lux & Koblinger, 1991, p. 46), (4) becomes

$$\frac{d\sigma}{d\theta} = \pi r_e (1 + \cos^2 \theta) \sin \theta . \quad (5)$$

This is the angular cross section for a differential element of polar scattering angle.

Computationally, it is more appropriate to consider (5) in terms of the cosine of the scattering angle, because all of the subsequent transport calculations use the cosine and not the angle itself. Rearranging (5) we get

$$d\sigma = \pi r_e (1 + \cos^2 \theta) \sin \theta d\theta . \quad (6)$$

If we let  $\mu = \cos \theta$ , then  $|d\mu| = \sin \theta d\theta$  and  $d\theta = \frac{1}{\sin \theta} |d\mu|$ , and (6) becomes

$$d\sigma = \pi r_e (1 + \mu^2) d\mu . \quad (7)$$

The angular cross section for a differential element of  $\mu$  is then

$$\frac{d\sigma}{d\mu} = \frac{r_e}{\pi} (1 + \mu^2) . \quad (8)$$

Scaling  $\frac{d\sigma}{d\mu}$  so that  $0 \leq \frac{d\sigma}{d\mu} \leq 1$  and defining the scaled distribution function,

$f(\mu)$ , gives

$$f(\mu) = \frac{(1 + \mu^2)}{2} . \quad (9)$$

The distribution  $f(\mu)$  is plotted in Figure 5. The scaling step from (8) to (9) is not entirely necessary for the implementation of coherent scatter angular selection. However, scaling the angular distribution function will be convenient for the implementation of incoherent scatter scattering angle selection later.



Forgoing the change from (8) to (9) and defining  $f(\mu) = \frac{d\sigma}{d\mu} = -\frac{r_e}{\pi}(1 + \mu^2)$  does not change the results of the implementation for coherent scatter scattering angle selection.

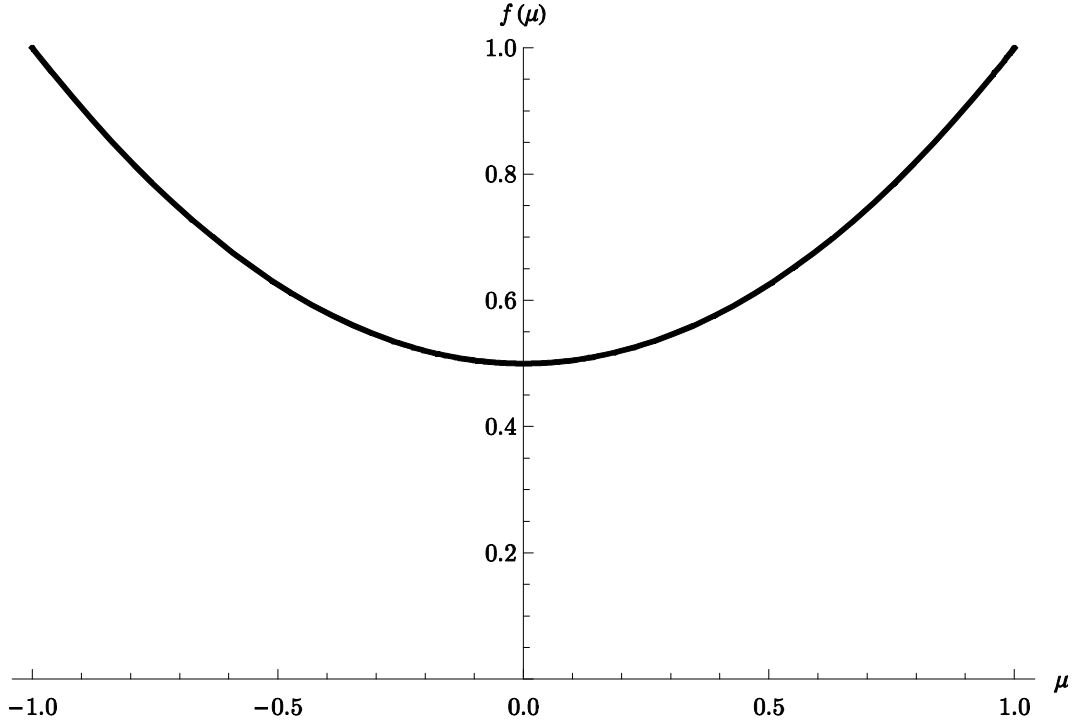


Figure 5. Distribution of the Cosine of the Scattering Angle for Coherently Scattered Photons.

## Photoelectric Absorption

Photoelectric absorption occurs when a gamma ray photon is fully absorbed by an absorber atom and causes the ejection of an electron, called a photoelectron, from a bound shell of the atom. The kinetic energy,  $T$ , of the photoelectron is

$$T = hv - E_b \quad (10)$$

where  $E_b$  is the binding energy of the photoelectron in its original bound shell (Knoll, 2000, p. 309). The resulting ionized absorber atom may also emit one or more characteristic x-ray photons or an Auger electron as electrons from other bound shells rearrange to fill the vacancy left by the ejected photoelectron (Knoll, 2000, p. 309). Figure 6 depicts the photoelectric absorption process.

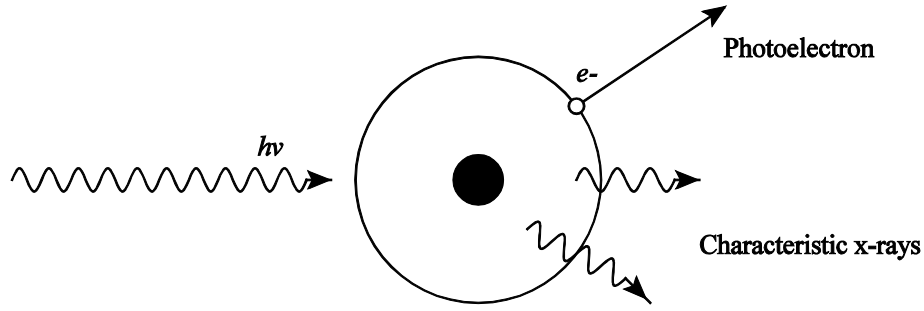


**Figure 6. Photoelectric Absorption.**

For the purposes of this research, we assume that the angular distribution of photoelectrons is isotropic and that characteristic x-rays and auger electrons are negligible. These assumptions simplify the model for photoelectric absorption to allow the focus of the research or remain on implementation of gamma ray interactions in the code.

## Incoherent Scattering

Incoherent scattering, also known as Compton scattering, occurs when an incident photon interacts with an electron in the scattering medium. The incident photon transfers some of its energy to the electron and is scattered through an angle  $\theta$  (Knoll, 2000, p. 310) as shown in Figure 7.

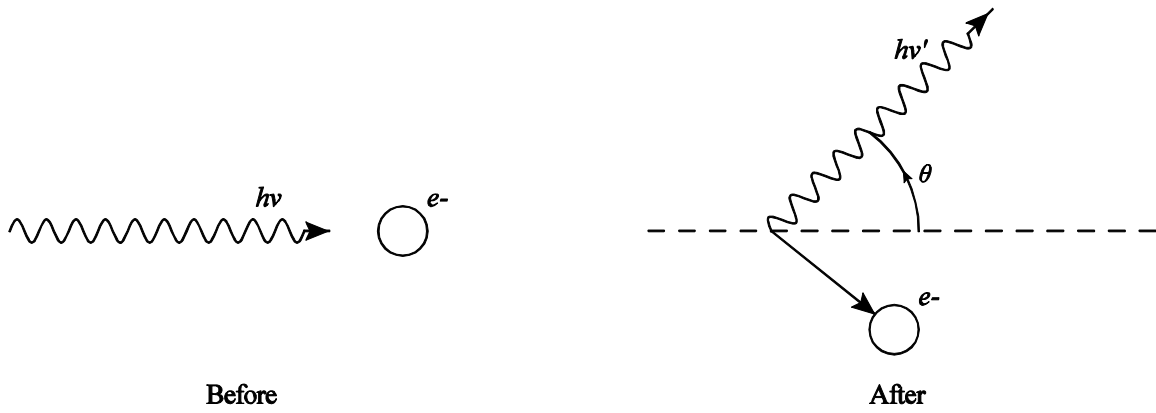


Figure 7. Incoherent Scattering.

The energy of the scattered photon is

$$h\nu' = \frac{h\nu}{1 + \alpha(1 - \cos \theta)} \quad (11)$$

where  $h\nu'$  is the energy of the scattered photon,  $h\nu$  is the energy of the incident photon, and  $\alpha \equiv h\nu / m_0c^2$ ; the ratio of incident photon energy to the rest mass energy of the electron (Knoll, 2000, p. 310). The kinetic energy,  $T$ , of the recoil electron is

$$T = h\nu - h\nu' \quad . \quad (12)$$

The angular distribution of scattered photons is approximated by the Klein-Nishina formula,

$$\frac{d\sigma}{d\Omega} = Zr_e^2 \left( \frac{1}{1 + \alpha(1 - \cos \theta)} \right)^2 \left( \frac{1 + \cos^2 \theta}{2} \right) \left( 1 + \frac{\alpha^2 (1 - \cos \theta)^2}{(1 + \cos^2 \theta)[1 + \alpha(1 - \cos \theta)]} \right), \quad (13)$$

where  $Z$  is the atomic number of the scattering medium (Knoll, 2000, p. 51).

The angular distribution of incoherently scattered photons, scaled so that

$0 \leq \frac{d\sigma}{d\Omega} \leq 1$ , is plotted in Figure 8 for photons incident from the left and several

values of  $\alpha$ . Recalling that  $\alpha \equiv h\nu / m_0 c^2$ , so that larger values for  $\alpha$

correspond to higher incident photon energies, note the strong tendency for

forward scattering for higher photon energies.

This model for incoherent scattering assumes that the electron with which the incident photon interacts is initially unbound and at rest. In reality, most electrons in a scattering medium meet neither of these criteria. It is possible to refine the Klein-Nishina approximation using electron binding corrections or incoherent scattering functions, but generally unnecessary for practical transport computations (Lux & Koblinger, 1991, p. 46). Electron binding corrections and incoherent scattering functions are not considered here in order to allow the focus of the research to remain on the implementation of gamma ray transport in the code.

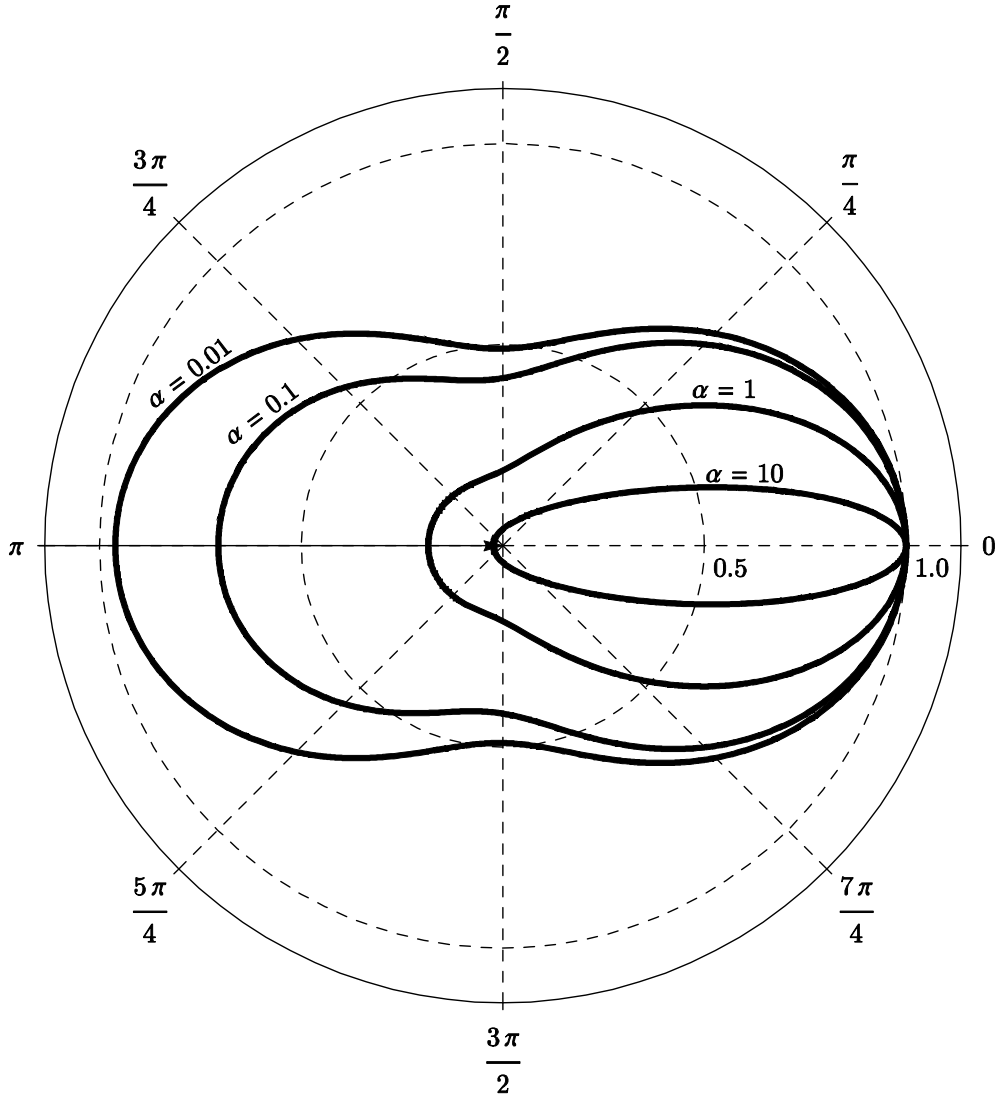


Figure 8. Scaled Angular Distribution of Incoherently Scattered Photons of Various Energies Incident from Left.

As before, we recognize that  $d\Omega = 2\pi \sin \theta d\theta$  (Lux & Koblinger, 1991, p. 46), (13) becomes

$$\frac{d\sigma}{d\theta} = 2\pi Zr_e^2 \left( \frac{1}{1 + \alpha(1 - \cos \theta)} \right)^2 \left( \frac{1 + \cos^2 \theta}{2} \right) \times \left( 1 + \frac{\alpha^2 (1 - \cos \theta)^2}{(1 + \cos^2 \theta) [1 + \alpha(1 - \cos \theta)]} \right) \sin \theta . \quad (14)$$

This is the angular cross section for a differential element of polar scattering angle.

As before, it is computationally more appropriate to consider (14) in terms of the cosine of the scattering angle, because all of the subsequent transport calculations use the cosine and not the angle itself. Rearranging (14) gives

$$d\sigma = 2\pi Zr_e^2 \left( \frac{1}{1 + \alpha(1 - \cos \theta)} \right)^2 \left( \frac{1 + \cos^2 \theta}{2} \right) \times \left( 1 + \frac{\alpha^2 (1 - \cos \theta)^2}{(1 + \cos^2 \theta) [1 + \alpha(1 - \cos \theta)]} \right) \sin \theta d\theta . \quad (15)$$

If we let  $\mu = \cos \theta$ , then  $|d\mu| = \sin \theta d\theta$  and  $d\theta = \frac{1}{\sin \theta} |d\mu|$ , and (15) becomes

$$d\sigma = \frac{Zr_e^2}{2\pi} \left( \frac{1}{1 + \alpha(1 - \mu)} \right)^2 \left( \frac{1 + \mu^2}{2} \right) \left( 1 + \frac{\alpha^2 (1 - \mu)^2}{(1 + \mu^2) [1 + \alpha(1 - \mu)]} \right) d\mu . \quad (16)$$

Angular cross section for a differential element of  $\mu$  is then

$$\frac{d\sigma}{d\mu} = \frac{Zr_e^2}{2\pi} \left( \frac{1}{1 + \alpha(1 - \mu)} \right)^2 \left( \frac{1 + \mu^2}{2} \right) \left( 1 + \frac{\alpha^2 (1 - \mu)^2}{(1 + \mu^2) [1 + \alpha(1 - \mu)]} \right) . \quad (17)$$

Scaling  $\frac{d\sigma}{d\mu}$  so that  $0 \leq \frac{d\sigma}{d\mu} \leq 1$  and defining the scaled distribution function,

$f(\mu; \alpha)$ , gives

$$f(\mu; \alpha) = \left( \frac{1}{1 + \alpha(1 - \mu)} \right)^2 \left( \frac{1 + \mu^2}{2} \right) \left( 1 + \frac{\alpha^2 (1 - \mu)^2}{(1 + \mu^2)[1 + \alpha(1 - \mu)]} \right). \quad (18)$$

The distribution  $f(\mu; \alpha)$  is plotted for several values of  $\alpha$  in Figure 9.

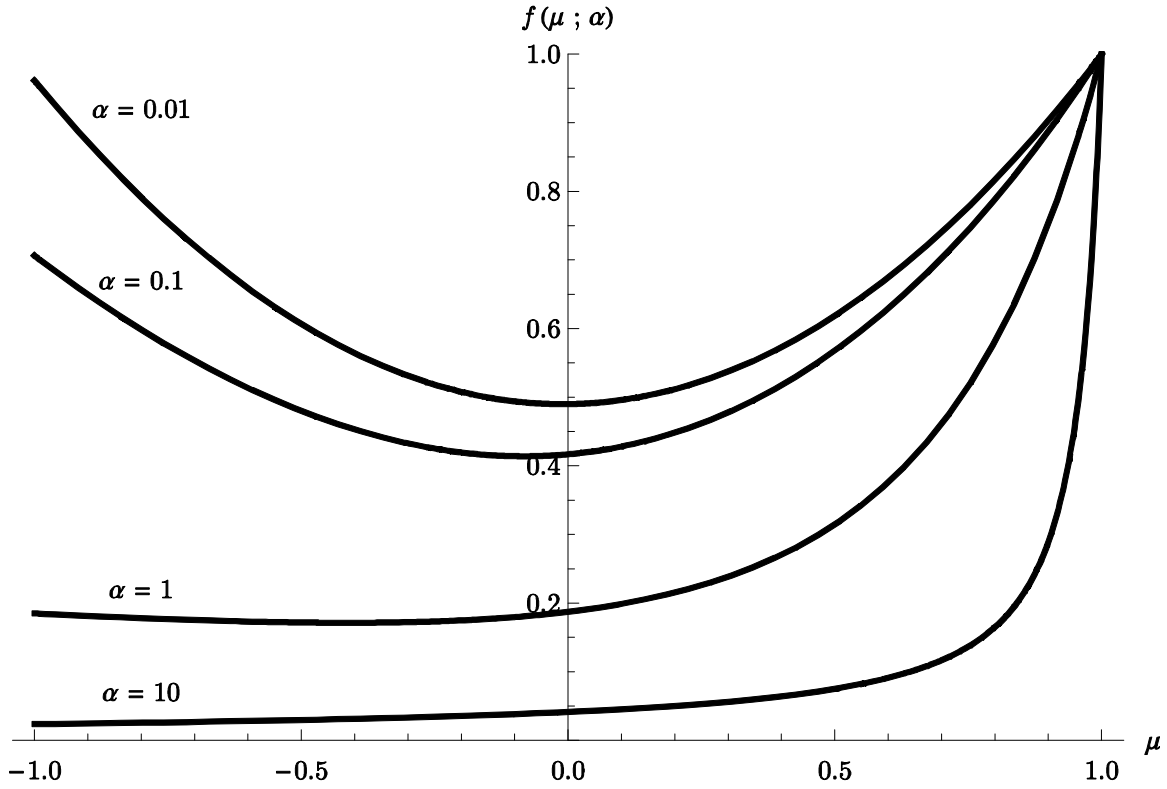


Figure 9. Distribution of the Cosine of the Scattering Angle for Incoherently Scattered Photons of Various Energies.

## Pair Production

In pair production, a gamma ray interacts within the coulomb field of a nucleus or the atomic electrons and transitions into an electron-positron pair (Knoll, 2000, p. 312). To create an electron-positron pair, the incident photon must have energy greater than two electron rest masses or 1.022 MeV. Any energy in excess of 1.022 MeV is converted to kinetic energy shared by the resulting electron-positron pair (Knoll, 2000, p. 312).

The positron created in the pair production interaction subsequently decelerates and annihilates with an electron in the scattering medium releasing the mass energy of the positron and electron in the form of two 511 keV gamma photons (Knoll, 2000, p. 52). These secondary photons have opposite directions of travel that are uncorrelated to the direction of the original photon (Lux & Koblinger, 1991, p. 47). Figure 10 depicts a pair production interaction and subsequent annihilation.

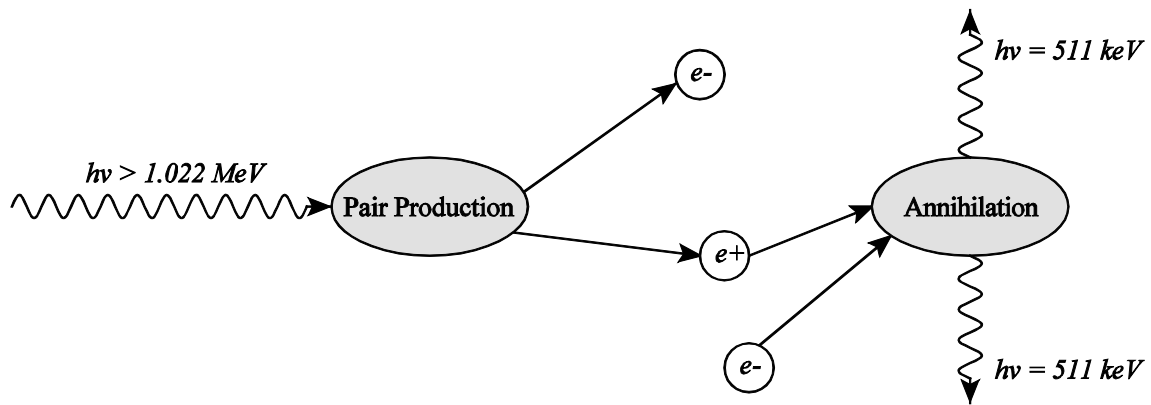


Figure 10. Pair Production.



Pair production is in fact a much more complicated process, but this model is adequate for practical transport calculations. A more detailed description can be found in the article by Hubbell (1980).

## Bremsstrahlung Radiation

Photoelectric absorption, incoherent scattering, and pair production interactions have potential to produce high energy electrons. As an electron moves through a scattering medium, it can be deflected through large angles by collisions with other electrons. Because charged particles radiate electromagnetic energy when accelerating, the decelerating electron emits radiation along its path (Krane, 1988, p. 196). This radiation is called *bremsstrahlung*, German for *braking*, radiation. A simplified model for production of photons by bremsstrahlung interactions is presented here and implemented in the code. The model assumes the continuous slowing down approximation for the charged particle and that the radiated energy is emitted as a single coherent photon.

The energy radiated per unit path length is given by

$$-\left(\frac{dE}{dx}\right)_r = \frac{\alpha_f N E Z (Z + 1) e^4}{(m_0 c^2)^2} \left( 4 \ln \frac{2E}{m_0 c^2} - \frac{4}{3} \right) \quad (19)$$

where  $\alpha_f$  is the fine structure constant,  $N$  is the number density of the scattering medium, and  $E$  is the energy of the incident electron (Knoll, 2000, p. 44).

Electrons also dissipate energy along their path as they collide with other particles in the scattering medium. Energy loss per unit path length due to collisions is

$$-\left(\frac{dE}{dx}\right)_c = \frac{2\pi e^4 NZ}{m_0 v^2} \left( \ln \frac{m_0 v^2}{2I^2(1-\beta^2)} - (\ln 2) \left( 2\sqrt{1-\beta^2} - 1 + \beta^2 \right) + (1-\beta^2) + \frac{1}{8} \left( 1 - \sqrt{1-\beta^2} \right)^2 \right) \quad (20)$$

where  $\beta = v / c$  and  $I$  is the empirically determined electron excitation and ionization potential of the target atom (Knoll, 2000, p. 44).

The total energy loss per unit path length, or stopping power of the scattering medium, is

$$\frac{dE}{dx} = \left(\frac{dE}{dx}\right)_c + \left(\frac{dE}{dx}\right)_r . \quad (21)$$

Determining the range of an electron in a scattering medium can be accomplished by integrating both the radiative and collisional energy losses over the path of the electron. As a result of the erratic nature of the path of the scattered electron, this is a difficult process (Krane, 1988, p. 197). Instead, range to incident energy relationships can be estimated from empirical data (Krane, 1988, pp. 197-198).

Bremsstrahlung radiation is small for electrons traveling at non-relativistic speeds or energy below 1 MeV (Krane, 1988, p. 196). For relativistic electrons, the ratio of radiative losses to collisional losses can be estimated by

$$\frac{\left(\frac{dE}{dx}\right)_r}{\left(\frac{dE}{dx}\right)_c} = \frac{T + m_0 c^2}{m_0 c^2} \frac{Z}{1600} \quad (22)$$

where  $T$  is the kinetic energy of the incident electron (Krane, 1988, p. 197).

## Decay of Excited Nuclei by Gamma Emission

The atomic nucleus can be excited to higher energy states, or levels, in neutron and other interactions. These excited states decay by a number of processes including the emission of gamma rays. A simplified model of the gamma emission process is presented here that is sufficient for this research, but is in no way a complete model for the process. A more complete discussion of gamma decay of nuclear excited states may be found in Krane (1988).

Gamma decay modes of nuclear excited states are different for each element and each isotope of that element. A graphical depiction of the different energy levels is often referred to as a *level scheme*. The level scheme for  $^{14}\text{N}$  is shown in Figure 11. Each excited state, or level, is labeled with its energy in keV, and downward arrows indicate gamma emissions as the excited nucleus transitions from one excited state to another.

Properties of the nucleus and quantum mechanical principles prohibit particular energy transitions and determine half-lives between transitions, and there are many models to explain emission behavior. In short, there are multiple

emission chains that can be followed from one excited state down to the lowest energy state available. Each of these chains has a relative intensity or likelihood of occurring. Empirical data on the decay of nuclear excited states is available in tabular format from the Nudat 2.5 database (NNDC, 2010).

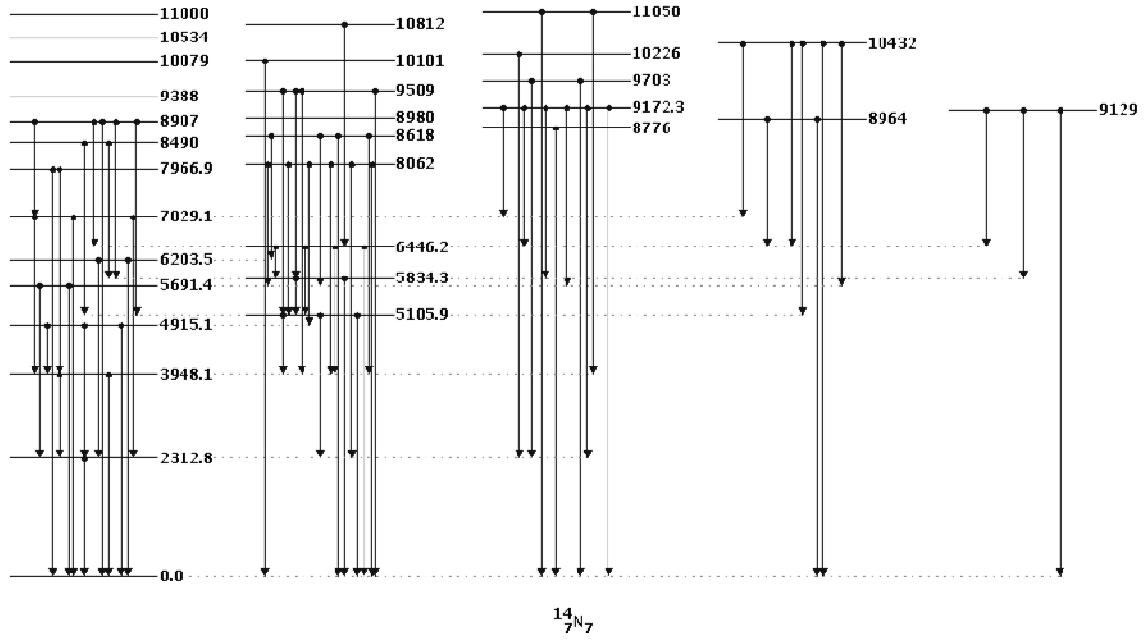


Figure 11. Level Scheme and Decay Gammas for  $^{14}\text{N}$ , energy levels in keV. (NNDC, 2010)

### **III. Methodology**

The Ray Next-Event Estimator (RNEE) v4.0.3 code was written in Fortran 2003 using the Microsoft Visual Studio 2005 development environment and the Intel Fortran compiler v9.1.023. The final version produced in the course of this research was RNEE v5.1.05, developed and compiled in Microsoft Visual Studio 2008 using the Intel Fortran compiler v12.0.2.154.

#### **RNEE Transport of Speed-of-Light Neutral Particles**

The existing method for ray estimation is well suited for adaptation to the purpose of gamma ray transport calculations. Computational transport of speed of light neutral particles is largely similar to computational neutron transport. The two fundamental differences between neutron and photon transport are that photon velocity is independent of energy and always equal to the speed of light, and that photon interactions with matter follow different physical models than neutron interactions.

#### **Implementation of Gamma Ray Interaction Physics**

The physical models of gamma interactions are used by the code for three main computations:

1. Drawing the scattering angle from the appropriate angular distribution for instances where the scattering angle is unknown.
2. Determination of the likelihood of scattering, angular density, into a particular scattering angle when that angle is known.
3. Determination of the particle energy after a scattering interaction when the scattering angle is known.

### **Scattering Angle Selection**

The dependence of the scattering angle distributions on the energy of the incident particle is one of the primary differences between the transport of photons and isotropically scattered neutrons as implemented in RNEE v4.0. In the three-dimensional representation of the photon interaction, the scattering angle is defined by two angles;  $\theta$ , the polar scattering angle, and  $\omega$ , the azimuthal scattering angle. The polar scattering angle is the angle between the incident and departure photon velocity vectors in the plane defined by those vectors. The azimuthal scattering angle is the angle of rotation about the incident photon velocity vector. In general,  $\theta$  is the angle to which the energy dependent angular distributions apply and is drawn from these distributions on the interval zero to  $\pi$ . The azimuthal angle,  $\omega$ , is drawn uniformly from the interval zero to  $2\pi$ . Although properties of the gamma ray and the scattering medium, such as polarization, may impact the distribution of  $\omega$ , uniform selection of this angle is appropriate for these general transport calculations.

## Coherent Scattering

Recall the scaled distribution function for coherently scattered photons in terms of the cosine of the scattering angle:

$$f(\mu) = \frac{(1 + \mu^2)}{2} .$$

We convert  $f(\mu)$  to a probability density function (PDF),  $p(\mu)$ , by

$$p(\mu) = \frac{f(\mu)}{\int_{-1}^1 f(\mu) d\mu} = \frac{3}{8}(1 + \mu^2) . \quad (23)$$

The PDF,  $p(\mu)$ , can be converted to a cumulative probability density function (CDF),  $P(\mu)$ , by

$$P(\mu) = \int_{-1}^{\mu} p(\mu') d\mu' \quad (24)$$

where  $\mu'$  is a dummy variable of integration. This gives

$$P(\mu) = \frac{1}{8}(4 + 3\mu + \mu^3) . \quad (25)$$

Figure 12 shows plots of the PDF and CDF for the distribution of the cosine of the scattering angle for coherent scattering.

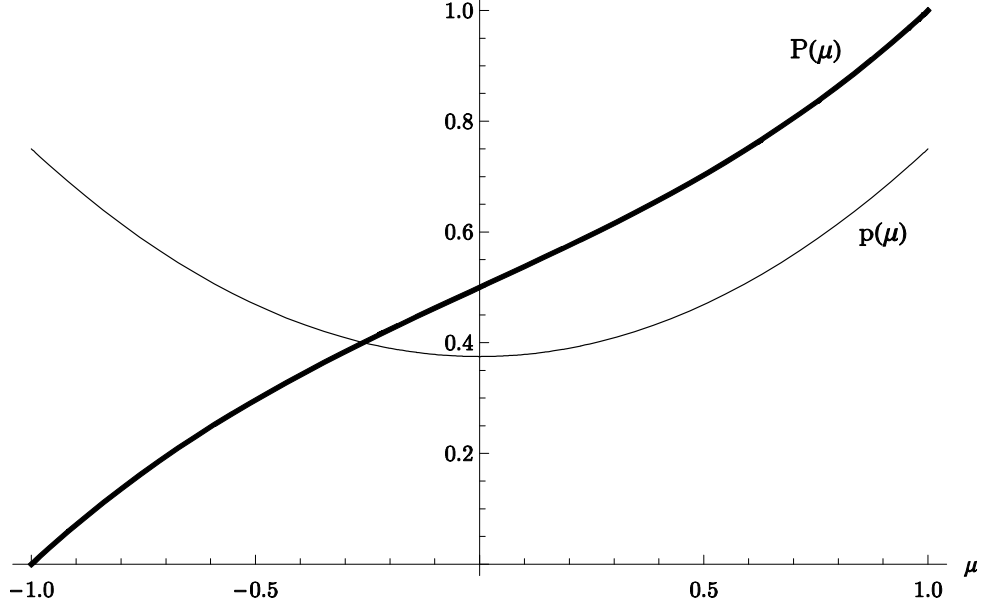


**Figure 12. PDF and CDF for the Distribution of the Cosine of the Polar Scattering Angle for Coherently Scattered Photons.**

To sample  $\mu$ , we draw a random number,  $\xi$ , uniformly distributed between zero and one and evaluate  $P^{-1}(\xi)$  to find  $\mu$ . Evaluation of  $P^{-1}(\xi)$  can be accomplished by root-solving or, if  $P(\mu)$  is invertible, direct computation. The  $P(\mu)$  in (25) can be directly inverted and has three roots, one real and two imaginary. Because the imaginary roots represent non-physical values for  $\mu$ , only the real root is relevant:

$$\mu = P^{-1}(\xi) = \frac{1 - \left(2 - 4\xi + \sqrt{5 + 16\xi(\xi - 1)}\right)^{2/3}}{\left(2 - 4\xi + \sqrt{5 + 16\xi(\xi - 1)}\right)^{1/3}}. \quad (26)$$

This allows us to compute appropriately distributed cosines for the scattering angle of coherently scattered photons. Figure 13 shows the cumulative



distribution of 100,000 angle cosines drawn by the estimator code along with a line representing the cumulative probability density function.

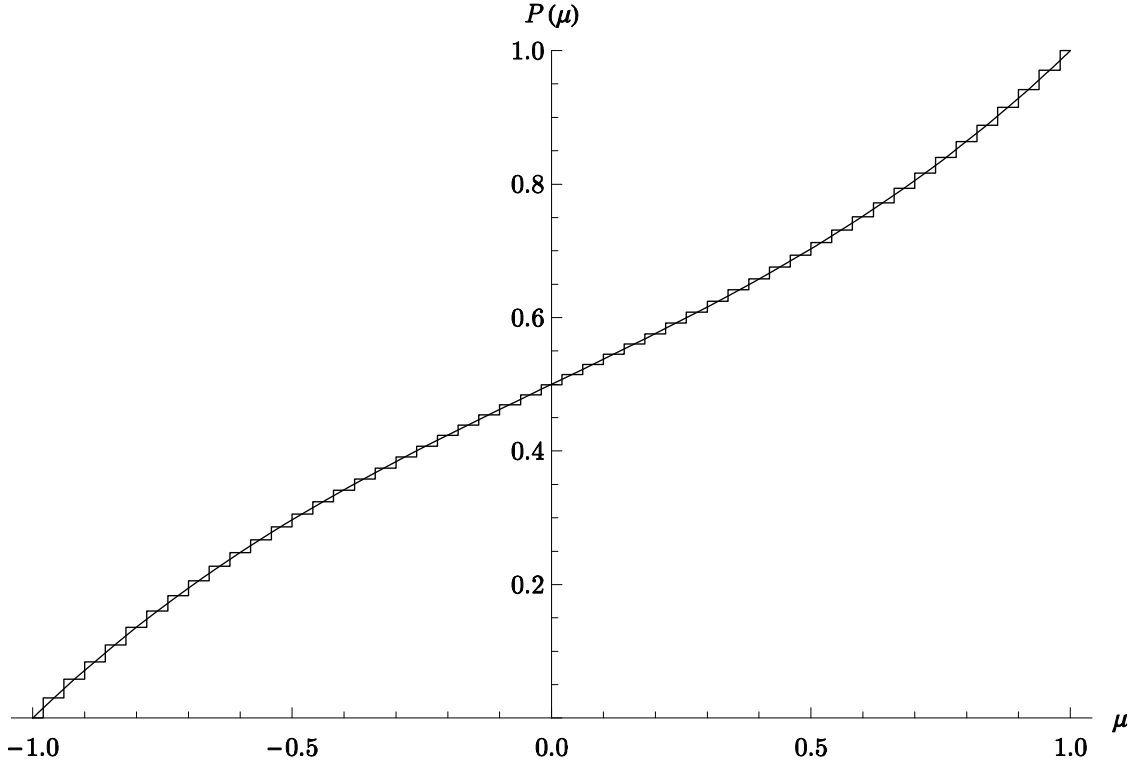


**Figure 13. Distribution of 100,000 Angle Cosines Drawn by the Estimator Code Compared to the Angle Cosine CDF for Coherent Scattering.**

To verify that the angle cosines were drawn from the correct distribution, we apply a statistical test for goodness of fit. We choose the Chi-squared ( $\chi^2$ ) test for simplicity and readily available tables of critical values. The  $\chi^2$  test statistic is

$$\chi^2 = \sum_{i=1}^k \frac{(O_i - NF_i)^2}{NF_i} \quad (27)$$

where  $k$  is the number of bins into which the data are sorted,  $O_i$  is the number of samples in the bin  $i$ ,  $N$  is the total number of samples, and  $F_i$  is the expected fraction of samples in bin  $i$ . The null hypothesis is that the data are from the distribution  $F$ . The alternate hypothesis is that the data are from a distribution other than  $F$ . If the test statistic is greater than the upper critical value or less than the lower critical value for the desired level of confidence and number of degrees of freedom, we reject the null hypothesis with the specified level of confidence.

The 100,000 angle cosines drawn by the code were sorted into 50 equally spaced bins, the  $\chi^2$  test was applied, and we accepted the null hypothesis. The results of the  $\chi^2$  test are shown in Table 1.

**Table 1. Results of Chi-Squared Test for Fit of 100,000 Angle Cosines Drawn by the Code for Coherent Scattering.**

$\chi^2$	Critical Values (90% confidence, 49 DoF)		Accept Null Hypothesis?
	Upper	Lower	
48.64	66.34	33.93	Yes

### Incoherent Scattering

Recall the scaled distribution function for incoherently scattered photons in terms of the cosine of the scattering angle:

$$f(\mu; \alpha) = \left( \frac{1}{1 + \alpha(1 - \mu)} \right)^2 \left( \frac{1 + \mu^2}{2} \right) \left( 1 + \frac{\alpha^2(1 - \mu)^2}{(1 + \mu^2)[1 + \alpha(1 - \mu)]} \right).$$

Converting  $f(\mu; \alpha)$  to a PDF and CDF is complicated and the resulting functions are not easily conditioned for computational applications. The resulting CDF must be recomputed for a new value of  $\alpha$  for each interaction and is also not easily inverted, increasing the computational cost and necessitating an iterative root-solving method to sample  $\mu$ .

To avoid complicated implementation and the high computing cost associated with attempting to evaluate  $P^{-1}(\xi)$  for the Klein-Nishina distribution, a simpler approach is to use a method called sampling by rejection. Sampling by rejection trades the cost of evaluating  $P^{-1}(\xi)$  for the cost of generating extra random numbers (Lewis & Miller, 1993, p. 303).

To sample from  $f(\mu; \alpha)$  we draw a pair of random numbers each uniformly distributed from zero to one,  $\xi_1'$  and  $\xi_2'$ . We then scale  $\xi_1'$  and  $\xi_2'$  to represent a point,  $\{\xi_1, \xi_2\}$ , in the sample space for  $f(\mu; \alpha)$ ;  $-1 \leq \xi_1 \leq 1$  and  $0 \leq \xi_2 \leq 1$ . We then evaluate  $f(\mu; \alpha)$  at  $\xi_1$ , and if  $\xi_2 \leq f(\xi_1; \alpha)$  then we accept  $\xi_1$  as a value for  $\mu$ . If  $\xi_2 > f(\xi_1; \alpha)$ , we reject  $\xi_1$  and draw a new random point from the sample space to test. Figure 14 illustrates the sampling by rejection process for two points from  $f(\mu; \alpha = 0.2)$ . Points drawn in the shaded region are rejected.

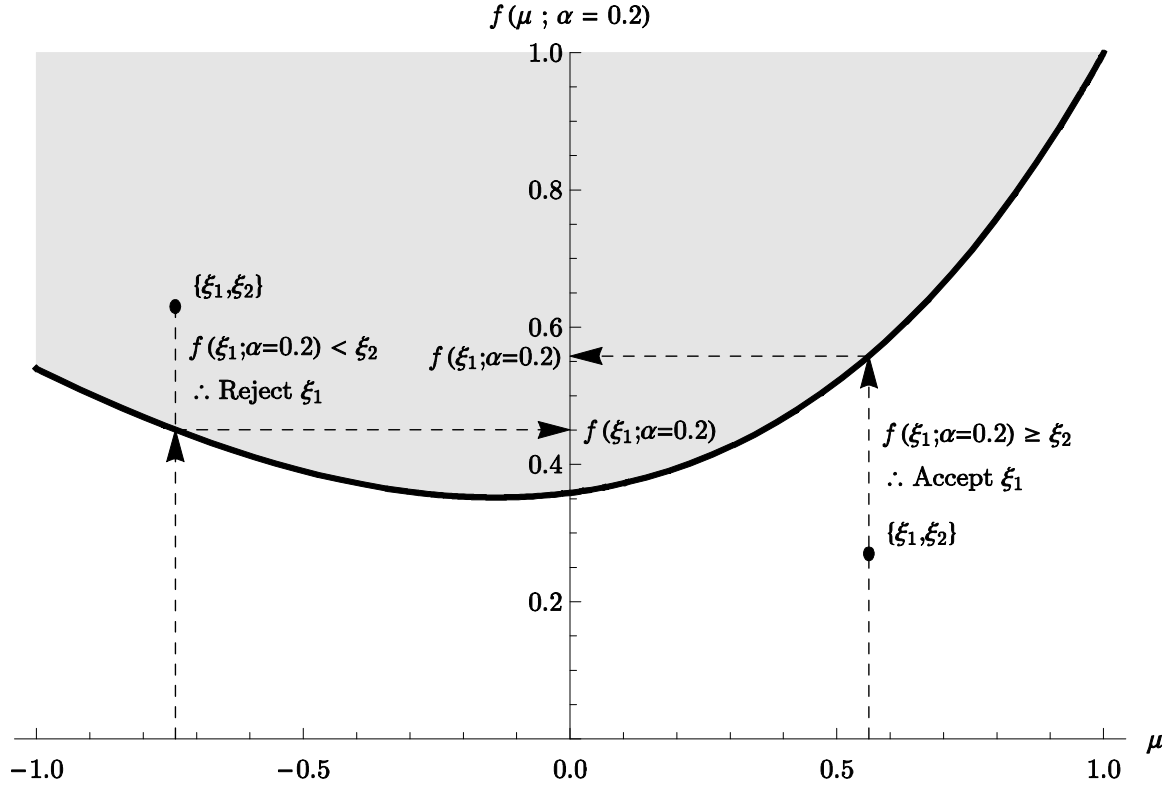


Figure 14. Sampling by Rejection from the Klein-Nishina Distribution.

The sampling efficiency,  $\eta$ , is the ratio of the area of the sample space to the area below the distribution curve. Recalling from Figure 9 that the shape of the distribution changes with  $\alpha$ , we can define the sampling efficiency

$$\eta(\alpha) = \frac{\int_{-1}^1 f(\mu; \alpha) d\mu}{\int_{-1}^1 1 d\mu} \quad (28)$$

Figure 15 shows a plot of sampling efficiency as a function of  $\alpha$ .

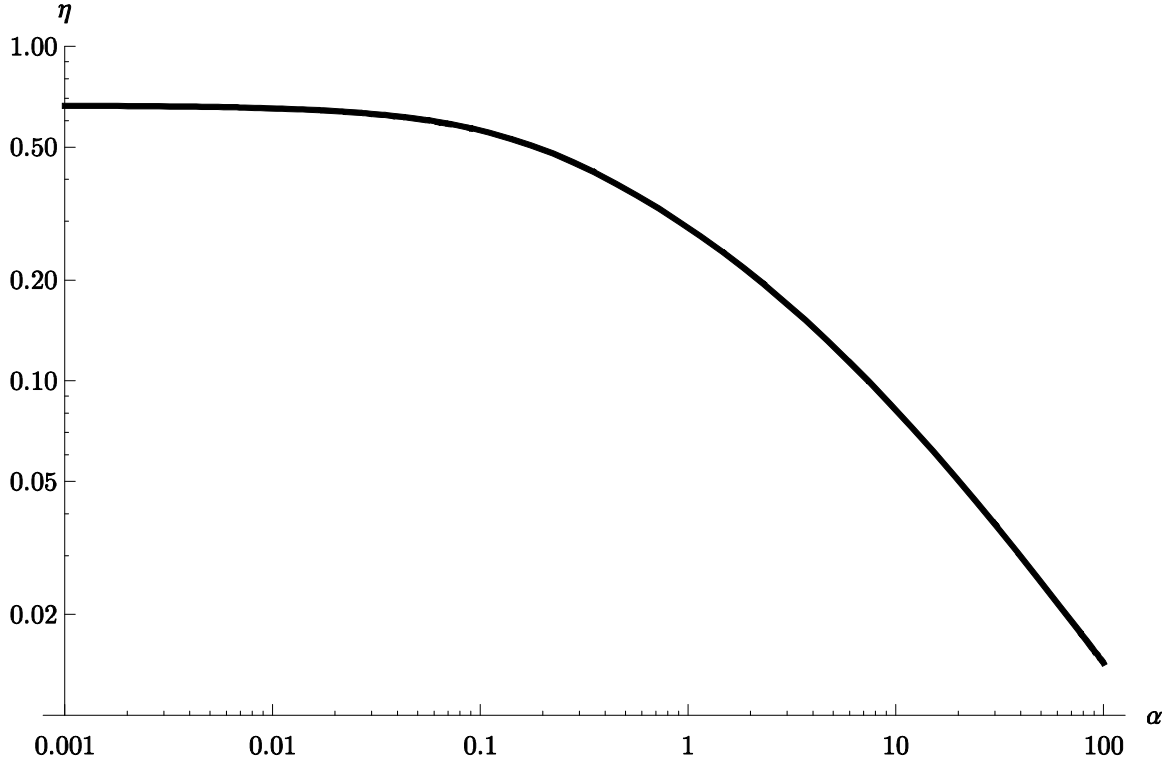


Figure 15. Sampling Efficiency for Basic Sampling by Rejection from the Klein-Nishina Distribution.

Graphical inspection of  $\eta(\alpha)$  immediately suggests that the maximum efficiency is significantly less than unity. In fact,  $\lim_{\alpha \rightarrow 0} \eta(\alpha) = 2/3$ : The maximum efficiency for sampling by rejection using this method is 66% for only the lowest energy photons. As energy of the incident photon increases, the sampling efficiency falls rapidly.

A simple improvement to the rejection sampling method outlined above is to exclude from the sample space any points that are guaranteed to be rejected. Consider the limit of  $f(\mu; \alpha)$  as  $\alpha$  approaches zero:

$$g(\mu) = \lim_{\alpha \rightarrow 0} f(\mu; \alpha) = \frac{(1 + \mu^2)}{2} . \quad (29)$$

Any points selected in the sample space above this curve will be rejected for any distribution with positive  $\alpha$ . We can eliminate these rejections by bounding the sample space to exclude these samples from the beginning of the sampling process.

Conveniently, (29) is the same distribution as previously discussed for the coherent scatter angular distribution, (9). Drawing  $\xi_1'$  and  $\xi_2'$  each uniformly between zero and one, we draw  $\xi_1$  from the distribution  $g(\mu)$  by evaluating (26) at  $\xi_1'$ . The second random number,  $\xi_2$ , is then found by multiplying  $\xi_2'$  by  $g(\xi_1)$  to scale the sample height below the sample space bounding function,  $g(\mu)$ . Figure 16 illustrates sampling by rejection in the new sample space. Note the significantly smaller rejection region (shaded) than in Figure 14.

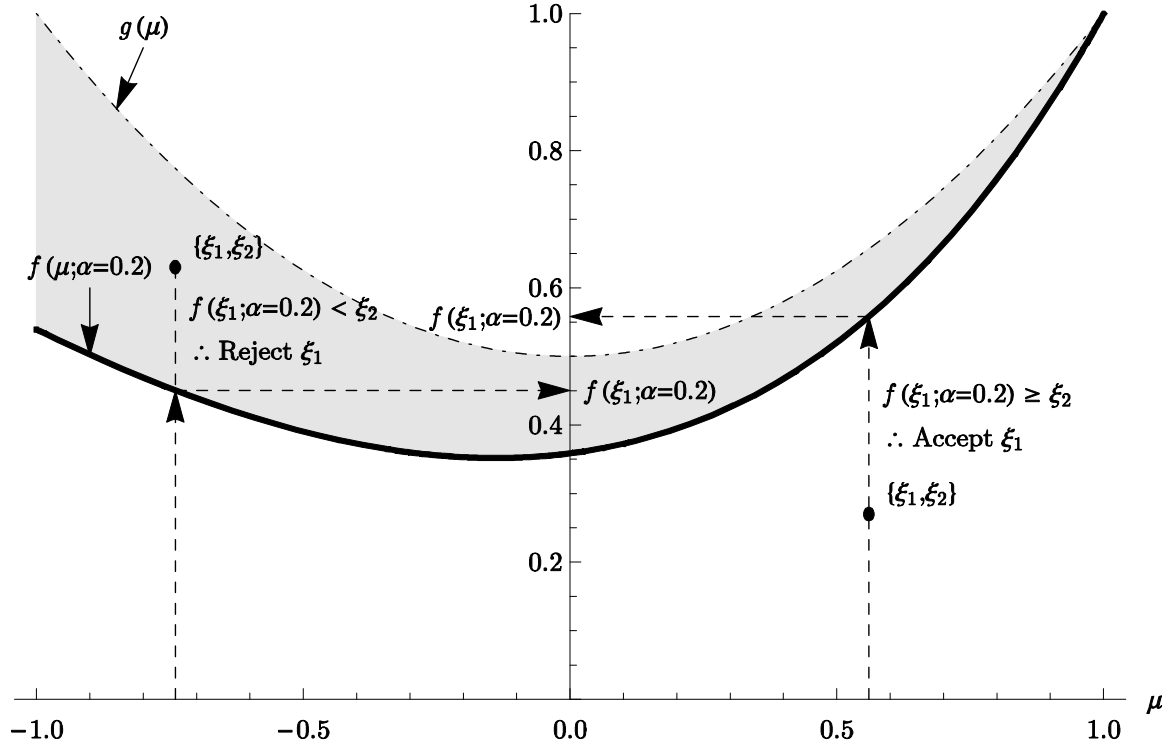


Figure 16. Sampling by Rejection from Bounded Sample Space from the Klein-Nishina Distribution.

Sampling efficiency for the method using the bounded sample space is

$$\eta(\alpha) = \frac{\int_{-1}^1 f(\mu; \alpha) d\mu}{\int_{-1}^1 g(\mu) d\mu} \quad (30)$$

The sampling efficiency for sampling by rejection from the bounded sample space is plotted in Figure 17.

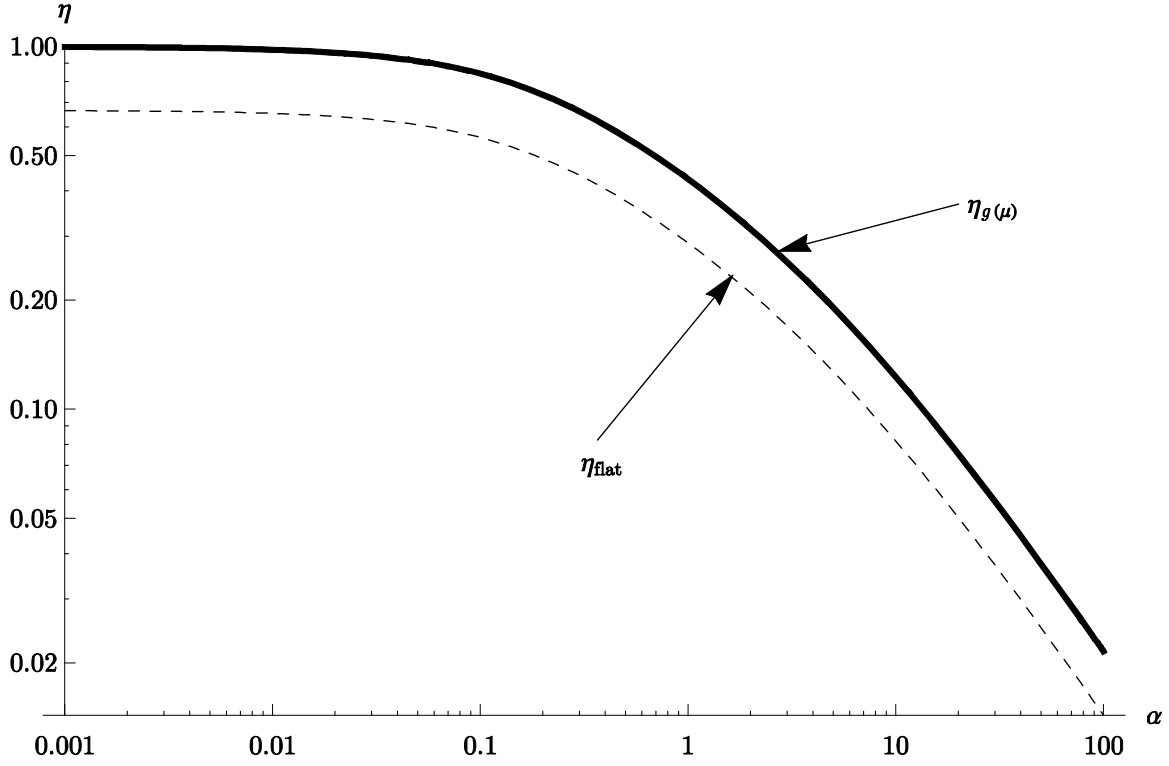


Figure 17. Sampling Efficiency for Improved Sampling by Rejection from the Klein-Nishina Distribution.

While the maximum efficiency,  $\lim_{\alpha \rightarrow 0} \eta(\alpha)$ , is now equal to unity, this method still quickly becomes inefficient for even moderately large values of  $\alpha$ .

The function used to bound the sample space,  $g(\mu)$ , need not be independent of  $\alpha$ . In fact, a boundary function that would adjust its shape according to  $\alpha$  could greatly improve sampling efficiency for higher values of  $\alpha$ . The boundary function must meet two requirements:  $g(\mu) \geq f(\mu)$  for all  $\mu$  in the sampling interval, and it must be possible to sample from the distribution  $g(\mu)$ . Preferably,  $g(\mu)$  has a form of its CDF that is invertible and can be



evaluated with little computational cost, so that the cost of sampling from  $g(\mu)$  will not diminish the improvement in efficiency to the sampling by rejection process. The boundary function  $g(\mu) = \lim_{\alpha \rightarrow 0} f(\alpha, \mu)$  provides sufficient improvement to the sampling by rejection process for this research.

Table 2 compares the observed rejection sampling efficiency for the 100,000 selected angle cosines compared to the theoretical sampling efficiency from (30) and Figure 17. Figure 18 shows the cumulative distribution 100,000 incoherent scattering angle cosines drawn by the estimator code for  $\alpha = 0.001, 0.01, 0.1, 1, 10$ , and 100 respectively with lines representing the cumulative probability density functions.

**Table 2. Comparison of Theoretical and Observed Rejection Sampling Efficiencies for 100,000 Angle Cosines Drawn by the Estimator Code for Various Values of Alpha for Incoherent Scattering.**

$\alpha$	$\eta$ - Theoretical	$\eta$ - Observed	$\alpha$	$\eta$ - Theoretical	$\eta$ - Observed
0.001	0.9980	0.9977	1	0.4307	0.4306
0.01	0.9805	0.9811	10	0.1228	0.1225
0.1	0.8413	0.8409	100	0.0215	0.0214

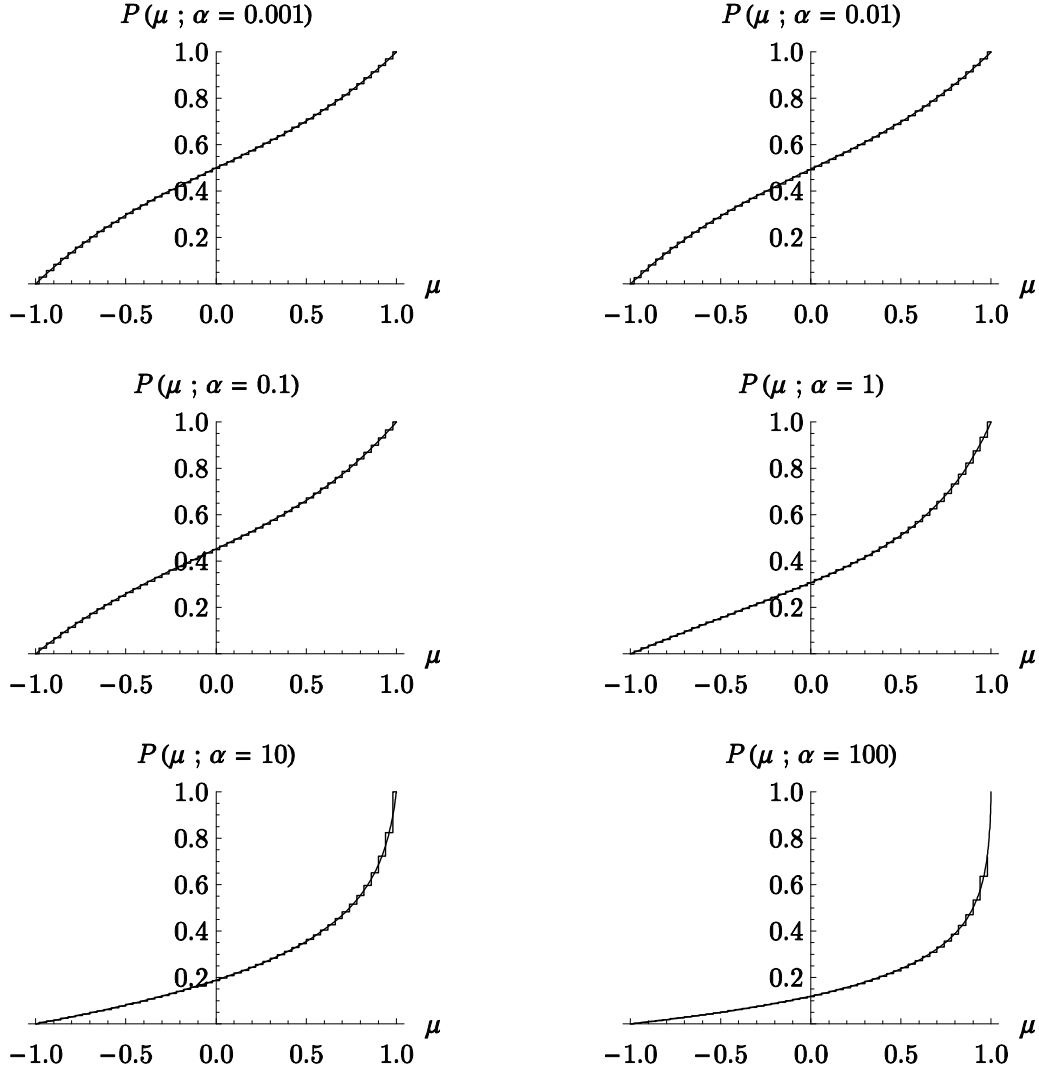


Figure 18. Distribution of 100,000 Angle Cosines Drawn by Estimator Code for Various Values of Alpha Compared to the Angle Cosine CDFs for Incoherent Scattering.

The  $\chi^2$  test was also applied to each set of angle cosines drawn by the code to test the goodness of fit to  $f(\mu; \alpha)$ . For each value of  $\alpha$  we accepted the null hypothesis. Table 3 shows the results of the  $\chi^2$  tests.

**Table 3. Results of Chi-Squared Test for Fit of 100,000 Incoherent Scatter Angle Cosines  
Drawn by the Code for Various Values of Alpha.**

$\alpha$	$\chi^2$	Critical Values (90% confidence, 49 DoF)		Accept Null Hypothesis?
		Upper	Lower	
0.001	42.47	66.34	33.93	Yes
0.01	52.08			Yes
0.1	41.27			Yes
1	46.39			Yes
10	39.90			Yes
100	60.23			Yes

### Isotropic Angles

Angle cosines for other photon interaction processes are drawn uniformly from negative one to one. This includes nuclear excited state gamma emission, emission of bremsstrahlung photons, and the *first* annihilation photon emitted after a pair production interaction. The *second* annihilation photon is constrained to travel in the opposite direction from the first. Thus, for the second photon

$$\mu_{h\nu_2} = -\mu_{h\nu_1} \quad (31)$$

and

$$\omega_{h\nu_2} = \omega_{h\nu_1} + \pi \quad . \quad (32)$$

This selects the direction of travel for the second photon as the direction of travel of the first photon reflected through the origin, aligning the two annihilation photons correctly for the pair production model.

### Angular Density

Recall the ray next-event estimator from (3)

$$P_{i,j} \left( A \middle| E', \Omega', s \right) = \frac{e^{-\tau(E', s_1)}}{2\pi} \int_{s_1}^{s_2} ds \frac{p(\theta(s)) \Sigma_{scat}(s) e^{-[\tau(E', s-s_1) + \tau(E(E', s), \rho(s))]} }{(\rho(s))^2} .$$

We recognize that for anisotropically scattered particles, the probability of scatter into a particular angle,  $p(\theta)$ , must be computed to evaluate the integral.

This probability, hereafter referred to as angular density, requires a different computational approach for each type of photon interaction.

### Coherent Scattering

To compute the angular density for a coherent scatter interaction, we need only evaluate the probability density function for the angular distribution of photons from coherent scattering for the known value of  $\mu$ . The coherent scatter PDF, (23), is

$$p(\mu) = \frac{3}{8} (1 + \mu^2).$$

Evaluating this function for the known value of  $\mu$  for scatter to the flux-point will give the angular density for coherent scatter for that particular value of  $\mu$ .

### Incoherent Scattering

Computing the angular density of an incoherent scatter contribution encounters the same challenges as drawing an angle cosine from the Klein-Nishina distribution. Recall the scaled version of the Klein-Nishina distribution, (18):

$$f(\mu; \alpha) = \left( \frac{1}{1 + \alpha(1 - \mu)} \right)^2 \left( \frac{1 + \mu^2}{2} \right) \left( 1 + \frac{\alpha^2 (1 - \mu)^2}{(1 + \mu^2)[1 + \alpha(1 - \mu)]} \right).$$

We can convert  $f(\mu; \alpha)$  to a PDF by

$$p(\mu; \alpha) = \frac{f(\mu; \alpha)}{\int_{-1}^1 f(\mu; \alpha) d\mu}. \quad (33)$$

However, the algebraic form of this function is complex and poorly conditioned for numerical implementation. Instead, we evaluate the numerator and denominator in the right hand side of (33) independently and then divide.

The numerator is easily evaluated for the known values of  $\alpha$  and  $\mu$ . The denominator, carrying out the integration, is

$$\int_{-1}^1 f(\mu; \alpha) d\mu = \frac{\alpha(\alpha + 8)(\alpha + 1) + 2}{\alpha^2(2\alpha + 1)^2} + \frac{\ln(2\alpha + 1)(\alpha(\alpha - 2) - 2)}{2\alpha^3} \quad (34)$$

This is easily evaluated for most values of  $\alpha$ , but becomes numerically unstable for small  $\alpha$ . Therefore, for  $\alpha$  greater than 0.01, we evaluate the right hand side of (34). For  $\alpha$  less than 0.01, we implement a numerical quadrature to evaluate the left hand side of (34). Once values are determined for the numerator and denominator on the right hand side of (33),  $p(\mu; \alpha)$  is found by carrying out the division. This gives the angular density for incoherent scatter for that particular value of  $\mu$ .

### Pair Production

The annihilation photons produced in pair production interactions also require an angular density adjustment, but for a different reason from the scattering interactions. The computed contribution to a time-energy bin at the flux-point is normally based on the likelihood of a scatter *to* the flux-point. In the case of pair production, the first annihilation photon is treated as an isotropically scattered photon and the contribution to the flux-point is computed. However, we must also consider the case in which the first annihilation photon travels *away* from the flux-point, aligning the second annihilation photon to contribute. Instead of a single angle at which the interaction can contribute to the flux-point, there are two. This reduces the solid angle over which the scatter is distributed from  $4\pi$  to  $2\pi$ . Assuming that the two photons produced in the

pair production interaction are identical except for their opposite directions of travel,  $p(\mu) = 1$ .

### **Post-Scatter Energy**

The estimator code must also compute the energy of a photon after a simulated interaction. For these computations, the energy of the incident photon is known, as well as the cosine of the departure angle from the interaction.

### **Incoherent Scattering**

Photon energy after an incoherent scatter interaction is computed by evaluating (11) for  $h\nu'$  using the energy of the incident photon,  $h\nu$ , and the cosine of the known scattering angle:

$$h\nu' = \frac{h\nu}{1 + \alpha(1 - \mu)} .$$

### **Constant Energy Processes**

For coherent scattering and pair production, the post scatter energy is not dependent on the scattering angle. The energy of a coherently scattered photon is identical to the energy of that photon before the scattering interaction (Choppin, Liljenzin, & Rydberg, 2002, p. 143). For pair production, the energy

for each of the annihilation photons is equal to the rest mass of an electron or 511 keV (Knoll, 2000, p. 52).

## Secondary Particles

Secondary or induced particles are particles created as a result of an interaction simulated by the estimator code.

### Bremsstrahlung Photons

Pair production, photoelectric absorption, and incoherent scattering interactions may produce high energy charged particles, electrons and positrons, which will decelerate in the scattering medium. The energy radiated by a decelerating charged particle, bremsstrahlung radiation, can be computed by combining (21) and (22) and assuming that all of the kinetic energy of the particle is dissipated to get

$$E_r = \frac{TZ(T + m_0c^2)}{Z(T + m_0c^2) + 1600m_0c^2} \quad (35)$$

where  $E_r$  is the energy radiated and  $T$  is the kinetic energy of the incident charged particle. If we assume that the energy radiated during deceleration of the charged particle is radiated as a single coherent photon, then (35) gives the energy of the bremsstrahlung photon.



The origin of the bremsstrahlung photon is assumed to be at the point of origin of the decelerating charged particle which is the location of the previous gamma interaction. This assumes that the range of the electron in the scattering medium is negligible compared to the ranges of the incident and departing photons. For example, an electron with 1 MeV of kinetic energy at an altitude of 51 km (where the air density of the US Standard Atmosphere is  $\approx 8.62 \times 10^{-7}$  g/cm<sup>3</sup>) and electron the range-energy relationship for air from NIST (2010), has a total path length on the order of 1 km. The projected range of the electron, or the range along the initial direction of travel, is significantly shorter due to the erratic nature of electron paths (Krane, 1988, p. 197). A 1 MeV gamma ray, at the same altitude, has an average mean free path on the order of 100 km. Thus we assume that the range of the electron is insignificant compared to that of the photon.

### **Decay of Excited Nuclei by Gamma Emission**

The emission of gamma ray photons as a result of gamma decay of excited nuclear states was also implemented in the estimator code. Gamma decay level lists were acquired from the Nudat 2.5 database (NNDC, 2010) and converted to a format to be read into the estimator code. Level lists were converted to a text file with five columns: level number, level energy, emitted gamma energy, emission intensity, and the number of the level to which the nucleus decays with

the emission of that gamma. There are as many lines in the file for each level as there are possible gamma emissions at that level. The formatted list for the first six levels of  $^{15}\text{N}$  is shown in Figure 19. Note the emission intensity values in the fourth column.

Level	Level E(kev)	Gamma E(kev)	Gamma I	New Level
1	5270.155	5269.161	100.0	0
2	5298.822	5297.817	100.0	0
3	6323.78	1024.92	0.05	2
3	6323.78	1053.58	0.1	1
3	6323.78	6322.35	100.0	0
4	7155.05	831.27	0.5	3
4	7155.05	1856.11	4.0	2
4	7155.05	1884.77	100.0	1
4	7155.05	7153.22	0.023	0
5	7300.83	977.02	0.25	3
5	7300.83	2001.86	0.2	2
5	7300.83	2030.53	0.6	1
5	7300.83	7298.92	100.0	0
6	7567.1	1243.2	0.6	3
6	7567.1	2268.1	4.0	2
6	7567.1	2296.8	100.0	1
6	7567.1	7565.0	1.3	0

Figure 19. Formatted List of Levels 1-6 for  $^{15}\text{N}$ .

Emission intensities for each emitted gamma at a level are given relative to the most likely emitted gamma at that level, which has emission intensity 100. The relative distribution of emission intensities for a level can easily be converted to a probability of emission by

$$p_{\gamma,i} = \frac{I_{\gamma,i}}{\sum_{j=1}^{n_{\gamma}} I_{\gamma,j}} \quad (36)$$

where  $p_{\gamma,i}$  is the probability of emitting the  $i$ th gamma in the list,  $I_{\gamma,i}$  is the emission intensity of the  $i$ th gamma in the list,  $n_{\gamma}$  is the number of gamma

emission possibilities for the level, and  $\sum_{j=1}^{n_\gamma} I_{\gamma,j}$  is the sum of all emission intensities in the list for that level.

### **Inelastic Neutron Scatter Gammas**

When a neutron inelastic scatter event is simulated by the estimator code, the material and inelastic level are known. We then use this information to simulate the emission of photons due to gamma decay of the excited state at the site of the inelastic scatter interaction.

Although gamma emissions by gamma decay have associated half-lives before emission, we assume that these half-lives are insignificant compared to the timescale of the simulation and any gamma emissions can be treated as occurring immediately. This assumption is appropriate because half-lives for gamma decay are generally on the order of femtoseconds, but would not be appropriate if any of the materials included in the simulation have *metastable states* with half-lives significant to the timescale of the simulation. We also assume that any motion of the excited nucleus in the course of the gamma decay is negligible, for reasons similar to ignoring the path length of charged particles, so the gamma emissions are simulated at the site of the inelastic scatter.

Using the known material, inelastic level, and the location and time of the inelastic scatter interaction, the estimator code draws from the listed gamma

emissions for that level according to their probabilities. The selected gamma emission is then stored for later transport computations. If the selected gamma emission decays to a lower excited level that also decays by gamma emission, an appropriate gamma emission is drawn and stored again. The process continues until a gamma emission is drawn that decays the nucleus to the ground state, level zero. Alternatively, to eliminate variance from sampling the gamma decay emission chain, all possible gamma emissions weighted according to their relative likelihood can be stored for later computation.

### **Neutron Absorption**

Following the absorption of a neutron by a target nucleus, that nucleus may be left in an excited state that decays by gamma emission. For simplicity, we exclude the radioactive decay of an unstable isotope created by neutron absorption, and include only the decay of a stable nucleus from higher energy states by gamma emission. For implementation in the estimator code, the energy level of the excited nucleus after absorbing a neutron is the energy level nearest to but not greater than the energy of the absorbed neutron minus the Q-value for the neutron absorption interaction. We assume that this residual energy is imparted to the atomic nucleus by placing it in an excited state. Recoil of the nucleus and other energy absorbing processes are not considered. The recoil energy of the nucleus in neutron absorption interactions is not negligible.

However, we ignore it here to simplify the physical model implemented in the code. This limits the physical relevance of the model, but implementation in the code provides the infrastructure for a more refined model to be implemented in the future. Once the energy level of the excited nucleus is determined, gamma decay can be modeled similarly to gamma decay for inelastic scattering interactions, but using the level list for the isotope of the absorber atom plus one neutron.

## Gamma Ray Source Energy Selection

Ray Next-Event Estimator v4.0 included several distributions for drawing energy of a particle at the source including monoenergetic, uniform, Maxwell, and Watt distributions. For the energy of gamma rays from fission, we add the following distribution.

A fit to the distribution of gamma ray energy from the fission of  $^{235}\text{U}$  is given by (Verbeke, Hagmann, & Wright, 2010, p. 12):

$$N(E) = \begin{cases} 38.13(E - 0.085)e^{1.648E} & 0.085 \leq E < 0.3 \\ 26.8e^{-2.3E} & 0.3 \leq E \leq 1.0 \\ 8.0e^{-1.1E} & 1.0 < E \leq 8.0 \end{cases} \quad (37)$$

where  $E$  is the energy of the gamma ray in MeV. This distribution can be converted to a probability density function (PDF) by

$$p(E) = \frac{N(E)}{\int_{0.085}^8 N(E) dE} . \quad (38)$$

The PDF is then

$$p(E) = \begin{cases} C_1 (E - 0.085) e^{1.648E} & 0.085 \leq E < 0.3 \\ C_2 e^{-2.3E} & 0.3 \leq E \leq 1.0 \\ C_3 e^{-1.1E} & 1.0 < E \leq 8.0 \end{cases} \quad (39)$$

where

$$\begin{aligned} C_1 &= 4.547769900940718 \\ C_2 &= 3.196439374382671 \\ C_3 &= 0.954161007278409 . \end{aligned}$$

The cumulative probability density function (CDF) is given by

$$P(E) = \int_{0.085}^E p(E') dE' \quad (40)$$

where  $E'$  is a dummy variable of integration. Selecting integration constants so

that  $P(E)$  remains continuous on  $0.085 \leq E \leq 8.0$  MeV, the CDF is

$$P(E) = \begin{cases} C_4 + (C_5 E - C_6) e^{1.648E} & 0.085 \leq E < 0.3 \\ C_7 - C_8 e^{-2.3E} & 0.3 \leq E \leq 1.0 \\ C_9 - C_{10} e^{-1.1E} & 1.0 < E \leq 8.0 \end{cases} \quad (41)$$

where

$$\begin{aligned}
C_4 &= 1.926282766794659 \\
C_5 &= 2.759569114648494 \\
C_6 &= 1.909059196740567 \\
C_7 &= 0.850727368388764 \\
C_8 &= 1.389756249731596 \\
C_9 &= 1.000130748747967 \\
C_{10} &= 0.867419097525827 .
\end{aligned}$$

Figure 20 shows plots of the PDF and CDF for the energy distribution of gamma rays from the fission of  $^{235}\text{U}$ .

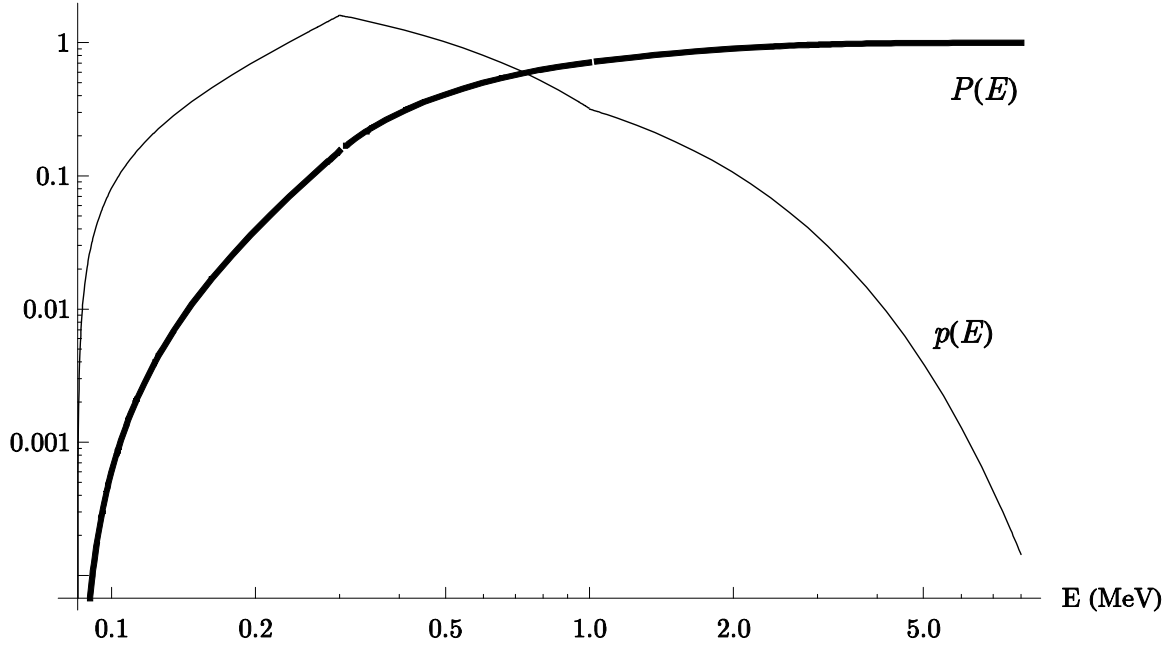


Figure 20. PDF and CDF for the Distribution of Gamma Ray Energies from Fission of  $^{235}\text{U}$ .

To sample  $E$ , we draw a random number,  $\xi$ , uniformly distributed between zero and one and evaluate  $P^{-1}(\xi)$  to find  $E$ . Because  $P(E)$  is a piecewise function, evaluation of  $P^{-1}(\xi)$  must be treated separately for each

interval. For  $0 \leq \xi < P(0.3)$ , or random numbers corresponding to the piece of the CDF where  $0.085 \leq E < 0.3$ ,  $P^{-1}(\xi)$  can be evaluated by root-solving. For  $P(0.3) \leq \xi \leq P(1.0)$  and  $P(1.0) < \xi \leq 1$ , or random numbers corresponding to the second and third pieces of the CDF,  $P^{-1}(\xi)$  can be evaluated directly by

$$E = P^{-1}(\xi) = \begin{cases} C_{11} \ln \left[ C_{12} (C_{13} - \xi) \right] & P(0.3) \leq \xi \leq P(1.0) \\ C_{14} \ln \left[ C_{15} (C_{16} - \xi) \right] & P(1.0) < \xi \leq 1 \end{cases} \quad (42)$$

where

$$\begin{aligned} C_{11} &= -0.434782608695652 \\ C_{12} &= 0.719550640763897 \\ C_{13} &= 0.850727368388764 \\ C_{14} &= -0.909090909090909 \\ C_{15} &= 1.152845265745635 \\ C_{16} &= 1.000130748747967 . \end{aligned}$$

Figure 21 shows the cumulative distribution of 100,000 energies drawn by the estimator code from the distribution in (39).

The 100,000 gamma ray energies drawn by the code were sorted into 50 equally spaced bins, the  $\chi^2$  test was applied, and we accepted the null hypothesis. The results of the  $\chi^2$  test are shown in Table 4.



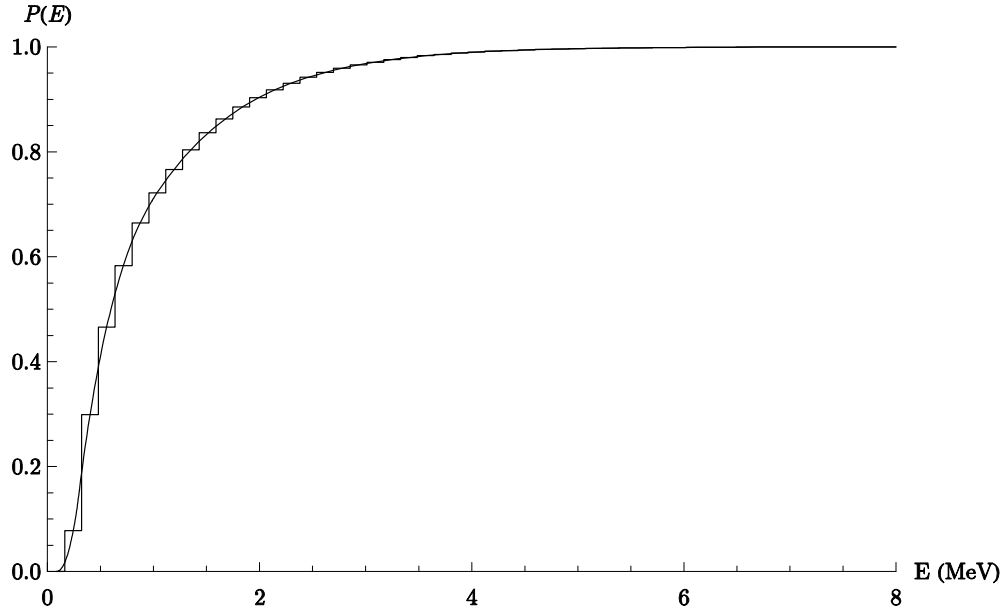


Figure 21. Cumulative Distribution of 100,000 Gamma Ray Energies Drawn by the Estimator Code for Fission of  $^{235}\text{U}$  Compared to the Gamma Energy CDF.

Table 4. Results of Chi-Squared Test for Fit of 100,000 Gamma Ray Energies Drawn by the Estimator Code for Fission of  $^{235}\text{U}$ .

$\chi^2$	Critical Values (90% confidence, 49 DoF)		Accept Null Hypothesis?
	Upper	Lower	
42.72	66.34	33.93	Yes

## Summary of Major Changes to RNEE 4.0

### Source Code Reorganization

Because RNEE v4.0 was developed with the goal of demonstrating the ray next-event estimation method for neutron transport, significant organizational changes were necessary throughout the majority of the source code to allow

integration of transport calculations for a second type of particle. These organizational changes grouped the source code into modules by function conducive to the addition of gamma ray transport computations. The reorganization also served to create an open program architecture to allow for future modifications and additions to the code.

### **Variable Dimensional Extension**

Ray Next-Event Estimator v4.0 used several large multidimensional arrays to store results of the transport computations. These allocatable arrays store the computed particle flux and tally count for each time-energy bin at the flux-point for each batch of particle histories. To utilize the existing data structure as much as possible, these variables were extended by one dimension. Results for neutron transport computations were stored in the first position of the new dimension and results for gamma transport computations were stored in the second position of the new dimension.

However, simply adding an additional dimension index would have constrained the results arrays to identical dimensions in time and energy. Energy range, energy resolution, time resolution, and time of interest for the time-energy grid at the flux-point may be different for each particle type included in the computation. These differences result in different time-energy grid dimensions for each particle type in the computation. To add the new variable dimension

and preserve the flexibility of different results array dimensions, a Fortran derived type was created to mirror the multidimensional allocatable array in the original code. A new variable was then created as a two-element array of the new type. This resulting two-element array contained two independently-allocatable multidimensional arrays to store transport computation results for the two different particle types.

## **Photon Interaction Physics Data**

### **Photo-Atomic Cross Sections**

Cross sections for photo-atomic interactions were acquired from the XCOM Photon Cross Sections Database (NIST, 2010). Interactions included are coherent scattering, incoherent scattering, photoelectric absorption, and pair production with energy ranging from 1 keV to 100 GeV. The cross sections can be interpolated using logarithmic functions. The cross sections are queried from the online database and downloadable in several formats, including the text format used by RNEE v5.1. A sample is shown in Figure 22.

Photon Energy	Coherent Scatter.	Incoher. Scatter.	Photoel. Absorb.	Nuclear Pr. Prd.	Electron Pr. Prd.	Tot. w/ Coherent	Tot. wo/ Coherent
1.000E-03	1.29E+00	1.10E-02	3.31E+03	0.00E+00	0.00E+00	3.31E+03	3.31E+03
1.500E-03	1.18E+00	2.23E-02	1.08E+03	0.00E+00	0.00E+00	1.08E+03	1.08E+03
2.000E-03	1.05E+00	3.51E-02	4.76E+02	0.00E+00	0.00E+00	4.77E+02	4.76E+02
3.000E-03	8.00E-01	5.98E-02	1.45E+02	0.00E+00	0.00E+00	1.46E+02	1.45E+02
4.000E-03	6.11E-01	8.02E-02	6.10E+01	0.00E+00	0.00E+00	6.17E+01	6.10E+01
5.000E-03	4.77E-01	9.57E-02	3.09E+01	0.00E+00	0.00E+00	3.14E+01	3.10E+01
6.000E-03	3.84E-01	1.07E-01	1.76E+01	0.00E+00	0.00E+00	1.81E+01	1.77E+01
8.000E-03	2.69E-01	1.23E-01	7.17E+00	0.00E+00	0.00E+00	7.56E+00	7.29E+00
1.000E-02	2.03E-01	1.33E-01	3.54E+00	0.00E+00	0.00E+00	3.88E+00	3.68E+00
1.500E-02	1.21E-01	1.48E-01	9.67E-01	0.00E+00	0.00E+00	1.24E+00	1.12E+00
2.000E-02	8.04E-02	1.57E-01	3.81E-01	0.00E+00	0.00E+00	6.18E-01	5.37E-01
3.000E-02	4.23E-02	1.63E-01	1.01E-01	0.00E+00	0.00E+00	3.07E-01	2.64E-01
4.000E-02	2.58E-02	1.64E-01	3.91E-02	0.00E+00	0.00E+00	2.29E-01	2.03E-01
5.000E-02	1.74E-02	1.62E-01	1.87E-02	0.00E+00	0.00E+00	1.98E-01	1.81E-01
6.000E-02	1.25E-02	1.59E-01	1.02E-02	0.00E+00	0.00E+00	1.82E-01	1.69E-01
8.000E-02	7.30E-03	1.53E-01	3.92E-03	0.00E+00	0.00E+00	1.64E-01	1.57E-01
1.000E-01	4.77E-03	1.46E-01	1.87E-03	0.00E+00	0.00E+00	1.53E-01	1.48E-01

Figure 22. Sample of Output from XCOM Photon Cross Sections Database

### Level Lists for Gamma Decay

Lists of levels for gamma decay are available from the Nudat 2.5 database (NNDC, 2010). The data is available for each isotope in tabular html format or as a complete evaluated nuclear structure data file (ENSDF). Because only a few materials were used in the course of this research, the tabular form of the data was converted to the level lists used to implement production of secondary gamma rays from gamma decay. If the estimator code is modified for application to a problem with many atmospheric constituents or requiring level data for many isotopes, it may be advantageous to modify the code to read directly from an ENSDF file.

## Particle Stacking in Linked Lists

Ray Next-Event Estimator v4.0 only considered neutron interactions with a single particle on the exit channel. Several of the newly added gamma interactions, as well as the inclusion of gamma emission cascades from neutron interactions, have the potential to produce multiple photons in a single interaction. To accommodate these groups of simultaneously generated particles, a set of variables was added to the code to serve as storage for particles awaiting transport calculations. As a particle is produced, either at the source or in a following interaction, it is placed in a set of storage locations called the particle stack. The estimator code then retrieves a particle from the stack and proceeds to make the transport calculations for that particle. In the course of the transport calculations, more particles produced in interactions of the current particle may be placed on the particle stack. After completing the transport calculations for a particle, the estimator code then checks for another particle on the stack and continues the transport calculation. If no particles remain on the stack, the computation is complete.

Memory allocation for storage of particle stacks poses an interesting challenge for implementation: How much stack space is required? The conditions of the problem being solved and the parameters given to the estimator code can cause the required amount of storage to vary wildly. To avoid quantifying the required amount of storage and limiting the flexibility of the

estimator code, a linked list was implemented. A linked list is a dynamic data structure in which each element in the list contains pointers to memory locations of the previous and following elements in the list (Chapman, 2008, pp. 714-720).

Linked list implementations have two main challenges:

1. The process of incrementally allocating memory for each variable on the stack is significantly slower than the single large array stack implementation.
2. The memory use of the stack is unbounded and could become too large during a program run.

To minimize the additional time required for incremental memory allocations, the management of the linked list was modified so that when a particle was read from the list, its memory was not deallocated. Instead, another pointer variable was used to track the location of the next particle to be read from the stack. This allowed the memory allocated for the stack to grow and never shrink. When a new particle was generated to be placed on the stack, it is now stored in a memory location that is already allocated and the pointer to the next particle to be read from the stack is updated. Only when the full extent of the allocated stack memory is occupied by particles awaiting transport computations will a new particle have new memory allocated for it. This minimizes the time spent allocating memory for the particle stack for each code run.

To control the amount of memory used by a particle stack, counters were implemented to track the number of elements currently in the list and the total number of elements allocated for the list. These integers could then be interrogated to determine the extent of the particle stack memory use and to force memory management or graceful program shutdown should the memory allocation for the list become excessive.

### **Batch and Particle Sequencing**

To accommodate the coupled neutron-photon transport problem and to allow for future application to the coupled photon-neutron problem, neutron and photon transport computations were implemented in a phased manner. At the start of a run, the estimator code initializes time-energy grids for both the neutron and photon particle types. The estimator code then runs the neutron transport problem, if one is specified. During the course of the computation, if a coupled neutron-photon problem is specified, any photons induced in neutron interactions are also transported and their contributions to the gamma ray time-energy grid are computed. Once computations are complete for the neutron transport problem and its associated gamma ray transport, the results are processed and written to file.

At this point, if no additional computations are specified, the program run is complete. However, if a gamma ray transport problem is specified, the

estimator code reinitializes the time-energy grids and other computation variables and then performs the gamma ray transport computation in a similar fashion to the neutron transport computation that preceded it. In this manner, the estimator code may be applied to coupled neutron-photon or photon-neutron transport computations.



## IV. Estimator Results and Demonstration

The Ray Next-Event Estimator (RNEE) v5.1 code was demonstrated for neutron transport computations and compared to results from identical problem runs computed by RNEE v4.0. Both code versions were demonstrated for transport of neutrons from a 14.06 MeV monoenergetic neutron source and a  $^{235}\text{U}$  fission Watt distributed neutron source. After determining that the version 5.1 was functioning consistently with version 4.0, RNEE v5.1 was demonstrated for gamma ray transport from a 15 MeV monoenergetic gamma ray source and a  $^{235}\text{U}$  fission distributed gamma ray source. Further demonstration was made for coupled neutron-photon computations for a  $^{235}\text{U}$  fission Watt distributed neutron source and a 14.06 MeV monoenergetic neutron source. Table 5 lists the properties and purpose for each simulation that will be described in this section.

The ray next-event estimator code produces *large* amounts of results data including time-energy grid flux estimates, time-energy grid contribution tally counts, statistical comparisons between particle batches, and time-energy grid flux from direct flight contributions. It is the hope of the author that the limited data presented here is sufficient to illustrate the functionality and utility of the estimator method and code.

Table 5. List of Simulations Used to Exercise the Estimator Code.

Run	Code Version	Description	Purpose	Total Histories	Batches
1a	4.0	Neutron Transport:	v5.1 function check	$2 \times 10^6$	40
1b	5.1	Monoenergetic Source		$2 \times 10^6$	40
2a	4.0	Neutron Transport:		$2 \times 10^6$	40
2b	5.1	Fission Source		$2 \times 10^6$	40
3	5.1	Photon Transport: Monoenergetic Source	Photon Transport Demo	$1 \times 10^6$	20
4	5.1	Photon Transport: Fission Source		$1 \times 10^6$	20
5	5.1	Coupled Transport: Fission Neutron Source	Coupled Neutron- Photon Transport Demo	$1 \times 10^6$	10
6	5.1	Coupled Transport: Monoenergetic Neutron Source		$1 \times 10^6$	10

### RNEE v5.1 Function Check

The organizational and computational changes to the estimator code were verified by two test simulations: Neutron transport from a monoenergetic source, and neutron transport from a Watt distributed fission source. Each simulation was run on version 4.0 and version 5.1 of the estimator code. The objective was to observe near identical computational results from both versions of the code.

## Run #1 - Neutron Transport, Monoenergetic Source

The first test problem was the transport of neutrons from a 14.06 MeV monoenergetic neutron point source at 50 km altitude to a flux-point at 35,810 km altitude. The purpose of this simulation was to compare the results computed by version 5.1 of the estimator code to result of an identical neutron transport problem run from version 4.0. Properties of the neutron source and flux-point time-energy grid are listed in Table 6. Examples of input files to both versions of the estimator can be found in Appendix B.

**Table 6. Properties of the Source and Flux-Point Time-Energy Grid for Monoenergetic Neutron Source Neutron Transport Demonstration.**

<u>Source</u>		<u>Neutron Flux-Point Time-Energy Grid</u>	
<b>Type</b>	Neutron, Monoenergetic	<b>Energy Range</b>	0.01 – 15 MeV
<b>Energy</b>	14.06 MeV	<b>Energy Resolution</b>	0.01 MeV
<b># of Histories</b>	$2 \times 10^6$ in 40 batches	<b>Time of Interest</b>	20 sec
<b>Altitude</b>	50 km	<b>Time Resolution</b>	0.01 sec
		<b>Flux-Point Altitude</b>	35,810 km

The scattered free-field flux at the flux-point per source neutron

$\left( n_{\text{flux-point}} \cdot \text{cm} \cdot \text{cm}^{-3} \cdot \text{s}^{-1} \cdot n_{\text{source}}^{-1} \right)$  for each time-energy bin is plotted for versions 4.0 and 5.1 of the estimator code in Figure 23 and Figure 24 respectively.

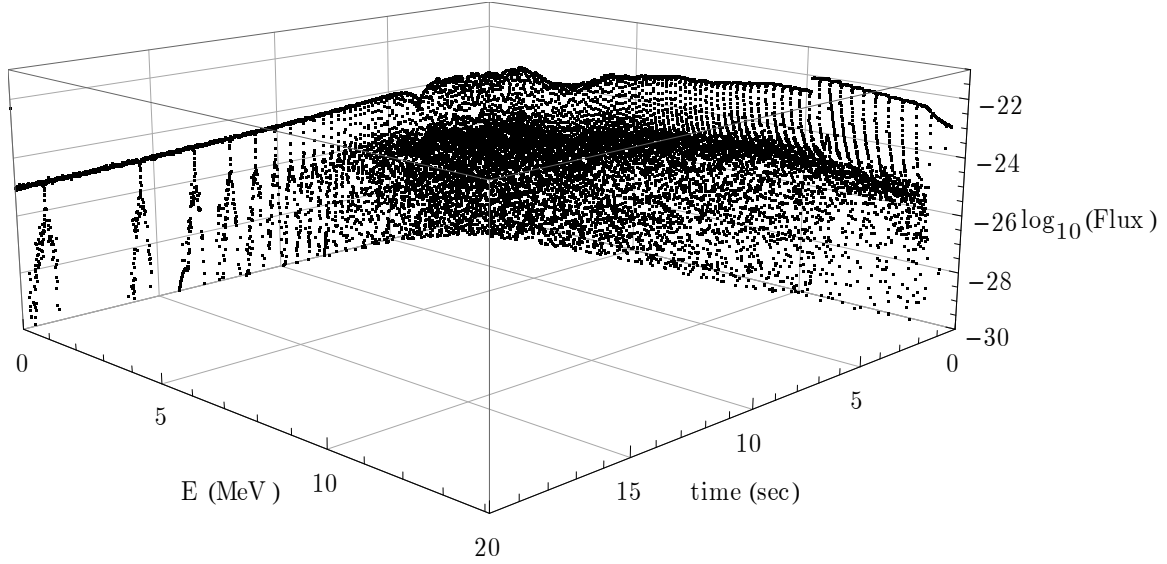


**Figure 23. Ray-Estimated Neutron Flux Per Source Neutron at the Flux-Point from a Monoenergetic Point Source in Time and Energy Computed by RNEE v4.0.**

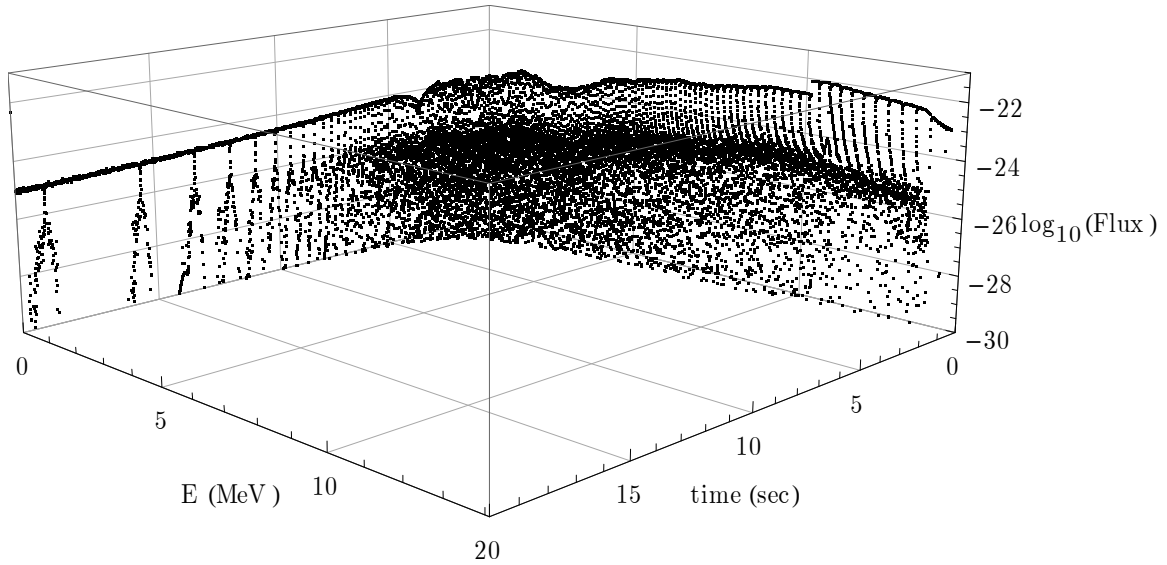


**Figure 24. Ray-Estimated Neutron Flux Per Source Neutron at the Flux-Point from a Monoenergetic Point Source in Time and Energy Computed by RNEE v5.1.**

By graphical inspection and numerical comparison, versions 4.0 and 5.1 of the estimator code were in agreement with a mean relative difference of 0.66%. Perfect agreement was not expected because changes to the code structure

changed the order in which random numbers were drawn from the random number stream.

The ray-estimated and point-estimated time integrated flux spectra computed by code version 5.1 are plotted Figure 25 for neutron energies up to 2 MeV to better illustrate the behavior of neutron contributions to the flux in an energy range where the cross section varies significantly with energy. Note the energy correlated peaks in cross section and valleys in neutron flux at the flux-point.

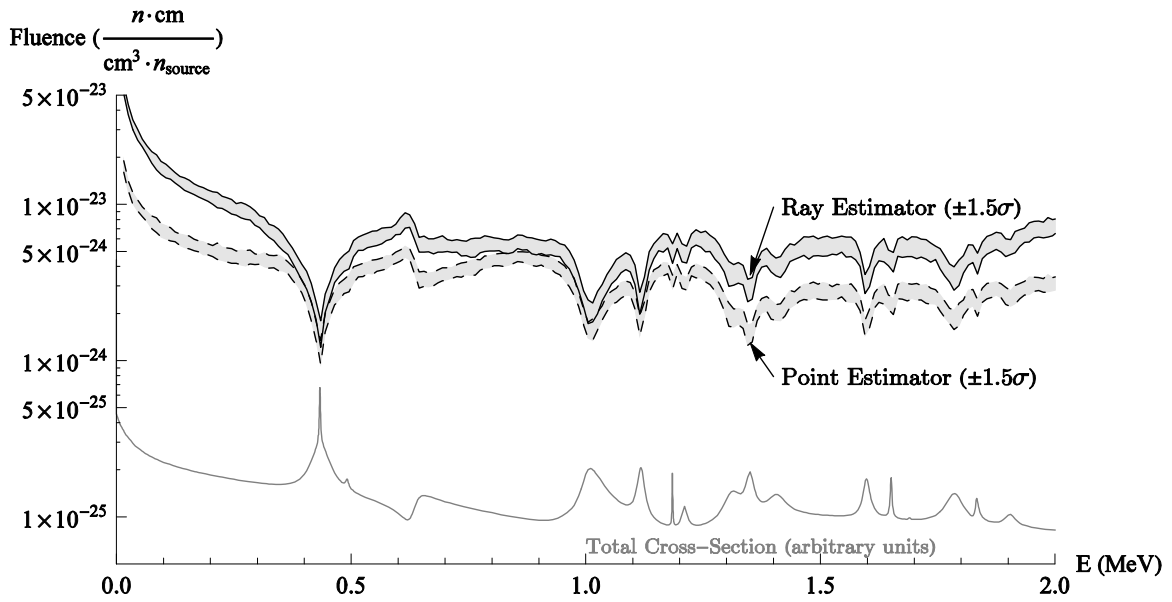


Figure 25. Ray- and Point- Estimated Time Integrated Flux Spectra for Neutron Transport from a Monoenergetic Point Source, 0 to 2 MeV.

## Run #2 - Neutron Transport, Fission Source

The next test problem was the same as run #1 except the neutrons were emitted from a Watt distributed  $^{235}\text{U}$  fission neutron point source. The purpose of this simulation was again to compare the results computed by version 5.1 of the estimator code to result of an identical neutron transport problem run from version 4.0. Properties of the neutron source and flux-point time-energy grid are listed in Table 7.

**Table 7. Properties of the Source and Flux-Point Time-Energy Grid for Fission Neutron Source Neutron Transport Demonstration.**

<u>Source</u>		<u>Neutron Flux-Point Time-Energy Grid</u>	
<b>Type</b>	Neutron, $^{235}\text{U}$ Fission	<b>Energy Range</b>	0.01 – 15 MeV
	Watt Distribution	<b>Energy Resolution</b>	0.01 MeV
<b># of Histories</b>	$2 \times 10^6$ in 40 batches	<b>Time of Interest</b>	20 sec
<b>Altitude</b>	50 km	<b>Time Resolution</b>	0.01 sec
		<b>Flux-Point Altitude</b>	35,810 km

The Watt distributed  $^{235}\text{U}$  fission distribution for the neutron source was built in to version 4.0 of the estimator code. The Watt distribution for  $^{235}\text{U}$  fission is:

$$\chi(E) = 0.453e^{-1.036E} \sinh\left(\sqrt{2.29E}\right) \quad (43)$$

where  $E$  is neutron energy in MeV (Knief, 2008, p. 45). The Watt distribution is plotted in Figure 26.

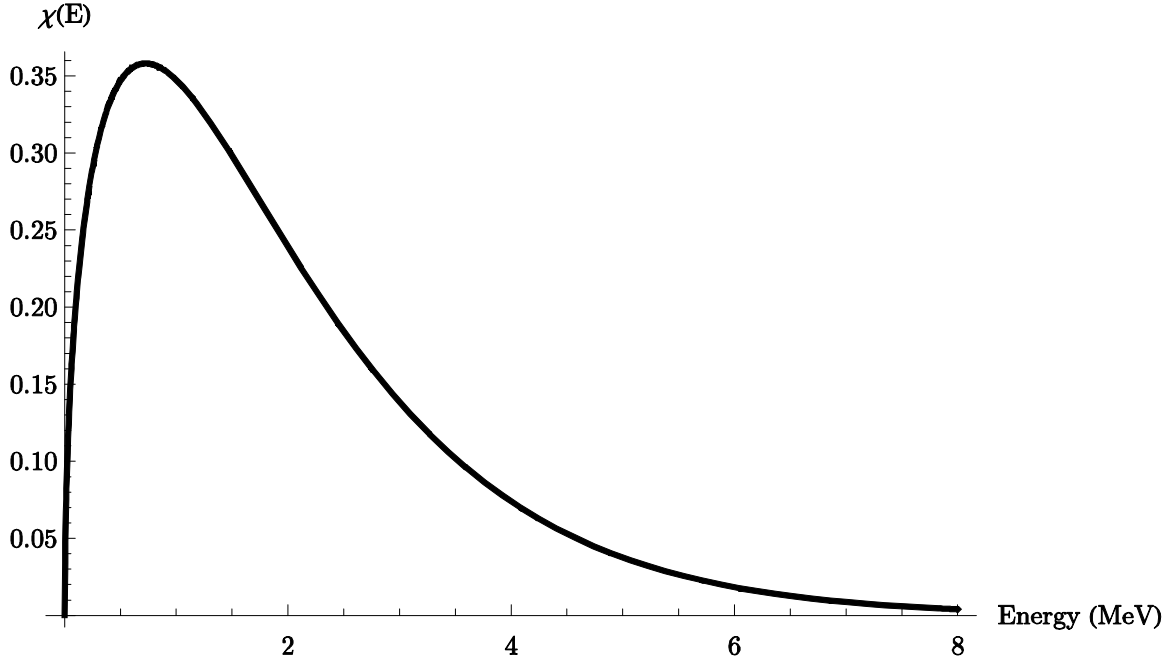
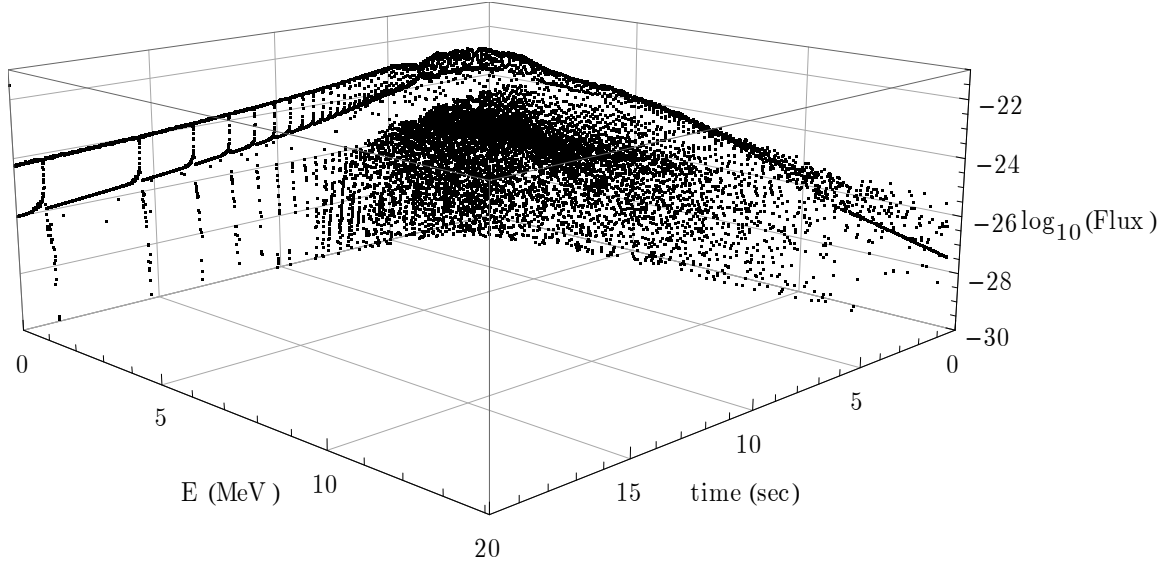


Figure 26. Watt Distribution of Neutron Energies from Fission of  $^{235}\text{U}$ .

The scattered free-field flux at the flux-point per source neutron  $\left( n_{\text{flux-point}} \cdot \text{cm} \cdot \text{cm}^{-3} \cdot \text{s}^{-1} \cdot n_{\text{source}}^{-1} \right)$  for each time-energy bin is plotted for versions 4.0 and 5.1 of the estimator code in Figure 27 and Figure 28 respectively.

By graphical inspection and numerical comparison, versions 4.0 and 5.1 of the estimator code were in agreement with a mean relative difference of 0.68%. Perfect agreement was not expected because changes to the code structure changed the order in which random numbers were drawn from the random number stream.



**Figure 27. Ray-Estimated Neutron Flux Per Source Neutron at the Flux-Point from a  $^{235}\text{U}$  Watt Distributed Point Source in Time and Energy Computed by RNEE v4.0.**

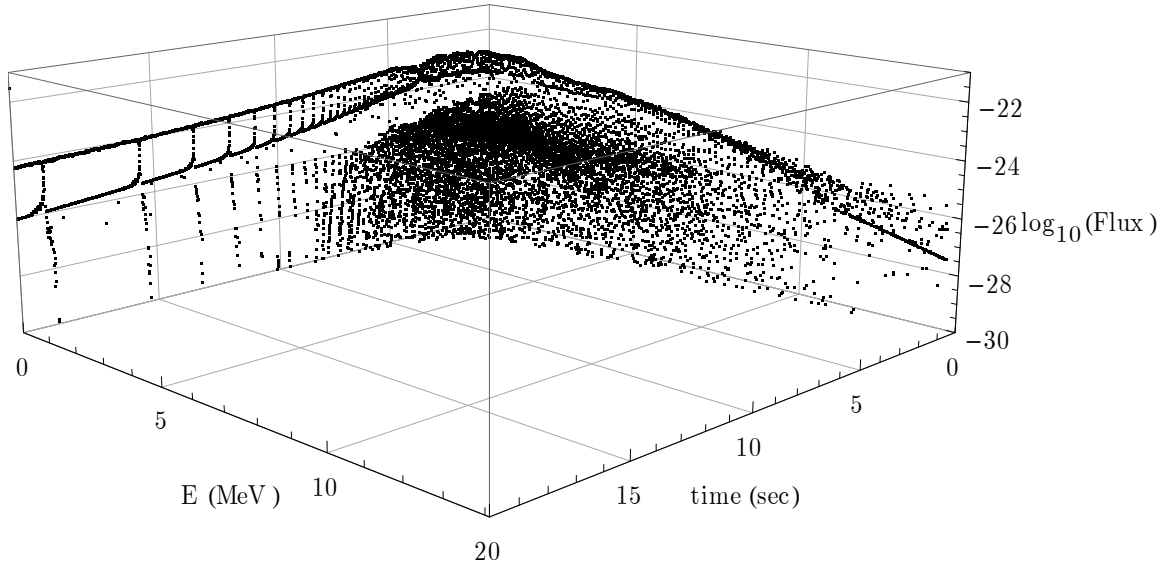


**Figure 28. Ray-Estimated Neutron Flux Per Source Neutron at the Flux-Point from a  $^{235}\text{U}$  Watt Distributed Point Source in Time and Energy Computed by RNEE v5.1.**

Based on comparison of estimator results from runs 1 and 2, and many other simulations run in the course of this research and throughout the code



modification process, the changes between estimator code versions 4.0 and 5.1 did not impact the computational results of the code for neutron transport.

## **RNEE v5.1 Demonstration: Gamma Ray Transport**

Many simulations were run to demonstrate the newly implemented gamma ray transport computation capability. Gamma ray transport from a monoenergetic source and gamma ray transport from a fission source are discussed here.

### **Run #3 - Gamma Ray Transport, Monoenergetic Source**

The first gamma ray test problem was the transport of gamma rays from a 15 MeV monoenergetic gamma ray point source at 50 km altitude to a flux-point at 35,810 km altitude. The purpose of this simulation was to demonstrate the application of RNEE v5.1 to the transport of primary gamma rays from a monoenergetic point source. Properties of the gamma ray source and flux-point time-energy grid are listed in Table 8.

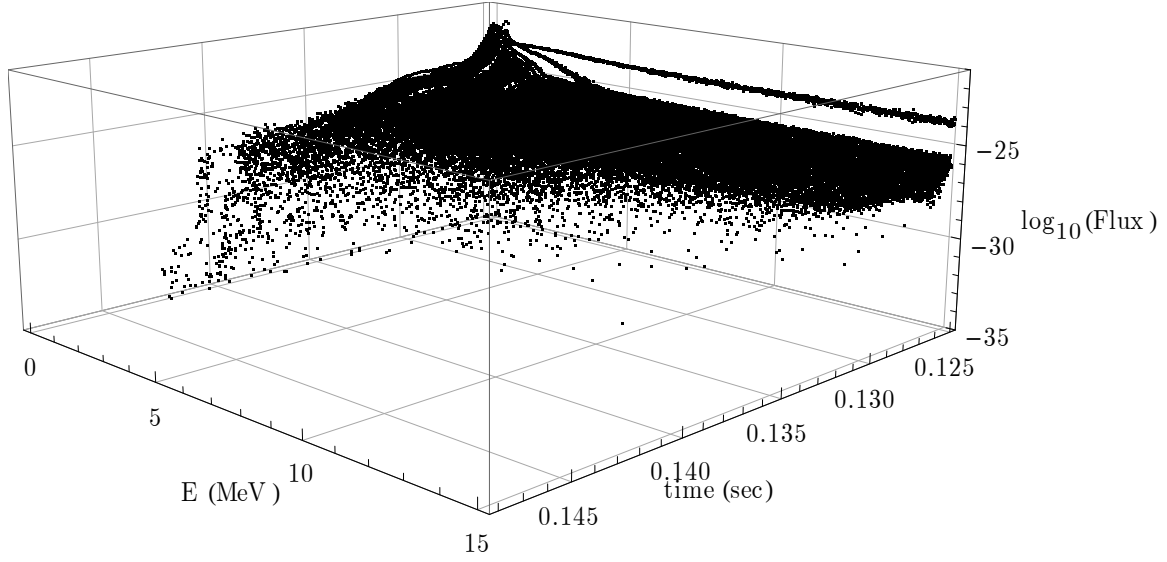
The scattered free-field flux at the flux-point per source gamma ray  $\left( \gamma_{\text{flux-point}} \cdot \text{cm} \cdot \text{cm}^{-3} \cdot \text{s}^{-1} \cdot \gamma_{\text{source}}^{-1} \right)$  for each time-energy bin is plotted for the point estimator and the ray estimator in Figure 29 and Figure 30 respectively. The inverse relative standard deviation,  $1 / \sigma_{rel}$ , for each time-energy bin is plotted in

Figure 31 to compare the relative certainty of the flux estimate from the point and ray estimators (larger values indicate higher certainty).

**Table 8. Properties of the Source and Flux-Point Time-Energy Grid for Monoenergetic Gamma Ray Source Gamma Ray Transport Demonstration.**

<u>Source</u>		<u>Gamma Flux-Point Time-Energy Grid</u>	
<b>Type</b>	Photon, Monoenergetic	<b>Energy Range</b>	0.01 – 15 MeV
<b>Energy</b>	15 MeV	<b>Energy Resolution</b>	0.01 MeV
<b># of Histories</b>	$1 \times 10^6$ in 20 batches	<b>Time of Interest</b>	0.2 sec
<b>Altitude</b>	50 km	<b>Time Resolution</b>	0.00001 sec
		<b>Flux-Point Altitude</b>	35,810 km

The energy peak at  $m_0c^2$  expected from annihilation of positrons produced in pair production interactions was not observed in the ray-estimated flux. One possible explanation for the lack of this expected feature is that the numerical quadrature implemented to evaluate the ray next-event estimator integrand may not appropriately evaluate the endpoints of each segment of the ray. These endpoints are explicitly evaluated in the point estimator by definition, giving the point estimate the distinct energy peak at  $m_0c^2$ .



**Figure 29. Point-Estimated Gamma Ray Flux Per Source Gamma Ray at the Flux-Point from a Monoenergetic Point Source in Time and Energy.**

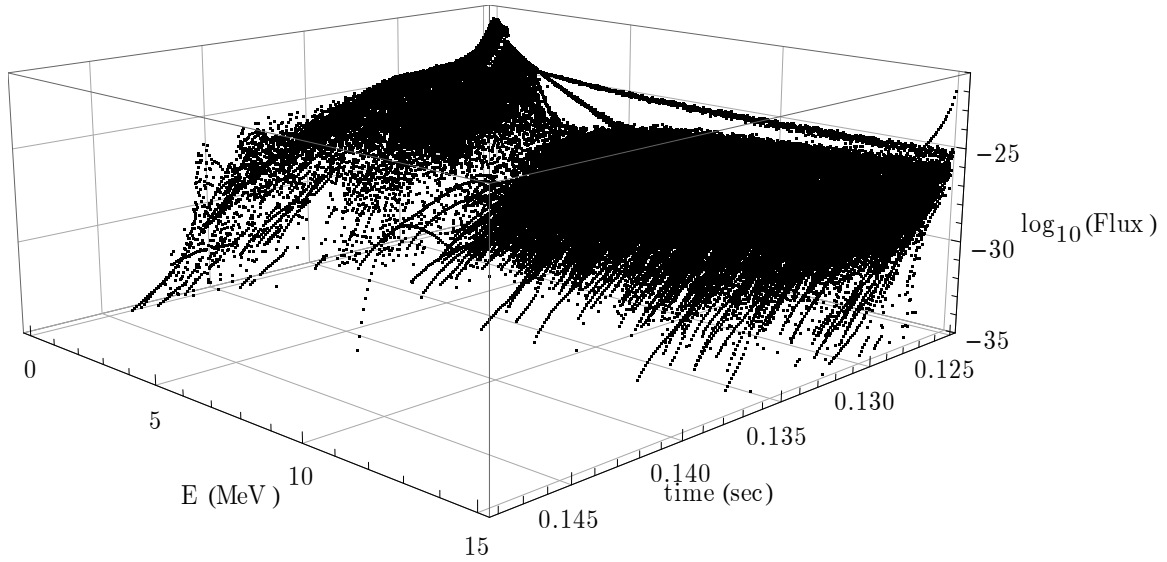


**Figure 30. Ray-Estimated Gamma Ray Flux Per Source Gamma Ray at the Flux-Point from a Monoenergetic Point Source in Time and Energy.**

The ray estimate also showed a large *saddle* in the energy range 1 to 5 MeV where a lower flux at the flux-point was estimated than in the point estimate. The variance in the ray-estimated flux was also much higher than in the

point-estimated flux in this region of the spectra. The appearance of this saddle may be an artifact of the angular density implementation or weighting of the likelihood of each mechanism as the estimate is computed for the ray. Because the appearance of the saddle feature is limited to the ray estimate, it is possible that a coding implementation for one or more photon interaction computations was adequate for the point estimator, but not the ray estimator.

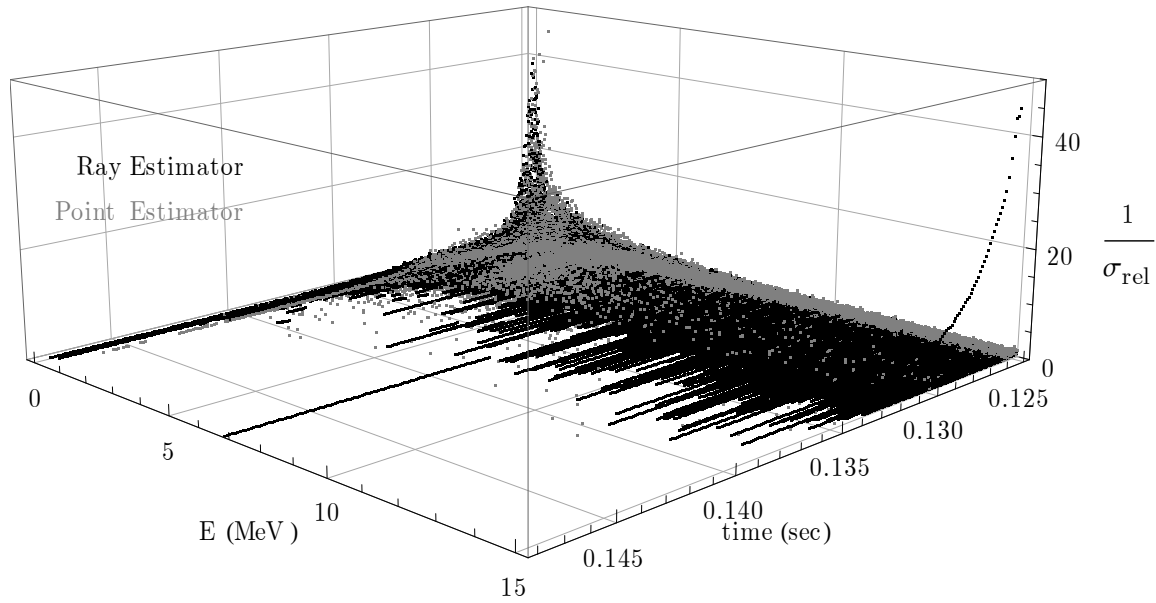


**Figure 31. Inverse Relative Standard Deviation of Point- and Ray- Estimated Gamma Ray Flux at the Flux-Point from a Monoenergetic Point Source in Time and Energy.**

We expected to observe lower variance in the estimate computed by the ray estimator. However, initial investigation indicated that the variance of the point estimate was generally lower along the *ridge* of peak flux and in other areas of the grid where the number of histories contributing to a particular time-energy bin was high. The ray estimator provided estimates with lower variance in

time-energy bins to the left and right of the peak flux ridge in time where the number of contributing histories was lower. The ray estimator had lower variance at the high energy end of the spectrum and both the point and ray estimators appeared to have comparable variance at energies below 1 MeV.

It was also illustrative to compare the features of point and ray estimates as fluence (flux integrated over the time of the simulation). The ray-estimated and point-estimated time integrated flux spectra are plotted in Figure 32. The energy peak at  $m_0 c^2$  is clearly visible in the point estimate and missing from the ray estimate. The low energy end of the flux saddle is also visible in the ray estimate.

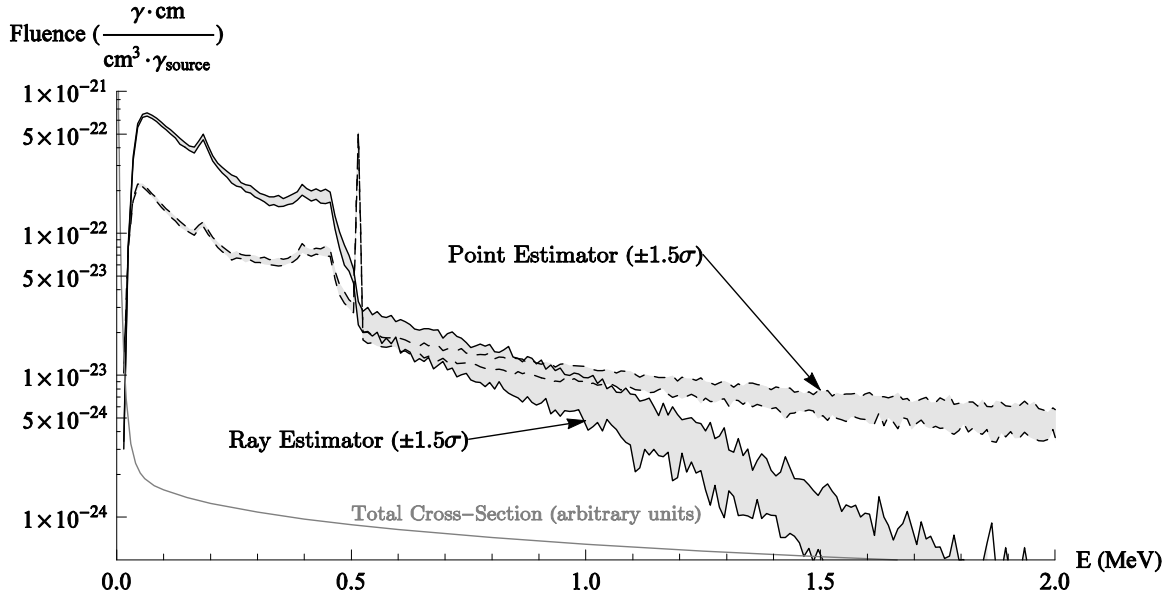


Figure 32. Ray- and Point- Estimated Time Integrated Flux Spectra for Gamma Ray Transport from a Monoenergetic Point Source.

## Run #4 - Gamma Ray Transport, Fission Source

The next test problem was the same as run #3 except the gamma rays were emitted from a  $^{235}\text{U}$  fission gamma ray point source. The purpose of this simulation was to demonstrate the application of RNEE v5.1 to the transport of primary gamma rays from a fission distributed point source. Properties of the gamma ray source and flux-point time-energy grid are listed in Table 9.

The scattered free-field flux at the flux-point per source gamma ray  $\left( \gamma_{\text{flux-point}} \cdot \text{cm} \cdot \text{cm}^{-3} \cdot \text{s}^{-1} \cdot \gamma_{\text{source}}^{-1} \right)$  for each time-energy bin is plotted for the point estimator and the ray estimator in Figure 33 and Figure 34 respectively. The inverse relative standard deviation,  $1 / \sigma_{\text{rel}}$ , for each time-energy bin is plotted in Figure 35 to compare the relative certainty of the flux estimate from the point and ray estimators (larger values indicate higher certainty).

**Table 9. Properties of the Source and Flux-Point Time-Energy Grid for  $^{235}\text{U}$  Fission Gamma Ray Source Gamma Ray Transport Demonstration.**

<u>Source</u>		<u>Gamma Flux-Point Time-Energy Grid</u>	
<b>Type</b>	Photon, $^{235}\text{U}$ Fission	<b>Energy Range</b>	0.01 – 8 MeV
		<b>Energy Resolution</b>	0.01 MeV
<b># of Histories</b>	$1 \times 10^6$ in 20 batches	<b>Time of Interest</b>	0.2 sec
<b>Altitude</b>	50 km	<b>Time Resolution</b>	0.00001 sec
		<b>Flux-Point Altitude</b>	35,810 km

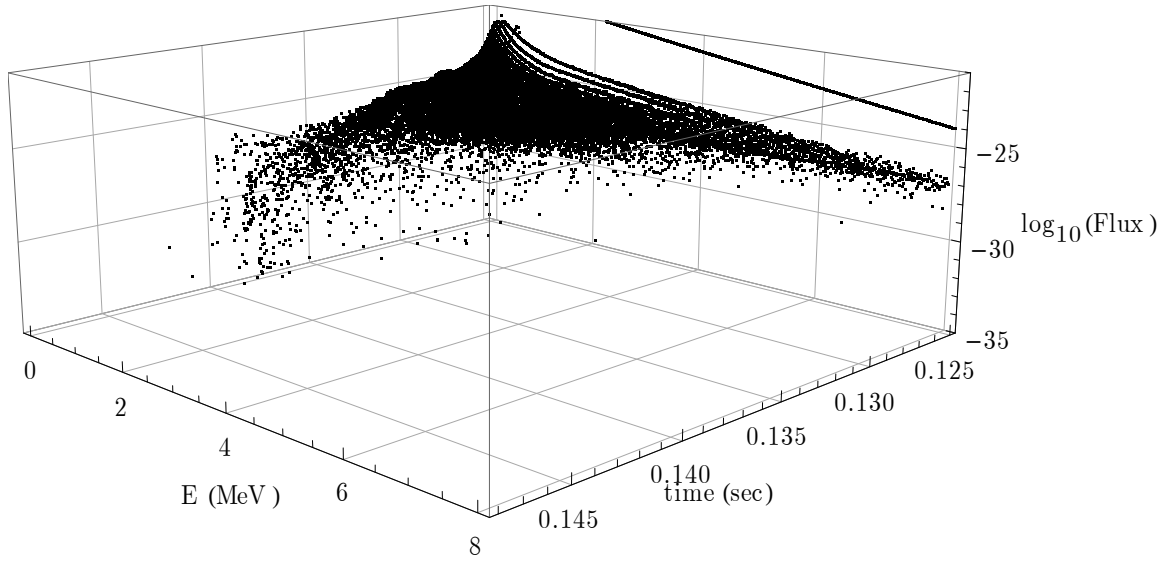


**Figure 33. Point-Estimated Gamma Ray Flux Per Source Gamma Ray at the Flux-Point from a  $^{235}\text{U}$  Fission Point Source in Time and Energy.**

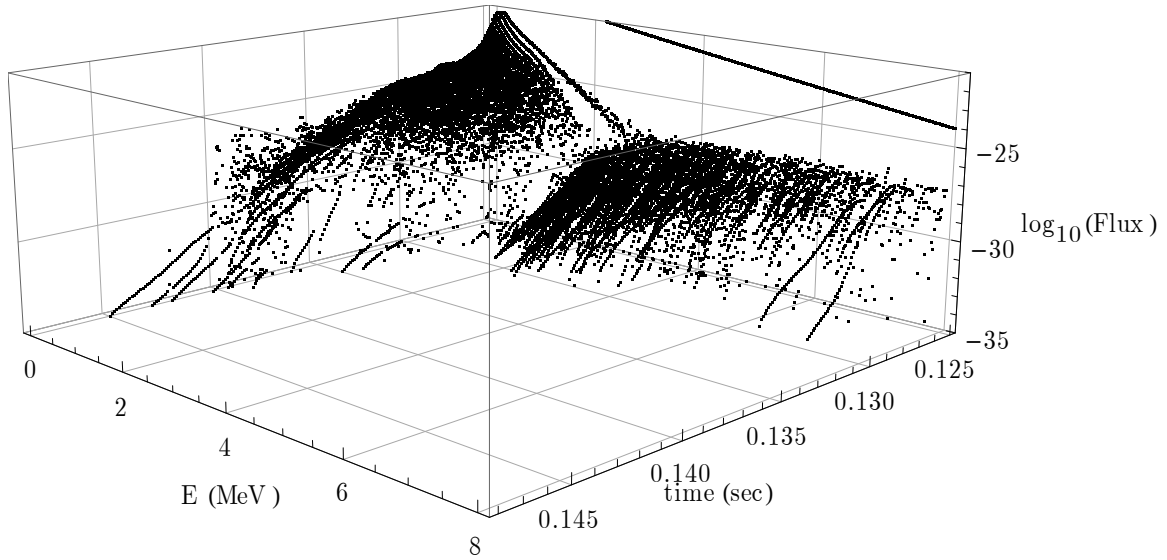


**Figure 34. Ray-Estimated Gamma Ray Flux Per Source Gamma Ray at the Flux-Point from a  $^{235}\text{U}$  Fission Point Source in Time and Energy.**

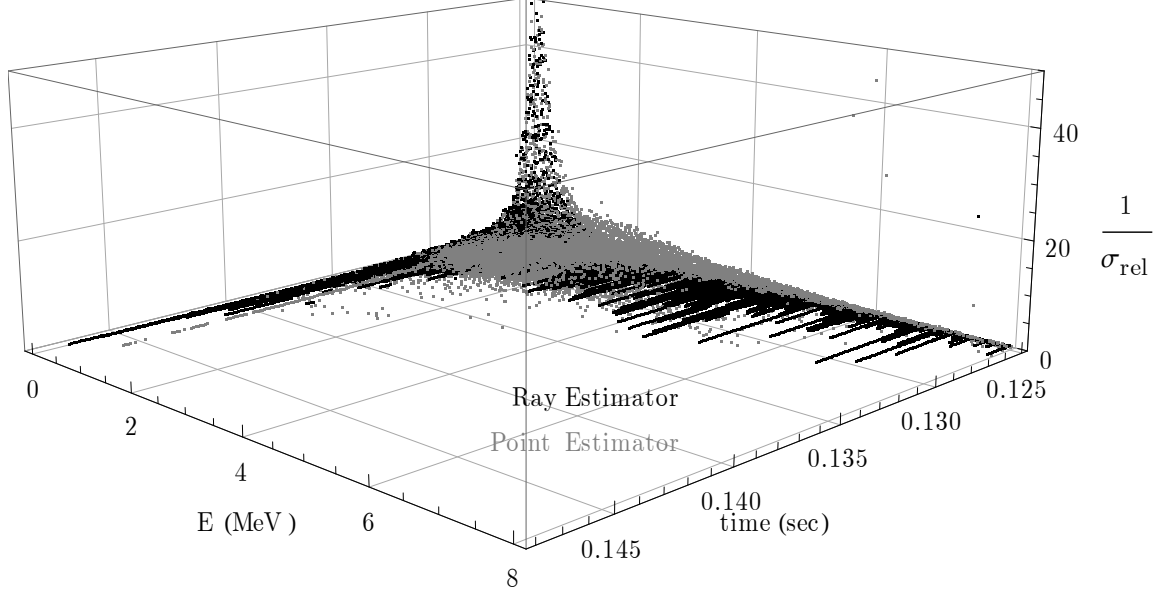


**Figure 35. Inverse Relative Standard Deviation of Point- and Ray- Estimated Gamma Ray Flux at the Flux-Point from a  $^{235}\text{U}$  Fission Point Source in Time and Energy.**

As in the monoenergetic gamma ray source example, we observed the missing  $m_0 c^2$  energy peak from positron annihilation and the same flux *saddle* in the ray estimate. Without comparison to an estimate computed by an independent tool, it was not possible to determine whether the point estimator was functioning correctly for gamma ray transport, but the results of the point estimate were consistent with expectations based on the physics of the transport problem. If we assumed the point estimator was working properly, then these issues with the ray estimate indicate that there may have been a computational problem with the behavior of photon interaction mechanics as the ray next-event estimator integrand was evaluated by numerical quadrature.



## RNEE v5.1 Demonstration: Coupled Neutron-Photon Transport

### Run #5 - Coupled Transport, Fission Neutron Source

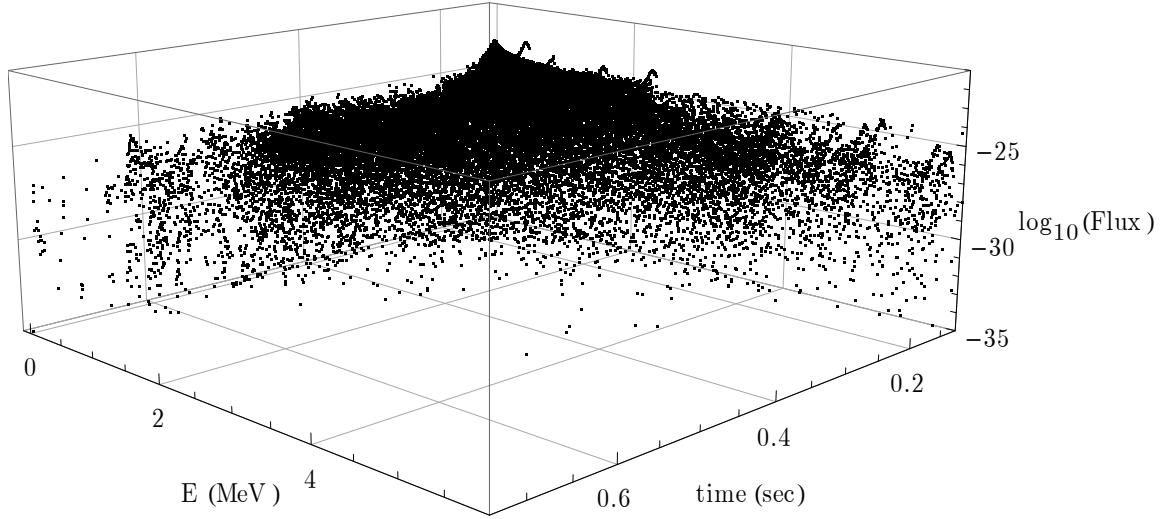
The first coupled neutron-photon test problem was the transport of secondary gamma rays induced by prompt neutrons from a Watt distributed  $^{235}\text{U}$  fission neutron point source. The purpose of this simulation was to demonstrate the application of RNEE v5.1 to coupled neutron-photon transport computations. Properties of the neutron source and flux-point time-energy grid are listed in Table 10.

Table 10. Properties of the Source and Flux-Point Time-Energy Grid for Fission Neutron Source Coupled Neutron-Photon Transport Demonstration.

<u>Source</u>		<u>Gamma Flux-Point Time-Energy Grid</u>	
<b>Type</b>	Neutron, $^{235}\text{U}$ Fission	<b>Energy Range</b>	0.01 – 8 MeV
	Watt Distribution	<b>Energy Resolution</b>	0.01 MeV
<b># of Histories</b>	$1 \times 10^6$ in 10 batches	<b>Time of Interest</b>	1 sec
<b>Altitude</b>	50 km	<b>Time Resolution</b>	0.0001 sec
		<b>Flux-Point Altitude</b>	35,810 km

The free-field secondary gamma ray flux at the flux-point per source neutron  $\left( \gamma_{\text{flux-point}} \cdot \text{cm} \cdot \text{cm}^{-3} \cdot \text{s}^{-1} \cdot \text{n}_{\text{source}}^{-1} \right)$  for each time-energy bin is plotted for the point estimator and the ray estimator in Figure 36 and Figure 37 respectively. The inverse relative standard deviation,  $1 / \sigma_{\text{rel}}$ , for each time-energy bin is plotted in Figure 38 to compare the relative certainty of the

flux estimate from the point and ray estimators (larger values indicate higher certainty).



**Figure 36. Point-Estimated Secondary Gamma Ray Flux Per Source Neutron at the Flux-Point from a  $^{235}\text{U}$  Fission Neutron Point Source in Time and Energy.**

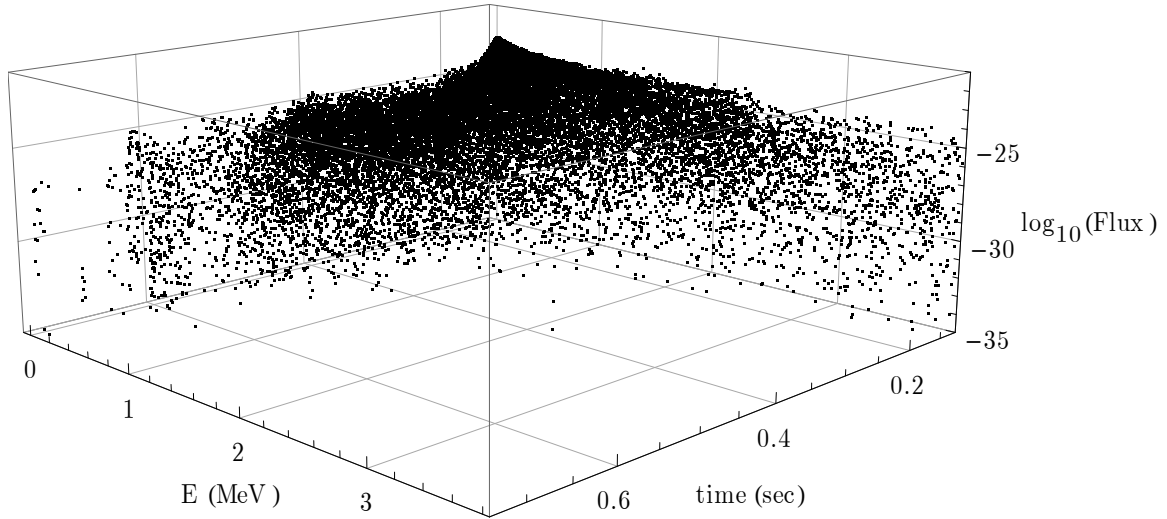


**Figure 37. Ray-Estimated Secondary Gamma Ray Flux Per Source Neutron at the Flux-Point from a  $^{235}\text{U}$  Fission Neutron Point Source in Time and Energy.**

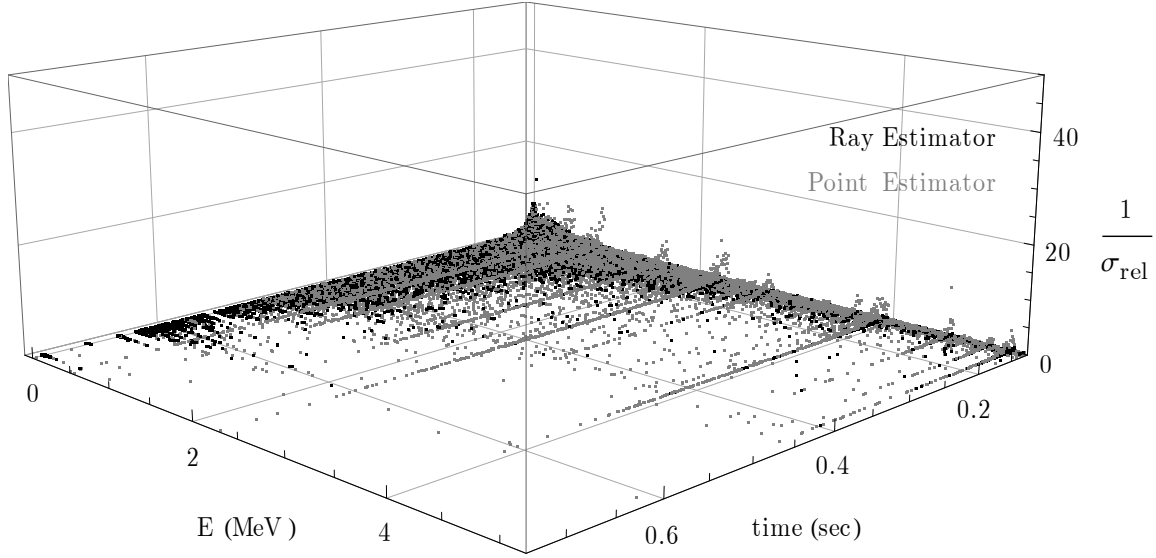


**Figure 38. Inverse Relative Standard Deviation of Point- and Ray- Estimated Secondary Gamma Ray Flux at the Flux-Point from a  $^{235}\text{U}$  Fission Neutron Point Source in Time and Energy.**

It was immediately apparent that both the point and ray estimates had not converged on a solution for larger values of time and energy. Because of the low mean energy of neutrons from the Watt distribution, the  $1 \times 10^6$  neutron histories induced a total of only  $0.24 \times 10^6$  secondary gamma rays for transport computations. The low number of secondary gamma rays indicated that the code implementation for secondary gamma ray production was inefficient. Longer computational times, for corresponding larger numbers of prompt neutron histories, were required for this transport problem.

### **Run #6 - Coupled Transport, Monoenergetic Neutron Source**

The next coupled neutron-photon test problem was the transport of secondary gamma rays induced by prompt neutrons from a monoenergetic

neutron point source. The purpose of this simulation was to supplement the demonstration of run #5 with a coupled neutron-photon computation with a higher number of induced secondary gamma rays. Properties of the neutron source and flux-point time-energy grid are listed in Table 11.

**Table 11. Properties of the Source and Flux-Point Time-Energy Grid for Monenergetic Neutron Source Coupled Neutron-Photon Transport Demonstration.**

<u>Source</u>		<u>Gamma Flux-Point Time-Energy Grid</u>	
<b>Type</b>	Neutron, Monoenergetic	<b>Energy Range</b>	0.01 – 15 MeV
<b>Energy</b>	14.06 MeV	<b>Energy Resolution</b>	0.01 MeV
<b># of Histories</b>	$1 \times 10^6$ in 10 batches	<b>Time of Interest</b>	1 sec
<b>Altitude</b>	50 km	<b>Time Resolution</b>	0.0001 sec
		<b>Flux-Point Altitude</b>	35,810 km

The free-field secondary gamma ray flux at the flux-point per source neutron  $\left( \gamma_{\text{flux-point}} \cdot \text{cm} \cdot \text{cm}^{-3} \cdot \text{s}^{-1} \cdot \text{n}_{\text{source}}^{-1} \right)$  for each time-energy bin is plotted for the point estimator and the ray estimator in Figure 39 and Figure 40 respectively. The inverse relative standard deviation,  $1 / \sigma_{\text{rel}}$ , for each time-energy bin is plotted in Figure 41 to compare the relative certainty of the flux estimate from the point and ray estimators (larger values indicate higher certainty).

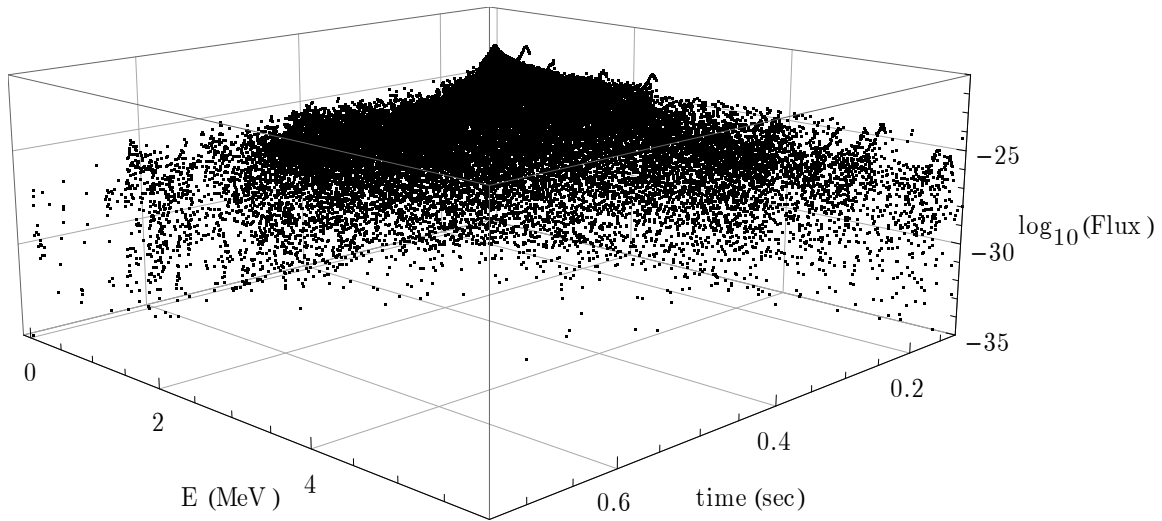


**Figure 39. Point-Estimated Secondary Gamma Ray Flux Per Source Neutron at the Flux-Point from a Monoenergetic Neutron Point Source in Time and Energy.**

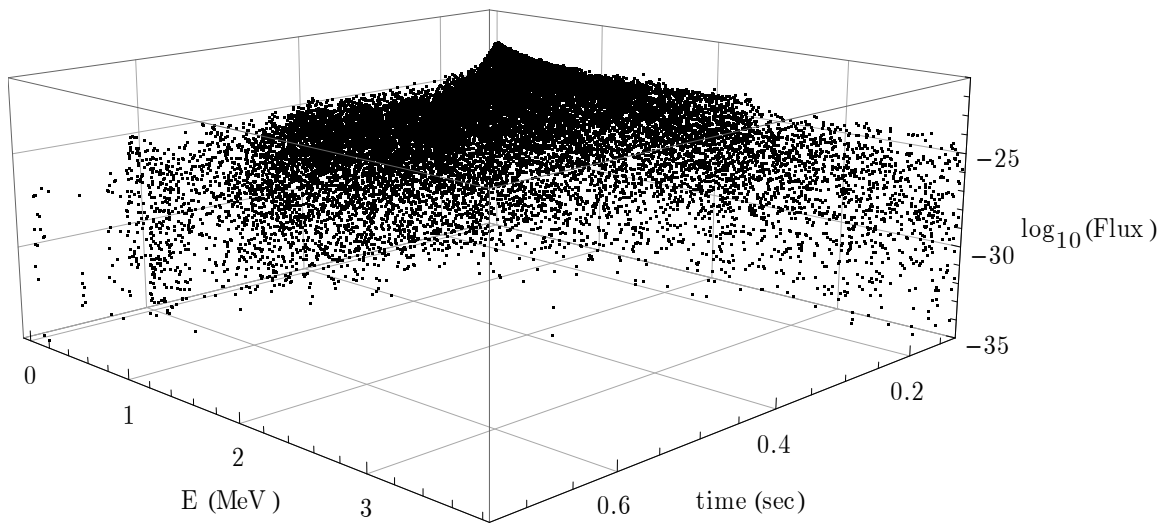


**Figure 40. Ray-Estimated Secondary Gamma Ray Flux Per Source Neutron at the Flux-Point from a Monoenergetic Neutron Point Source in Time and Energy.**

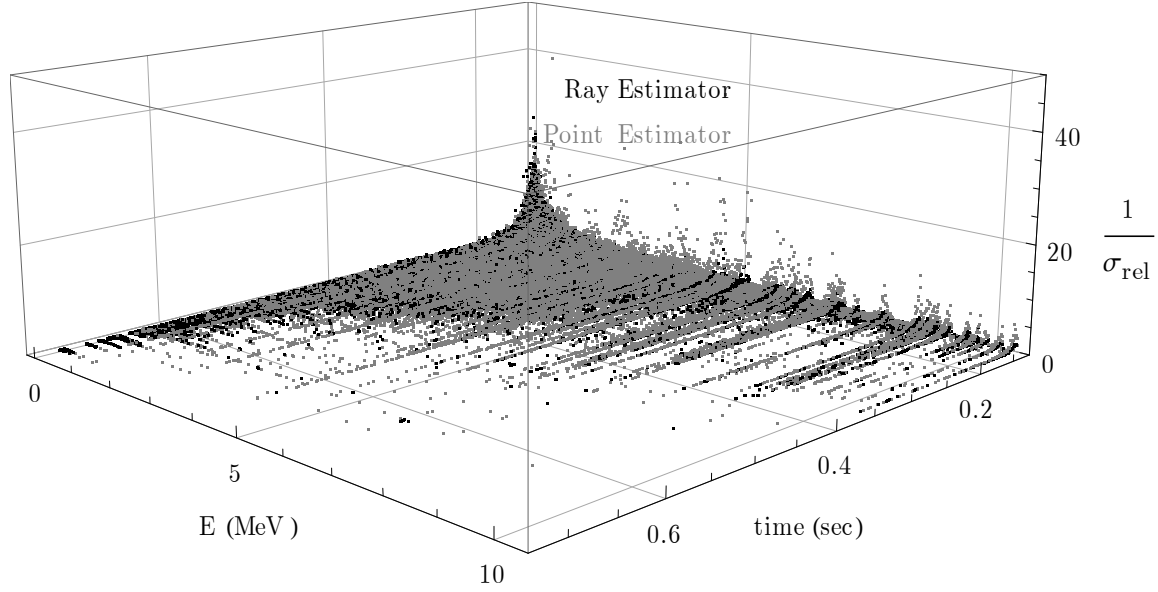


**Figure 41. Inverse Relative Standard Deviation of Point- and Ray- Estimated Secondary Gamma Ray Flux at the Flux-Point from a Monoenergetic Neutron Point Source in Time and Energy.**

For this simulation, the  $1 \times 10^6$  neutron histories produced  $5.9 \times 10^6$  secondary gamma rays for transport computations. The larger number of gamma rays produced a flux estimate with much higher certainty than the estimate from run #5. However, the variance in the secondary gamma ray flux estimate was still higher than the primary gamma ray estimates discussed in runs 3 and 4. Some of the increase in variance can be attributed to the lower number of batches used to compute batch statistics. The greater variance in the secondary gamma estimates is also a product of the fact that as each secondary particle is born during the simulation, it inherits the weight of its parent at the time of its birth. Since the parent has already spent some simulation time transporting through the scattering medium, this birth weight is always less than unity.

Thus, despite the large number of secondary gamma rays produced, each of these gamma rays carries the weight of less than one whole gamma ray.

Despite the higher variance in the estimated flux, many energy peaks in the secondary gamma ray flux estimate were apparent in the point estimate. These peaks correspond to gamma emission lines from the decay of nuclei excited by neutron interactions. As with the  $m_0c^2$  positron annihilation peak in the primary gamma ray transport demonstrations, the gamma emission lines were not visible in the ray-estimated secondary gamma ray flux estimate.

## V. Conclusions

The implementation of gamma ray interaction physics in the Ray Next-Event Estimator (RNEE) v5.1 code was successful with limitations. Neutron transport computations with RNEE v5.1 were consistent with RNEE v4.0 despite significant organizational changes to the source code. Ray Next-Event Estimator v5.1 gamma ray transport computations using the built-in point estimator produced flux estimates with features consistent with expectations based on the physics of the transport problem. Ray Next-Event Estimator v5.1 gamma ray transport computations using the ray estimator were not consistent with expectations. In particular, expected energy peaks from positron annihilation and gamma decay by gamma emission were not observed in the ray estimate. The ray-estimated gamma ray flux at the flux-point due to primary gamma rays, runs 3 and 4, also included the low-flux *saddle* not observed in the point estimate. Coupled neutron-photon transport computations were also demonstrated, with the observed limitations on gamma ray flux estimates by the ray estimator, and a need for reduced computation time to adequately sample the domain for secondary gamma ray transport computations was identified.

Continued development of this estimation method is important because little real-world data exists with which to validate the results of existing or new estimators for this class of problems. As a limited-utility substitute for validation



against real-world data, estimates computed using different methods and/or tools can be compared with one another for investigation of the utility and physical relevance of each estimate. With further refinement of the physical models for neutron and photon transport, the RNEE code will become a formidable tool to be used in conjunction with others for computational transport of neutral particles for this interesting class of problems.

## Appendix A. RNEE 5.1 Release Notes

These release notes accompany version 5.1.05 of the Ray Next-Event Estimator (RNEE) Fortran computer code. Included is a brief description of the program and source code, known issues, and recommended areas for improvement. This document in no way constitutes a user manual or guide to the use, application, and/or modification of the RNEE.

### Ray Next-Event Estimator v5.1.05

**Date:** 06 February 2011

**Authors:** M. Zickafoose, W. Dailey

**Advisor:** K. Mathews

**Platform of Build:** Microsoft Visual Studio 2008 w/  
Intel Fortran Compiler 12.0.2.154  
32- and 64- bit architectures

The source code is comprised of 31 modules containing subroutines, functions, and the main program that make up the estimator code. The ray-next-event estimator has been developed to find the flux at a specified location in the flux field, which we have called the *flux-point*. In the code implementation, this term is awkward as a variable name. Therefore, the term *detector* is used in the code and file formats, and consequently in these appendices.

### RNEE\_Driver

- main program module
- contains version details and history
- no known issues
- no recommendations

### Monte\_Carlo\_Module

- contains top-level routines to handle running of simulation batches and managing computational data flow
- no known issues
- Recommendation: If batch or particle level parallelism is implemented, most of the main parallel statements will be in this module.

### **Monte\_Carlo\_Neutron**

- contains top-level routines for neutron transport computations
- module variables include neutron interaction cross sections
- no known issues
- Recommendation: Should additional neutron interaction types be added, it may be necessary to revisit the manner in which neutron cross sections are stored. The current unified energy grid is a simple, logical solution; but it is memory intensive and significant computational time is spent searching the cross sections tables.

### **Monte\_Carlo\_Gamma**

- contains top-level routines for gamma transport computations
- module variables include photo-atomic cross sections
- Known Issue: The subroutine Load\_Cross\_Sections loads the photo-atomic cross sections into a unified energy grid using logarithmic interpolation between points. Discontinuities such as the "k-edge" are not explicitly handled: The loading routine does not look for special cases.
- Recommendation: Should additional photon interactions be added, particularly photo-nuclear interactions, the loading and storage of cross sections variables will need to be reworked.

### **Processing\_Module**

- contains the bulk of the ray next-event estimator computational code
- computes point estimates, ray properties and geometry, partitions rays, and computes ray estimates
- Parallel estimation is implemented in the subroutine Partition\_and\_Estimate
- no known issues
- Recommendation: Review the implementation of Parallel Estimation. Current implementation actually degrades performance (longer computation time) if enabled for simulations with low resolution detector grids.

### **Sampling\_Module**

- Contains most of the routines and functions that utilize random numbers from the random number generator stream
- Selection of particle energies, directions, and interaction material/mechanism and other statistical quantities are handled here

- no known issues
- no recommendations

### **Results\_Module**

- Contains subroutines to condense, compute, and write output data to file
- no known issues
- no recommendations

### **Transport\_Functions\_Shared**

- Contains subroutines and functions shared by neutron and gamma transport computations
- Includes routines with code specific to a particular particle type, but each routine is used to transport both particle types
- no known issues
- no recommendations

### **Transport\_Functions\_Common**

- Contains subroutines and functions common to neutron and gamma transport computations
- No particle type specific code
- no known issues
- no recommendations

### **Transport\_Functions\_Neutron**

- Contains subroutines and functions specific to neutron transport
- no known issues
- no recommendations

### **Transport\_Functions\_Gamma**

- Contains subroutines and functions specific to gamma ray transport
- no known issues
- no recommendations

### **Root\_Solver\_Module**

- Contains functions and subroutines for root-solving
- no know issues
- no recommendations

### **Tallies\_Module**

- Contains routines to initialize, increment, and output tallies for each detector bin
- Module variables include tally grids for the point estimator and the ray estimator
- no known issues
- no recommendations

### **Setups**

- Contains setup and initialization routines for the estimator
- Reads in data from the three main input files: ControlRNEE, Problem\_Definition, and Method\_Definition
- no known issues
- no recommendations

### **Statistics\_Module**

- Performs statistical comparison between batches and writes results to file
- no known issues
- no recommendations

### **Geometry\_Functions**

- Contains low-level functions and routines for computing geometric quantities for Cartesian and spherical geometries
- no known issues
- no recommendations

### **TE\_Spectra**

- Contains routines to initialize, increment, maintain the detector contribution time-energy spectra grids
- Module variables include batch-time-energy spectra for each detector
- no known issues
- Recommendation: Implement storage and maintenance of time-energy spectra as sparse matrices. This will reduce the memory requirements for the program and improve performance. Also look into the need to maintain batch results in memory. Each batch could be written to file and then read back in for statistics and post-processing.

### **Daughter\_Particles\_Module**

- Contains subroutines to sample and compute secondary particles and then store that particle data for later transport computations

- Known Issue: The current implementation of excited state gammas uses a recursive subroutine when `Level_Gamma_Decay_Sampled` is set to `False`. If an atmospheric constituent is added with *many* excited energy levels, this recursion could go too deep and cause excessive memory use or program performance degradation. No issues were observed with nitrogen or oxygen.
- no recommendations

### **Table\_Search\_Module**

- Contains subroutines and functions to perform searches of detector grids and cross sections variables
- no known issues
- Recommendation: Although an efficient binary search routine forms the backbone of table searching for the estimator, the majority of computational time is spent searching for detector time-energy bins. Any performance enhancements (maybe parallel searching?) to the search routines decrease estimator computational time.

### **Distribution\_Functions**

- Contains functions to compute and/or sample from various energy distributions for initial particle energies
- no known issues
- Recommendation: Renaming of distribution functions to distinguish between general distributions, neutron specific distributions, and gamma specific distributions. Also refine the input strings in `Problem_Definition.txt` where the source distribution is specified.

### **Error\_Log\_Module**

- Contains routines to write error conditions to file
- no known issues
- no recommendations

### **Quadratures\_Module**

- Contains numerical quadrature routines, general purpose and customized for RNEE functions
- no known issues
- no recommendations

### **Particle\_Stacks**

- Contains routines to initialize, update, and track memory for storage of particle awaiting transport
- Module variables include particle heaps for photons and neutrons
- no known issues
- no recommendations

### **Interpolation\_Module**

- Contains functions to linearly and logarithmically interpolate between data points
- no known issues
- no recommendations

### **Physical\_Constants**

- Contains parameters for physical constant values and program run constants
- no known issues
- no recommendations

### **Prob\_and\_Meth\_Vars**

- Contains variables associated with the problem definition including sources, detectors, and geometry
- Contains variables associated with the method definition including estimator properties, estimator options, and particle/batch specifications
- no known issues
- no recommendations

### **Types**

- Contains most of the user derived types used in the program
- no known issues
- Recommendation: A critical review of the content of each type to eliminate duplicated and unnecessary data structures. This could help to decrease memory requirements and improve estimator performance.

### **Random\_Numbers**

- Contains routines and functions to initialize, maintain, and draw from the random number stream
- no known issues

- Recommendations: If parallel particles or batches are implemented, these routine will need to be modified to provide independent random number streams to each of the computing threads.

**Kinds**

- Contains parameters for variable types
- no known issues
- no recommendations



## Appendix B. Sample Input Files

*(This page intentionally left blank.)*

## RNEE 4.0 Control File: "Control\_RNEE.txt"

&RandomNumberSeed

Seed\_Input = T ! Can be True or False...Only set to True if desire correlated  
!sampling between RayNEE and PtNEE, or for consistency testing

Seed = 13 ! Use a prime number here, if the above value is T

/

&Inputfiles

num\_of\_materials = 2 ! number of atmospheric constituents to include  
num\_of\_cs\_files = 2 ! includes total, elastic and level-inelastic scatters

num\_of\_cs\_files\_per\_material = 19,9,0 ! number of files for each constituent; here only one  
!constituent but 19 cross section files

num\_of\_geometries = 2 ! loads both Flat Geometry and Spherical Geometry Atmosphere

/

&MaterialsList

list\_of\_materials = 'N-14','O-16','\_'

A\_value\_of\_materials = 14.D0,16.D0,0.D0 ! must be same size array as the list\_of\_materials  
!and num\_of\_materials, and in same order

material\_fraction = 0.788488D0,0.211512D0,0.D0 ! must be same size and be normalized so the sum=1

/

&Inputfiles

! Filename for the number density integrals -- Flat Geometry

!filename = 'SlantIntNDbylayerFlat.txt'

filename = 'SlantINDbyHeightFlat.txt'

/

&Inputfiles

! Filename for the number density integrals -- Spherical Geometry

!filename = 'SlantIntNDbylayerSphr.txt'

filename = 'SlantINDbyHeightSphr.txt'

/

&InputFiles

! Filename for the material and mechanism

filename = './CrossSections\pendN14.txt'

/

&InputFiles

! Filename for the material and mechanism

filename = './CrossSections\pendO16.txt'

/

**RNEE 4.0 Problem Definition File: "Problem\_Definition.txt"**

&UnitsInfo

one\_per\_cm2 = T                   ! .TRUE. puts the output in units of [1/cm2], .FALSE. leaves it in units of  
                                  ![1/km2]

counts = F                   ! .TRUE. puts output in counts, .FALSE. puts it in units of Intensity

/

&SourceInfo

```

z = 50.D0          ! [km] - geometric
x = 0.D0           ! [km] - geometric
y = 0.D0           ! [km] - geometric
source_distribution = 'Watt'      ! can be 'Uniform', 'Watt', 'Maxwell', 'Point', 'Fusion', 'Group',
                                   ! 'Boosted'
energy = 14.06D      ! only used if source_distribution = 'Point'
endpoints = 11.7D0,11.71D0      ! only used if source_distribution = 'Group'
sampled_direct_contribution = F  ! Used to determine if the direct flight contribution is sampled
/

```

```

! The following Detector namelist is for a spherical geometry
! therefore it doesn't contain cartesian coordinates,
! but rather the height or look_angles...

```

```

&DetectorInfo

```

```

z = 35810.D0        ! [km]
look_angle = 44.8D0 ! [degrees]
E_min = 0.02D0       ! [MeV]
E_max = 15.D0        ! [MeV]
T_max = 20.D0        ! [s]
E_spacing = 'Linear' ! Can be 'Log' or 'Linear'
E_res = 0.01D0       ! [MeV] only used in E_spacing is 'Linear'
E_divisions = 100    ! Integer number of divisions per decade starting with the E_min decade and
                      ! ending at the E_max decade
E_decades = 4        ! Integer number of decades associated with the E_min and E_max values
T_res = 0.01D0       ! [s]
/

```

```

! The following Detector namelist is for a flat geometry
! therefore it doesn't contain look_angles and the height is set negative
! but rather the cartesian coordinates...

```

```

&DetectorInfo

```

```

z = -1.D0           ! [km] -- but negative implies Flat geometry
x_pos = 0.D0         ! [km]
y_pos = -35810.D0    ! [km]
z_pos = 35810.D0     ! [km]
E_min = 0.02D0       ! [MeV]
E_max = 15.D0        ! [MeV]
T_max = 20.D0        ! [s]
E_res = 0.01D0       ! [MeV]
T_res = 0.01D0       ! [s]
/

```

**RNEE 4.0 Method Definition File:** "Method\_Definition.txt"

```

&MethodDetails

```

```

Batch_size = 100000
num_of_batches = 10
interim_output = 1000001
diagnostics_basic = F
diagnostics_full = F
estimator_choice = 'Both'      ! can be 'PtNEE', 'RayNEE', or 'Both'
diagnostics_screen = T
full_matrix_output = F
Direct_Only = F               ! *Note that the direct contribution is computed every time, but this flag
                               ! is to provide a sampled direct contribution for comparison to the

```

```

                                !computed direct contribution

Integrand_Check = T
/

&VarianceReduction
Leakage_Suppression = T
Absorption_Suppression = T
Mat_mech_sampled = F           ! F -> compute all materials and mechanisms for every ray, T -> sample the
                                !material and mechanism for every ray

/

&DiagnosticsFileNames
Basic_Ray_file = '.\LogFile\Basic_Ray_Log.txt'
Basic_Point_file = '.\LogFile\Basic_Point_Log.txt'
Full_File = '.\LogFile\Full_Log.txt'
/

RNEE 5.1 Control File: "Control_RNEE.txt"
&RandomNumberSeed
Use_MKL_RNGs = T
Seed_Input = T                ! Can be True or False...Only set to True if desire correlated
                                !sampling between RayNEE and PtNEE, or for consistency testing

Seed = 13                      ! Use a prime number here, if the above value is T
/

&Inputfiles
num_of_materials = 2           ! number of atmospheric constituents to include
num_of_neutron_cs_files = 2    ! includes total, elastic and level-inelastic scatters
num_of_gamma_cs_files = 2      ! includes total, elastic and level-inelastic scatters
num_of_cs_files_per_material = 19,9,0 ! number of files for each constituent; here only one

```

```

                                !constituent but 19 cross section files
num_of_geometries = 2          ! loads both Flat Geometry and Spherical Geometry Atmosphere
                                !file names
/

&MaterialsList
list_of_materials = 'N-14','O-16','_'
A_value_of_materials = 14.D0,16.D0,0.D0          ! must be same size array as the list_of_materials
                                                !and num_of_materials, and in same order
material_fraction = 0.788488D0,0.211512D0,0.D0    ! must be same size and be normalized so the sum=1
/

&AtmosphereFiles
! Filename for the number density integrals -- Flat Geometry
filename = '.\AtmosphereFiles\SlantINDbyHeightFlat.txt'
/

&AtmosphereFiles
! Filename for the number density integrals -- Spherical Geometry
filename = '.\AtmosphereFiles\SlantINDbyHeightSphr.txt'
/

&NeutronCSFiles
! Filename for the material and mechanism
filename = '.\CrossSectionFiles\Neutron\pendN14.txt'
/

&NeutronCSFiles
! Filename for the material and mechanism
filename = '.\CrossSectionFiles\Neutron\pendO16.txt'
/

&GammaCSFiles
! Filename for the material and mechanism
filename = '.\CrossSectionFiles\Gamma\N-atomic.txt'
/

```

```
&GammaCSFiles
! Filename for the material and mechanism
filename = './CrossSectionFiles\Gamma\O-atomic.txt'
/
```

```
&LevelFiles
! Filename for the material and mechanism
filename = './LevelsFiles\levelsN14.txt'
/
```

```
&LevelFiles
! Filename for the material and mechanism
filename = './LevelsFiles\levelsO16.txt'
/
```

```
&LevelFiles
! Filename for the material and mechanism
filename = './LevelsFiles\levelsN15.txt'
/
```

```
&LevelFiles
! Filename for the material and mechanism
filename = './LevelsFiles\levelsO17.txt'
/
```

```
&LevelFiles
! Filename for the material and mechanism
filename = './LevelsFiles\n_abs_Q.txt'
/
```

### **RNEE 5.1 Problem Definition File: "Problem\_Definition.txt"**

```
&UnitsInfo
one_per_cm2 = T           ! .TRUE. puts the output in units of [1/cm2], .FALSE. leaves it in units of
                          ! [1/km2]
counts = F               ! .TRUE. puts output in counts, .FALSE. puts it in units of Intensity
/
```



```

&NeutronSourceInfo
z = 50.D0          ! [km] - geometric
x = 0.D0          ! [km] - geometric
y = 0.D0          ! [km] - geometric
source_distribution = 'Point'      ! can be 'Uniform', 'Watt', 'Maxwell', 'Point', 'Fusion', 'Group',
                                   ! 'Boosted'
energy = 14.06D    ! only used if source_distribution = 'Point'
endpoints = 11.7D0,11.71D0        ! only used if source_distribution = 'Group'
/

&GammaSourceInfo
!If x,y,z are not included here, they will be the same as the previously listed source
z = 50.D0          ! [km] - geometric
x = 0.D0          ! [km] - geometric
y = 0.D0          ! [km] - geometric
source_distribution = 'Point'      ! can be 'Uniform', 'Watt', 'Maxwell', 'Point', 'Fusion', 'Group',
                                   ! 'Boosted', 'Fission235'
energy = 10.0D0    ! only used if source_distribution = 'Point'
endpoints = 10.0D0,0.001D0        ! only used if source_distribution = 'Group'
/

! The following Detector namelist is for a spherical geometry
! therefore it doesn't contain cartesian coordinates,
! but rather the height or look_angles...
&NeutronDetectorInfo
z = 35810.D0       ! [km]
look_angle = 44.8D0 ! [degrees]
E_min = 0.015D0    ! [MeV]
E_max = 15.D0      ! [MeV]
T_max = 20.D0      ! [s]
E_spacing = 'Linear' ! Can be 'Log' or 'Linear'
E_res = 0.01D0     ! [MeV] only used in E_spacing is 'Linear'
E_divisions = 100  ! Integer number of divisions per decade starting with the E_min decade and
                   ! ending at the E_max decade
E_decades = 4      ! Integer number of decades associated with the E_min and E_max values
T_res = 0.01D0     ! [s]
/

```

```
! The following Detector namelist is for a flat geometry
! therefore it doesn't contain look_angles and the height is set negative
! but rather the cartesian coordinates...
```

```
&NeutronDetectorInfo
```

```
z = -1.D0           ! [km] -- but negative implies Flat geometry
x_pos = 0.D0         ! [km]
y_pos = -35810.D0    ! [km]
z_pos = 35810.D0     ! [km]
E_min = 0.02D0       ! [MeV]
E_max = 20.D0        ! [MeV]
T_max = 20.D0        ! [s]
E_res = 0.01D0       ! [MeV]
T_res = 0.01D0       ! [s]
```

```
/
```

```
! The following Detector namelist is for a spherical geometry
! therefore it doesn't contain cartesian coordinates,
! but rather the height or look_angles...
```

```
&GammaDetectorInfo
```

```
z = 35810.D0        ! [km]
look_angle = 44.8D0 ! [degrees]
E_min = 0.015D0      ! [MeV]
E_max = 15.D0        ! [MeV]
T_max = 1.0D0        ! [s]
E_spacing = 'Linear' ! Can be 'Log' or 'Linear'
E_res = 0.01D0       ! [MeV] only used in E_spacing is 'Linear'
E_divisions = 100    ! Integer number of divisions per decade starting with the E_min decade and
                     ! ending at the E_max decade
E_decades = 4        ! Integer number of decades associated with the E_min and E_max values
T_res = 0.0001D0     ! [s]
```

```
/
```

```
! The following Detector namelist is for a flat geometry
! therefore it doesn't contain look_angles and the height is set negative
! but rather the cartesian coordinates...
```

```
&GammaDetectorInfo
```

```
z = -1.D0           ! [km] -- but negative implies Flat geometry
x_pos = 0.D0         ! [km]
```

```

y_pos = -35810.D0      ! [km]
z_pos = 35810.D0       ! [km]
E_min = 0.015D0        ! [MeV]
E_max = 15.D0          ! [MeV]
T_max = 0.5D0          ! [s]
E_res = 0.01D0         ! [MeV]
T_res = 0.0001D0       ! [s]
/

```

### RNEE 5.1 Method Definition File: "Method\_Definition.txt"

```

&MethodDetails
geometry = "Sphr"      !"Sphr" or "Flat" selects the geometry to use for computations
diagnostics_basic = F
diagnostics_full = F
Integrand_Check = T
estimator_choice = 'Both'      ! can be 'PtNEE', 'RayNEE', or 'Both'
sampled_direct_contribution = F      ! Used to determine if the direct flight contribution is sampled
diagnostics_screen = T
full_matrix_output = F
Direct_Only = F           ! *Note that the direct contribution is computed every time, but this flag
                          ! is to provide a sampled direct contribution for comparison to the
                          ! computed direct contribution
secondary_particles = T    ! F -> suppresses the production of secondary particles in all reactions
                          ! (pair production still produces 2 photons)
Abs_Induced_Particles = T  ! must have secondary particles set to true for this to be used
Level_Gamma_Decay_Sampled = F ! F -> start appropriately weighted photons for all level gamma decay
                          ! possible chains
parallel_estimation = T
/

&VarianceReduction
Leakage_Suppression = T
Absorption_Suppression = T
Mat_mech_sampled = F      ! F -> compute all materials and mechanisms for every ray, T -> sample the
                          ! material and mechanism for every ray
/

```

```
&NeutronBatches  
Batch_size = 100000  
num_of_batches = 10  
interim_output = 100001  
/
```

```
&GammaBatches  
Batch_size = 100000  
num_of_batches = 10  
interim_output = 100001  
/
```

```
&DiagnosticsFileNames  
Basic_Ray_Diag_file_name = '.\LogFile\Basic_Ray_Log.txt'  
Basic_Pt_Diag_file_name = '.\LogFile\Basic_Point_Log.txt'  
Full_Diag_file_name = '.\LogFile\Full_Log.txt'  
/
```

## Bibliography

- Chapman, S. J. (2008). *Fortran 95/2003 for Scientists and Engineers* (3rd ed.). New York: McGraw-Hill.
- Choppin, G. R., Liljenzin, J.-O., & Rydberg, J. (2002). *Radiochemistry and Nuclear Chemistry* (3rd ed.). Woburn, MA: Butterworth-Heinemann.
- Hubbell, J. H., Gimm, H. A., & Øverbø, I. (1980). Pair, triplet and total atomic cross sections (and mass attenuation coefficients) for 1 MeV to 100 GeV photons in elements  $z = 1$  to 100. *Journal of Physical and Chemical Reference Data*, 9 (4), 1023-1148.
- Knief, R. A. (2008). *Nuclear Engineering: Theory and Technology of Commercial Nuclear Power* (2nd ed.). La Grange Park, IL: American Nuclear Society.
- Knoll, G. F. (2000). *Radiation Detection and Measurement* (3rd ed.). Hoboken, NJ: John Wiley & Sons, Inc.
- Krane, K. S. (1988). *Introductory Nuclear Physics*. Hoboken, NJ: John Wiley & Sons, Inc.
- Lewis, E. E., & Miller, J. W. (1993). *Computational Methods of Neutron Transport*. La Grange Park, IL: American Nuclear Society, Inc.
- Lux, I., & Koblinger, L. (1991). *Monte Carlo Particle Transport Methods: Neutron and Photon Calculations*. Boca Raton, FL: CRC Press, Inc.
- NIST. (2010). *ESTAR: Stopping Power and Range Tables for Electrons*. Retrieved December 3, 2010, from National Institute of Standards & Technology: <http://physics.nist.gov/PhysRefData/Star/Text/ESTAR.html>
- NIST. (2010). *XCOM: Photon Cross Sections Database*. Retrieved November 17, 2010, from National Institute of Standards & Technology: <http://www.nist.gov/pml/data/xcom/index.cfm>
- NIST. (2010). *X-Ray Mass Attenuation Coefficients - Air, Dry*. Retrieved December 3, 2010, from National Institute of Standards & Technology: <http://www.nist.gov/PhysRefData/XrayMassCoef/ComTab/air.html>

- NNDC. (2010). *Nudat 2.5: Chart of Nuclides*. Retrieved November 17, 2010, from National Nuclear Data Center, Brookhaven National Laboratory:  
<http://www.nndc.bnl.gov/nudat2/>
- Persliden, J. (1983). A Monte Carlo program for photon transport using analogue sampling of scattering angle in coherent and incoherent scattering processes. *Computer Programs in Biomedicine* , 17 (1-2), 115-128.
- Verbeke, J. M., Hagmann, C., & Wright, D. (2010). *Simulation of Neutron and Gamma Ray Emission from Fission and Photofission*. Lawrence Livermore National Laboratory.
- Zickafoose, M. S., & Mathews, K. A. (2010-2011). Personal Communications: A New Estimator for Monte Carlo Neutron Transport Through a Layered Medium. Wright-Patterson AFB, OH.

REPORT DOCUMENTATION PAGE					Form Approved OMB No. 0704-0188	
<p>The public reporting burden for this collection of information is estimated to average 1 hour per response, including the time for reviewing instructions, searching existing data sources, gathering and maintaining the data needed, and completing and reviewing the collection of information. Send comments regarding this burden estimate or any other aspect of this collection of information, including suggestions for reducing the burden, to Department of Defense, Washington Headquarters Services, Directorate for Information Operations and Reports (0704-0188), 1215 Jefferson Davis Highway, Suite 1204, Arlington, VA 22202-4302. Respondents should be aware that notwithstanding any other provision of law, no person shall be subject to any penalty for failing to comply with a collection of information if it does not display a currently valid OMB control number.</p> <p><b>PLEASE DO NOT RETURN YOUR FORM TO THE ABOVE ADDRESS.</b></p>						
1. REPORT DATE (DD-MM-YYYY) 24-03-2011		2. REPORT TYPE Thesis		3. DATES COVERED (From - To) Aug 2009 - Mar 2011		
4. TITLE AND SUBTITLE Ray Next-Event Estimator Transport of Primary and Secondary Gamma Rays				5a. CONTRACT NUMBER		
				5b. GRANT NUMBER		
				5c. PROGRAM ELEMENT NUMBER		
				5d. PROJECT NUMBER		
6. AUTHOR(S) Dailey, Whitman T., Captain, USAF				5e. TASK NUMBER		
				5f. WORK UNIT NUMBER		
7. PERFORMING ORGANIZATION NAME(S) AND ADDRESS(ES) Air Force Institute of Technology Graduate School of Engineering and Management (AFIT/EN) 2950 Hobson Way WPAFB, OH 45433-7765				8. PERFORMING ORGANIZATION REPORT NUMBER AFIT/GNE/ENP/11-M04		
9. SPONSORING/MONITORING AGENCY NAME(S) AND ADDRESS(ES) (Intentionally left blank.)				10. SPONSOR/MONITOR'S ACRONYM(S)		
				11. SPONSOR/MONITOR'S REPORT NUMBER(S)		
12. DISTRIBUTION/AVAILABILITY STATEMENT APPROVED FOR PUBLIC RELEASE; DISTRIBUTION UNLIMITED						
13. SUPPLEMENTARY NOTES This material is declared a work of the U.S. Government and is not subject to copyright protection in the United States.						
14. ABSTRACT This thesis investigated the application of the ray next event estimation Monte Carlo method to the transport of primary and secondary gamma rays. The problem of interest was estimation of the free field flux at a distant point in a vacuum from a point source in the atmosphere. An existing Fortran code for neutron transport, Ray Next-Event Estimator v4.0, was adapted to perform photon transport computations including coherent scattering, incoherent scattering, photoelectric absorption, and pair production interactions. Production and transport of secondary gamma rays produced in bremsstrahlung, neutron inelastic scatter, and neutron absorption interactions was also implemented. A new version of the code, Ray Next-Event Estimator v5.1, was produced with the added photon transport capability and other changes focused on future development of the estimator code for application to this class of problems. Code version 5.1 was exercised and compared to version 4.0 for neutron transport computations. Code version 5.1 was also demonstrated for application to gamma ray transport computations and coupled neutron-photon transport computations.						
15. SUBJECT TERMS Monte Carlo, radiation transport, photon transport, gamma ray transport						
16. SECURITY CLASSIFICATION OF:			17. LIMITATION OF ABSTRACT	18. NUMBER OF PAGES	19a. NAME OF RESPONSIBLE PERSON	
a. REPORT	b. ABSTRACT	c. THIS PAGE			Kirk A. Mathews, AFIT/ENP	
U	U	U	UU	127	19b. TELEPHONE NUMBER (Include area code) 255-3636 x4508      kirk.mathews@afit.edu	